SOLID ELECTROLYTE FORMATION IN LI-METAL BATTERIES AND LIFSI/TMP ELECTROLYTE

A Dissertation

by

DIEGO GALVEZ ARANDA

Submitted to the Graduate and Professional School of
Texas A&M University
in partial fulfillment of the requirements for the degree of
DOCTOR OF PHILOSOPHY

Chair of Committee,	Jorge M. Seminario
Committee Members,	Perla B. Balbuena
	Jose Silva-Martinez
	Jun Kameoka
Head of Department,	Dr. Aniruddha Datta

August 2022

Major Subject: Electrical Engineering

ABSTRACT

Rechargeable Li-ion batteries (LIB) are the most popular devices for energy storage but still a lot of research needs to be done to improve their cycling and storage capacity. LIB feature energies densities in the range of 100-265 Wh/kg which is very low if compared with gasoline in which the range is in the order of 12,000 Wh/kg. Therefore, Li-metal has been proposed as an anode material because the energy density of the battery could increase up to 2,600 Wh/kg for a Li-Sulfur battery and to 3,458 Wh/kg for a Li-air (O_2) battery. With the addition of Li-metal as an anode material a new set of batteries called lithium metal batteries (LMB) can be developed with the potential to increase the cell-level energy of the LIBs. Therefore, focus is needed on the lithiation process of Li-metal anodes where it is known the mechanical, electrochemical, and electric phenomena such as cracking, SEI formation and ionic-clustering, respectively, that occur during the charge/discharge cycles.

Performing molecular dynamics simulations of an electrolyte comprising trimethyl phosphate (TMP) solvent and a lithium bis(fluorosulfonyl)imide (LiFSI) salt, the effects of salt concentration on solvation and ion-transport are explored. Three LiFSI-TMP electrolyte salt concentrations of 0.7, 1.43 and 3.82 molar are simulated. A statistical analysis was performed to study ion-pairing, clustering, diffusivity, conductivity, and coordination of Li-ions, providing insights into relations between molecular structures and transport properties. Molecular structure of ionic components changes as concentration increases, from a predominant solvent separated ion pair (SSIP) and contact ion pair (CIP) to aggregate (AGG) salt and ionic cluster formation. The formation of ionic clusters

suggests that the diffusion mechanism of Li-ions changes from a hopping/exchange to a vehicular mechanism as concentration increases; this is validated by a decrease of ionic conductivity. Ionicity was also calculated to reveal how the ionic motion changes from an uncorrelated to a correlated one as the salt concentration increases.

Identifying the mechanism of SEI formation at electronic and atomic levels is especially important to understand how the SEI formation affects the overall battery performance such as the decrease of active material, decrease of cell potential, and interfacial stability. Ab initio molecular dynamics simulations were performed for Li+-conducting electrolytes based on trimethyl phosphates (TMP) and lithium bis(fluorosulfonyl)imide (Li^+FSI^-) salt in contact with a Li-metal electrode. We focused on the transient-state behavior at the electrolyte, interfacial electrolyte−Li-metal electrode, and lithium reference electrode−electrolyte−Li-metal electrode to study dynamics and activation energy barriers of the Li^+ ion, electrochemical and thermal stability of the interface electrode−electrolyte, and potential behavior of the Li-metal electrode, respectively.

An interfacial study is performed using ab initio molecular dynamics simulations to elucidate the solid electrolyte interphase (SEI) evolution formed between an electrolyte based on trimethyl phosphates (TMP) and lithium bis(fluorosulfonyl)imide(Li^+FSI^-) salt in contact with a Li-metal electrode. Going beyond the initial SEI composition generated due to the degradation of one counter-ion adding a second and third counter-ions ana analysis of how the initial SEI evolution is performed. The results indicate a different product formation due to the LiFSI salt dissociation as the SEI is formed. The products

formed due to the dissociation of the 1st LiFSI salt when in direct contact with the Li-metal anode are Li_2O, Li_2S, Li_3N and LiF. These four Li-binary products compose the formed SEI. Then, a 2nd LiFSI is located at the electrolyte/SEI/Li-metal. The products formed due to the dissociation of the 2nd LiFSI when in contact with the SEI are Li_2S, Li_2O, LiF, Li_3NSO_2. Finally, a 3rd LiFSI is located at the electrolyte/SEI/Li-metal. The products formed due to the dissociation of the 3rd LiFSI when in contact with the SEI are $Li_2SO_2NSO_2$ and LiF.

Computational techniques such as molecular dynamics (MD) simulations can simulate a large number of atoms, in the order of 10^5 interacting through their forcefields. A nanobattery MD model is an accurate, yet simple model to study electrochemical phenomena occurring in in any rechargeable battery. A regression machine learning algorithm is proposed to overpass paramount timescale limitations of any atomistic MD model. The primary limitation of the nanobattery model is the extremely short charging time compared to the longer charging time in a real battery. Using data from several macro-scale commercial Li-ion batteries, and a nanobattery MD model, we constructed a scaling regression algorithm to scale the values obtained from the nanobattery MD model to a macro-scale Li-ion battery. The goal is to demonstrate that three transport properties: 1) the time, t_{Li}, a Li-ion spend to travel from cathode to anode; 2) the superficial density frequency of arrival Li-ions, ALi ($s^{-1}A^{-2}$); and 3) the frequency, fLi, of Li ions arrival to the anode, can be incorporated in one model that could predict the macro-scale variables having as an input the nano-scale variables.

CONTRIBUTORS AND FUNDING SOURCES

Contributors

This work was supervised by a dissertation committee consisting of Professors Jorge M. Seminario, Jun Kameoka and Jose Silva-Martinez from the Department of Electrical and Computer Engineering and Professor Perla B. Balbuena from the Department of Chemical Engineering

All work for the dissertation was completed by the student, under advisement of Professor Jorge M. Seminario from the Department of Electrical and Computer Engineering.

Funding Sources

This work was made possible in part by the support of the Texas A&M Supercomputer Facility and the Texas Advanced Computing Center.

NOMENCLATURE

TMP	Tetraphosphate
LiFSI	Lithium bis(fluorosulfonyl)imide
HOMO	Highest Occupied Molecular Orbital
LUMO	Lowest Unoccupied Molecular Orbital
CMD	Molecular Dynamics
AIMD	Ab-initio Molecular Dynamics
SEI	Solid Electrolyte Interphase
ML	Machine Learning
DFT	Density Functional Theory
AGG	Aggregate Salt
CIP	Contact Ion Pair
SSIP	Solvent Separated Ion Pair

TABLE OF CONTENTS

Page

LIST OF FIGURES

Page

LIST OF TABLES

Page

1. CHAPTER I INTRODUCTION

Rechargeable lithium-ion batteries (LIB) are the most popular devices for energy storage. Nevertheless, several efforts are being done to improve their cycling and storage capacity. Li-metal has been proposed as an anode material because of its large theoretical capacity of ~4200 mAh/g. Therefore, focus is needed on the lithiation process of Li-metal anodes where it is known the mechanical, electrochemical, and electric phenomena such as cracking, SEI formation and ionic-clustering respectively, that occurs during the charge/discharge cycles.

1.1. Lithium metal batteries

The rechargeable battery is a cycling device. At each cycle, the battery receives electrical energy and converts it into chemical energy, which is stored for a while and then delivers it again as electrical energy when needed. This cycle repeats until one or a few of its components degrade, being unable to continue the cycling at acceptable performances.

---

*Part of this chapter is reprinted with permission from:
Li-Metal Anode in Dilute Electrolyte LiFSI/TMP: Electrochemical Stability Using Ab Initio Molecular Dynamics by Diego E. Galvez-Aranda and J. M. Seminario, 2020. J. Phys. Chem. C, 124, 21919-21934, Copyright 2020 by American Chemical Society. Ion Pairing, Clustering and Transport in a LiFSI-TMP Electrolyte as Functions of Salt Concentration using Molecular Dynamics Simulations by Diego E. Galvez-Aranda and J. M. Seminario, 2021. J. Electrochem. Soc., 168, Copyright 2021 by The Electrochemical Society.

Concerted oxidation of Li and reduction of Li^+ reactions take place at the cathode and anode, respectively, during charge and at the anode and cathode, respectively, during discharge take care of the conversion of electrical to chemical and chemical to electrical during charge and discharge, respectively.

These reactions occur only when the battery is externally connected during the charge to a power source or during the discharge to a load. Since 1920, the rechargeable battery has been used to supply the required energy to operate the entire electrical system of cars. Also, since 1991, the rechargeable battery has been used as the main power source for portable electronic devices such as: mobile-phones, laptops, cameras, and tablets. Since its invention in 1859,[1] the rechargeable battery has continuously improved its capacity, durability, and efficiency. During the mid-1960s, Li-metal was thought as an excellent candidate for anodes due to its high specific energy per weight and to its theoretical specific capacity of 3860 mAh/g in comparison with other materials such as zinc with a theoretical capacity of 820 mAh/g.

1.2. Electrolytes

Current commercial electrolytes used in rechargeable Li+-ion batteries (LIBs) are mainly made of hexafluorophosphate (LiPF6) salt dissolved in carbonate liquids (CLs). Linear carbonates such as ethyl methyl carbonate (EMC), diethyl carbonate (DEC), or dimethyl carbonate (DMC) are used as solvents keeping the electrolyte viscosity low and the electrolyte conductivity high. Unfortunately, these LiPF6/CL electrolytes are highly volatile and flammable,[2], especially in abused conditions such as overcharging and

overheating. Therefore, it is necessary to develop novel electrolytes accomplishing all of the safety issues as well as electrochemical stability with electrodes.

Currently used electrolytes could be replaced by solid-state electrolytes (SSEs), especially when Li-metal electrodes are used.[3]The main issue when Li-metal electrodes are used is the formation of Li dendrites,[4] which simply grow through the liquid electrolyte until contacting the opposite electrode, causing a short circuit.[5-6] Several studies showed that SSE suppresses or reduces the growth of Li dendrites.[7] However, most of the SSEs form a solid-electrolyte interphase (SEI) that consumes the ionic charge carriers (Li^+ ions); thus, they are not electrochemically stable in contact with Li-metal.[8]

Most SSEs have lower conductivities at room temperature than liquid electrolytes do. Ionic liquid (IL) electrolytes are another potential solution to replace the current-commercial electrolytes due to their nonvolatility and nonflammability.[9] ILs based on trimethylpropylammonium ($TMPA^+$) coupled with bis-(trifluoromethylsulfonyl)imide ($[TFSI]^-$) feature an electrochemical window wide enough to allow the electrochemical deposition of Li without any additives.[10] Lithium bis-(fluorosulfonyl)imide (LiFSI) has been studied as a conducting salt and its ionic liquids (ILs) as nonflammable solvents for Li^+-ion batteries.[11]

Pure ionic liquid electrolytes based on the FSI^- anion, without any additives other than a lithium salt, are compatible with Li-metal electrodes.[12-13] Despite all of the work done in the potential use of IL as electrolyte, it is unlikely that an electrolyte can be made of pure IL. In pure IL, the high viscosity and the high ion concentration make the overall electrical conductivity relatively low.[14] Also, pure ILs are economically unfeasible. On

the other hand, dilute ILs have been proposed as a possible electrolyte solution since they can overcome the practical limitations of pure ILs.[15-17]

1.3. Solid Electrolyte Interphase

Battery performance strongly depends on the SEI film, which can profoundly modify several observables such as Coulombic efficiency, rate capability, cycling life, and safety;[18-19] therefore, it is extremely important to study the composition of the SEI film.

Experimental work such as in situ and in operando experiments requires modifications of the operating conditions of the battery to perform multiple measurements in the same device at the same time; therefore, experimental conditions are different from operating conditions of the battery, for this reason, the use of computational tools is necessary to elucidate the structural, dynamical, and reactive behavior of LiFSI/TMP electrolytes in contact with a Li-metal electrode. Therefore, identifying the mechanism of SEI formation at electronic and atomic levels is very important to understand how the SEI formation affects the overall battery performance such as the decrease of active material, decrease of cell potential, and interfacial stability.

1.4. Classical molecular dynamics

All MD simulations of the battery are performed with the LAMMPS[20] program to calculate global properties and predict behavior of the anode and electrolyte solution of a nanobattery. The interactions between particles are described by force fields. A force field defines an interatomic potential given a set of parameters. These parameters are usually found by experimental methods and/or, more recently, by quantum mechanical calculations.

Nonbonded interactions in the solvent between pair of atoms *i* and *j* from counterion, ions and solvent, are defined with a Lennard-Jones (LJ) potential in conjunction with a Coulombic (electrostatic) potential,

$$E_{ij} = 4\varepsilon_{ij}\left(\left(\frac{\sigma_{ij}}{r_{ij}}\right)^{12} - \left(\frac{\sigma_{ij}}{r_{ij}}\right)^{6}\right) + C\frac{q_i q_j}{r_{ij}} \tag{1.1}$$

where r_{ij} is the distance between any intermolecular pair of atoms *i* and *j*, ε and σ are the well-depth and zero-energy length, respectively, of the LJ potential. Mixing rules for the LJ interactions can be used to obtain parameters to define interaction between different atoms types.

Other potentials such as MEAM and Born-Mayer describe in a precise way the interactions of the all atoms involved. There is no need to apply the mixing rules with these potentials because all the parameters were chosen to describe experimental data

2. CHAPTER II ION PAIRING, CLUSTERING AND TRANSPORT IN A LIFSI-TMP ELECTROLYTE

2.1. Synopsis

Battery capacity is highly related to ion-pairing mechanisms in electrolytes, since a cluster formation can lead to dead Li formation, reducing the number of charge carriers and leading to capacity fading. We use molecular dynamics simulations to model an electrolyte comprising trimethyl phosphate (TMP) solvent and a lithium bis(fluorosulfonyl)imide (LiFSI) salt, exploring effects of salt concentration on solvation and ion-transport. We simulate the LiFSI-TMP electrolyte for salt concentrations of 0.7, 1.43 and 3.82 molar. A statistical analysis was performed to study ion-pairing, clustering, diffusivity, conductivity, and coordination of Li-ions, providing insights into relations between molecular structures and transport properties. Molecular structure of ionic components changes as concentration increases, from a predominant solvent separated ion pair (SSIP) and contact ion pair (CIP) to aggregate salt (AGG) and ionic cluster formation. Given the formation of the ionic cluster, the diffusion mechanism followed by Li-ions changes from a hopping/exchange to a vehicular mechanism as concentration increases; this is reflected in a decrease of ionic conductivities.

---

*Reprinted with permission from:
Ion Pairing, Clustering and Transport in a LiFSI-TMP Electrolyte as Functions of Salt Concentration using Molecular Dynamics Simulations by D. E. Galvez-Aranda, J. M. Seminario, 2021. Journal of The Electrochemical Society, 2021, vol. 168, no 4, p. 040511.

Ionicity was also calculated to reveal how the ionic motion changes from an uncorrelated to a correlated one as the salt concentration increases.

2.2. Introduction

Considerable efforts have been made in the last years to develop advance electrode materials for high-energy and high-power density batteries.[21-23] The lithium-ion battery (LIB) is the most popular rechargeable battery due to its higher energy density and cycling life than those from other technologies.[24-26] The applications of LIB go from portable electronic devices to electric vehicles.[27] In a LIB, the electrolyte allows the transport of the charge carriers, Li^+, from cathode to anode and vice versa.

The electrolyte is also an electrical insulator that avoids short-circuiting the electrodes, keeping them electronically isolated. Internal short circuits can occur when ions plating the anode growth as dendrites.[4, 28] Therefore, the electrolyte plays an important role in the LIB overall performance. Safety issues regarding flammability of LIB have been under studies in the last years.[29-30]

The source of explosion hazards lie on the flammable components of the electrolyte,[31] such as carbonate electrolytes, which are the most common ones used in LIB. Typically, the electrolyte of a LIB is a solution of lithium salt such as lithium hexafluorophosphate, $LiPF_6$ in organic carbonates such as ethylene carbonate and dimethyl carbonate. However, these organic carbonate-based electrolytes are flammable, especially in a battery operated under extreme conditions. Overcharging, overheating, and short circuiting are examples of extreme conditions. Even in normal operating conditions,

the electrolyte increases heat dissipation due to exothermic reactions occurring during battery charge and discharge cycles.[32-33] A better choice of electrolyte material could improve the safety of LIBs. Trimethyl phosphate (TMP) is one of the organic phosphorus-based compounds that are being tested as possible diluent for electrolytes because its good flame-retarding properties.[34-35] However, the addition of flame retardant to the electrolyte degrades the electrochemical performance of the battery.[36-38]

Electrolytes for LIBs contain lithium salt dissolved in a mixture of solvent at a determined salt concentration. The most common electrolyte concentration used in all batteries is 1 mol l^{-1} since the maxima of ionic conductivities frequently occurs near 1 mol l^{-1}.[39] Formation of several types of ion-pairings may occur at close-circuit states (charge or discharge) as well as at open circuit state. Based on the compounds present in an electrolyte, cations (C), anions (A) and solvent, three types of ion-pairing can be described: solvent separated ion-pair (SSIP), contact ion-pair (CIP) and ion-aggregate (AGG). AGG may be found as triple ions (C-A-C), ion pair dimers $(C\text{-}A)_2$ or even ionic clusters.[40] As the salt concentration increases, significant ion-pairing and ion-aggregates occurs, leading to the formation of new structures affecting several electrolyte properties such as transport, thermal, mechanical, electrochemical, and interfacial.[39]

Super-concentrated electrolytes can be considered as a transition regime between the conventional "1 M" electrolyte and neat ionic liquids or molten salts. Polymer based electrolytes were the first showing promising results as a super-concentrated electrolyte in terms of the ionic conductivity.[41-42] The use of high concentrated electrolytes can address the thermal and electrochemical stability at the electrode/electrolyte interfaces.[43]

For example, a dilute TMPs electrolyte cannot passivate carbonaceous electrodes, which are the most common electrodes used in commercial batteries.[38, 44]

However, the interfacial stability can be improved using a high concentrated electrolyte. Shi et al., proved that a 5 M LiFSI-TMP electrolyte enhance the cycling life of the battery and also effectively suppress the dendrite growth in Li-metal anodes.[43] Even though most of the previous work were focused in enhancing cycling stability analyzing interfacial stability, ion transport properties are equally important in the overall performance of the battery. The battery capacity is highly related to the ion pairing mechanism in the electrolyte,[45] because cluster formation can lead to dead Li formation, reducing the number of charge carriers.

TMP was tested as a solvent replacement for carbonate solvents in LIBs given its good flame-retarding ability and low cost of organic phosphorus-based compounds.[34-35] Also, LiFSI was tested in solvents such as dimethyl carbonate and ethylene carbonate showing the ability to mitigate dendrite formation exclusively at salt concentrations greater than 4 M, due to the high density of the created SEI layer able to prevent corrosion of the Li-metal electrode, thus, providing an excellent stability; simultaneously, the SEI features high ionic conductivities, 10^{-4} to 10^{-8} S cm^{-1}, leading to very stable voltage profiles during cycling of Li-electrodes.[46]

Experimental[43, 47] and computational[48-50] research have been focused on the stability of LiFSI-TMP electrolytes in contact with Li metal anode; however, transport properties and ionic coupling from the electrolyte are equally important to develop better batteries in terms of cyclability and charge rate. Also, high concentration electrolytes have

gained attention because they present a higher reductive/oxidative stability and ionic density, in comparison withthe regular ~1 M concentration liquid electrolytes.[49, 51] However, high concentrated electrolytes present a low ionic conductivity, usually in the order of 10^{-7} to 10^{-11} mS cm^{-1}.[51-53]

In order to overcome these drawbacks such as the low ionic conductivity, several strategies have been proposed, such as the use of localized high concentrated electrolytes to improve the ionic conductivity by adding a diluent to reduce the overall concentration of the salt in the solution.[49, 52] However, to improve an electrolyte material, the understanding of ionic materials in dilute and high concentrated electrolytes should be advanced. Atomistic theoretical computational tools can help us to overcome the limited capability to characterize ionic interactions in experiments, given the difficulty to decouple individual motion and correlations of cations, anions, and solvent molecules.

2.3. Methodology

Ab initio molecular dynamics (AIMD) simulations are performed with the Quantum Espresso program,[54] using the Born–Oppenheimer approximation with the Perdew–Burke–Ernzerhof (PBE) functional[55-56] and within the projector augmented-wave approach (PAW)[57] to solve the electronic Schrödinger equation. A planewave basis set with an energy cutoff of 50 Ry (wavelength, λ = 0.4 Å) is used. AIMD simulations are performed under an NVT ensemble at 297 K with a tolerance of ±20 K to rescale velocities with a time step (τ) of 1 fs. Charge transfer is studied using the Bader charge analysis,[58-60] which allocates the electronic charge of an atom from the total charge enclosed within surfaces of minimum charge density, i.e., within zero flux surfaces. (Bader volume).

Typically, in molecular systems, the charge density reaches a minimum between atoms and this is a natural place to define the border between atoms.

CMD simulations are performed using the Large-Scale Atomic/ Molecular Massively Parallel Simulator (LAMMPS) program.[20] A velocity-Verlet integrator with a time step (τ) of 1 fs is used to calculate the trajectories of the particles in the motion equations. NPT ensembles are performed with Nosé-Hoover barostating every 500τ (0.5 ps). NVT ensembles are performed with a Nosé-Hoover thermostating every 1000τ (1 ps). Three dilute electrolyte boxes are built of initial molarities of 1 M, 2 M and 4 M. 1 M LiFSI solvated in TMP, the simulation box contains 27 LiFSI with 243 TMPs randomly distributed. The box size is 31.59 × 31.59 × 52.122 $Å^3$, corresponding to a density of 1.086 g cm−3 of pure TMP, which changed to 1.240 g cm−3 when the salt is added (Figs. 2.1) 2 M LiFSI solvated in TMP, the simulation box contains 27 LiFSI with 122 TMPs randomly distributed. The box size is 31.59 × 31.59 × 27.123 $Å^3$, corresponding to a density of 0.928 g cm^{-3} of pure TMP, which changed to 1.238 g cm^{-3} when the salt is added. 4 M LiFSI solvated in TMP, the simulation box contains 27 LiFSI with 54 TMPs randomly distributed. The box size is 31.59 × 31.59 × 12.123 $Å^3$, corresponding to a density of 0.519 g cm^{-3} of pure TMP, which changed to 1.212 g cm^{-3} when the salt is added.

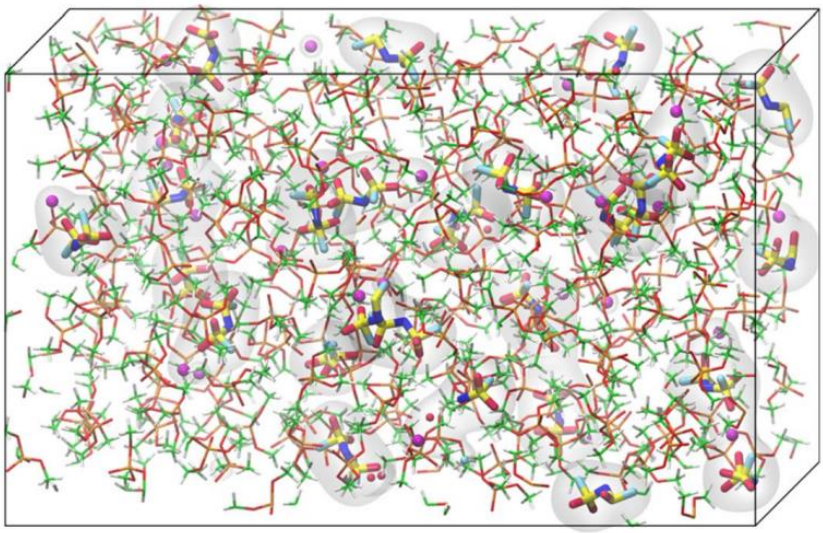

Figure 2.1 CMD simulation box for the LiFSI-TMP electrolyte corresponding to 1 M salt concentration ($LiFSI_{27}TMP_{243}$). Location of Li^+ and counter ions (gray shaded areas), Li (violet), N (blue), C (green), P (orange), H (white), F (cyan), S (yellow) and O (red). LiFSI = $F_2LiNO_4S_2$ and TMP = $(CH_3O)_3PO$.

2.4. Results and Discussion

Effect of concentration on electrolyte density.— We describe density behavior on 1 M, 2 M and 4 M LiFSI salt solvated in TMP from the CMD simulations and calculate the new salt concentration considering the simulated volume of each box. The simulation boxes were first equilibrated at 5 K in the NPT ensemble for 500 ps, then heated up to 300 K for other 500 ps and finally equilibrated at 300 K for 500 ps. Figure 4 shows the temperature and density for the three salt concentrations during the 1.5 ns under the NPT ensemble. In all three cases the density has changed after the final equilibration at 300 K due to the presence of the LiFSI salt. Since all the three cases were initialized from a totally unequilibrated structure created by considering the density of pure TMP (1.197 g cm−3), a change of the density was expected. The densities by the end of the equilibration at 300 K are 1.00 g cm^{-3} for 1 M, 1.07 g cm^{-3} for 2 M and 1.25 g cm^{-3} for 4 M. Therefore, the

computed salt concentrations changed to 0.70 M, 1.43 M and 3.82 M. The density of the whole electrolyte increases as the molarity increases. Table 2.1 shows the density at the different time frames of the CMD simulation in the NPT ensemble. From now on, we use the computed final salt concentrations to report our results.

Table 2.1 Simulation box density during the CMD simulation from 5 K to 300 K at the specific times: 0, 0.5, 1 and 1.5 ns.

	Box density (g cm-3)				
Initial salt concentration	0 ps	0.5 ns	1 ns	1.5 ns	Computed salt concentration
1 M	0.85	1.13	1.00	1.00	0.70
2 M	0.86	1.17	1.06	1.07	1.43
4 M	0.88	1.18	1.24	1.25	3.82

Effect of concentration in cumulative values of ions.— For a pair of atoms *i*–*j*, the time-averaged normalized radial distribution functions (RDF) is defined as:

$$g_{i,j} = \frac{n(r)}{\rho 4\pi r^2 dr} \tag{2.1}$$

where, ρ is the bulk number density, $n(r)$ is the number of *j*-atoms located in a differential volume $4\pi r^2 dr$ at a radial distance r from the center of *i*-atom. The magnitude of $g_{i,j}(r)$ is a function of binning size for r. The coordination number is the cumulative value of the respective neighbor atoms at a given shell radius r_s:

$$CN = \int_{r_s}^{0} g(r) dr \tag{2.2}$$

At 0.70 M, Li^+ is preferentially coordinated with O_{TMP} and O_{FSI}, yielding the plateau observed at about 3 Å, and indicating the atoms belonging to the first solvation shell (Fig. 2.2a). To get the CN, we calculate the cumulative value at r_{min} from Table 2.2. For O_{FSI} and O_{TMP}, the r_{min} values are 3.15 and 3.17 Å, respectively, getting a $CN_{Li,O\text{-}TMP}$ equal to 3 and a $CN_{Li,O\text{-}FSI}$ equal to 1. Therefore, the most recurrent geometry observed at 0.70 M is the Li^+ around three O_{TMP} and one O_{FSI} (Fig. 2.2b).

Table 2.2 RDF first peak radial position of maxima (r_{max}) and first minima (r_{min}) after its first peak of all atomic pairs and salt concentrations of the TMP-LiFSI electrolyte.

	0.70 M		1.43 M		3.82 M	
Ion pair	r_{max}/Å	r_{min}/Å	r_{max}/Å	r_{min}/Å	r_{max}/Å	r_{min}/Å
Li^+–F	3.87	4.97	3.95	4.82	3.87	5.07
Li^+–S	3.22	3.97	3.22	4.02	3.27	3.87
Li^+–O_{TMP}	1.72	3.17	1.67	3.05	1.72	2.95
Li^+–N	4.12	6.85	4.17	5.52	4.35	6.67
Li^+–O_{FSI}	1.82	3.15	1.82	3.25	1.82	3.35
Li^+–H	3.97	6.65	3.92	6.55	3.95	6.65
Li^+–C	4.62	6.35	4.62	6.35	4.62	6.35
Li^+–P	3.27	5.25	3.27	5.15	3.28	4.75
Li^+–Li^+	6.17	9.95	6.22	9.55	5.82	7.55

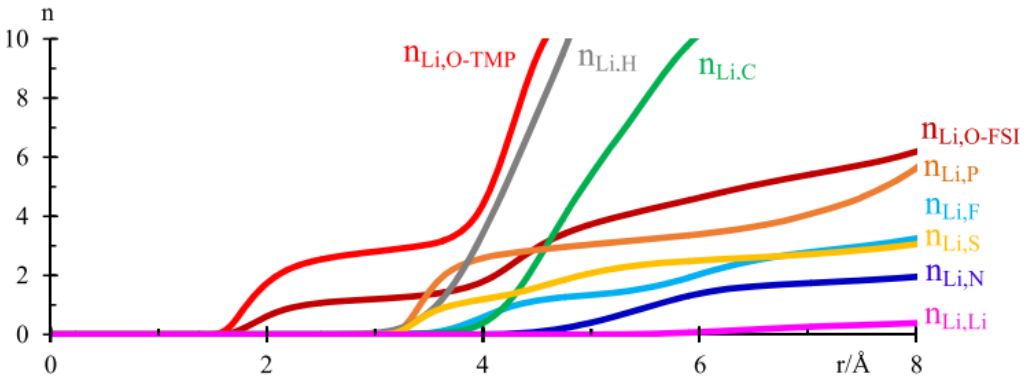
n
10
8
6
4
2
0
0
2
4
6
r/Å
8
n_Li,O-TMP
n_Li,H
n_Li,C
n_Li,O-FSI
n_Li,P
n_Li,F
n_Li,S
n_Li,N
n_Li,Li

(a)

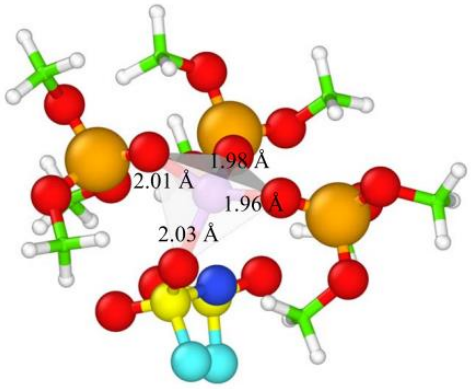
1.98 Å
2.01 Å
1.96 Å
2.03 Å

(b)

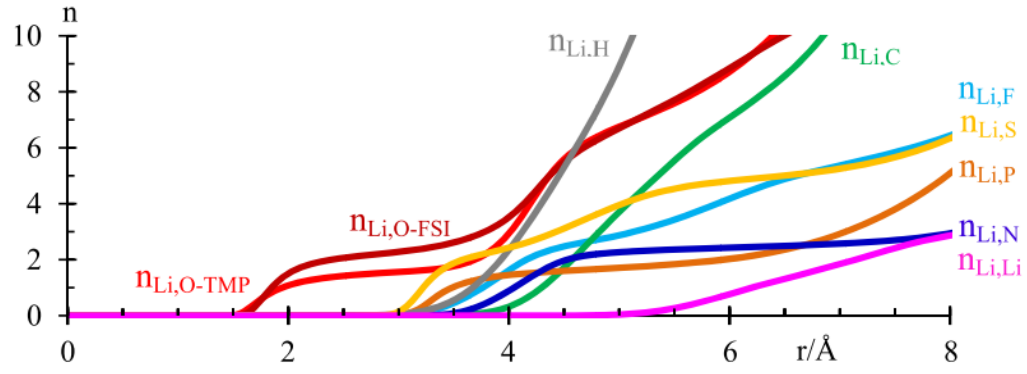
n
10
8
6
4
2
0
0
2
4
6
r/Å
8
n_Li,H
n_Li,C
n_Li,F
n_Li,S
n_Li,P
n_Li,O-FSI
n_Li,N
n_Li,Li
n_Li,O-TMP

(c)

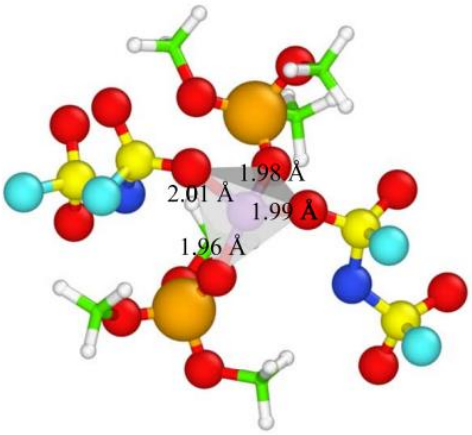
1.98 Å
2.01 Å
1.99 Å
1.96 Å

(d)

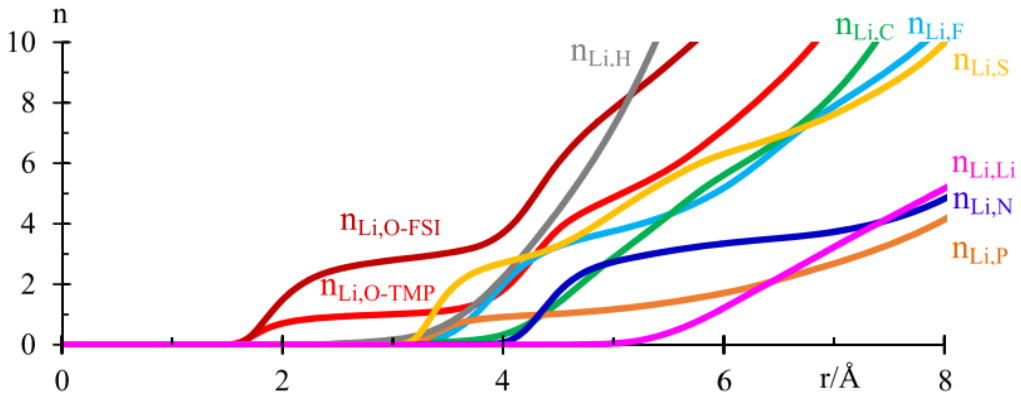
n
10
8
6
4
2
0
0
2
4
6
r/Å
8
n_Li,H
n_Li,C
n_Li,F
n_Li,S
n_Li,Li
n_Li,N
n_Li,P
n_Li,O-FSI
n_Li,O-TMP

(e)

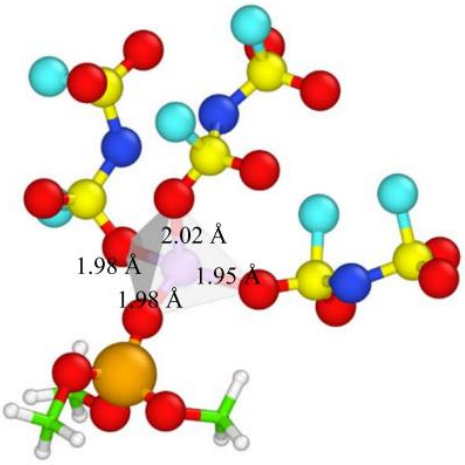
2.02 Å
1.98 Å
1.95 Å
1.98 Å

(f)

Figure 2.2 Cumulative numbers (n) of all the electrolyte constituents around Li+ ions at (a) 0.70 M, (c) 1.43 M and (e) 3.82 M. Most recurrent conformation of electrolyte constituents around Li+ ions at (b) 0.70 M, (d) 1.43 M and (f) 3.82 M. Li (violet), N (blue), C (green), P (orange), H (white), F (cyan), S (yellow) and O (red)

Similarly, to the 0.70 M case at 1.43 M, Li^+ is preferentially coordinated with O_{TMP} and O_{FSI} given the plateau observed at about 3 Å, indicating the atoms belonging to the first solvation shell (Fig. 2.2c). For OFSI and O_{TMP}, the r_{min} values from Table 2.2 are 3.05 and 3.25 respectively, getting a $CN_{Li,O\text{-}TMP}$ equal to 2 and a $CN_{Li,O\text{-}FSI}$ equal to 2. Therefore, the most recurrent geometry observed at 1.43 M is the Li^+ around 2 O_{TMP} and 2 O_{FSI} (Fig. 2.2d). At 3.82 M, Li^+ is still preferentially coordinated with O_{TMP} and O_{FSI} given the plateau observed at about 3 Å, indicating the atoms belonging to the first solvation shell (Fig. 2.2e). For O_{FSI} and O_{TMP}, the r_{min} values from Table 2.2 are 2.95 and 3.35, respectively, getting a $CN_{Li,O\text{-}TMP}$ equal to 1 and a $CN_{Li,O\text{-}FSI}$ equal to 3. Therefore, the most recurrent geometry observed at 3.82 M is the Li^+ around one O_{TMP} and three O_{FSI} (Fig. 2.2f). From the cumulative value analysis, we can establish that the first solvation shell of Li^+ is mostly composed by 4 O atoms in a tetrahedral conformation, regardless of electrolyte salt concentration. Li^+ coordinates preferentially with four oxygen atoms in a tetrahedral conformation. This is similar to the coordination of Li in Li_2O; however, considering the ratio r_{cation}/r_{anion} of Li^+ and O_{2-} ions (0.74 Å[61] and 1.4 Å,[62] respectively) yields a ratio of 0.52, which is larger than 0.414 and corresponds to an octahedral site; therefore, a relatively large covalent component is expected in the formation of the SEI.

From the cumulative value analysis, we observe that the tetrahedral configuration does not change regardless of electrolyte salt concentration (Fig. 2.2). The most common

Li-coordination in the 0.70 M is the one with three O from three TMPs and one O from an FSI^- ; in the 1.43 M, two O from two TMPs and two O from two FSI^- ; and in the 3.82 M, one O from one TMP and three O from three FSI^-.

Effect of salt concentration on transport properties.— We calculate the diffusivity (D) to analyze the pace at which a particle or molecule is transported in the electrolyte. The D can be computed from the mean square displacement (MSD) of the particles. In a long period of time, the MSD is given by:

$$\text{MSD} = \langle [r(t) - r(0)]^2 \rangle \tag{2.3}$$

and varies linearly with time *t*, and it can be related to the D (in a three-dimensional space) using Einstein's relation:

$$\text{D} = \lim_{t \to \infty} (MSD/6t) \tag{2.4}$$

and varies linearly with time *t*, and it can be related to the D (in a three-dimensional space) where r(t) denotes the position of a particle at time t. $\langle\ \rangle$ indicates ensemble average. We compute the diffusion coefficients of the electrolyte components (D_{TMP}, D_{Li} and D_{FSI-}) at 0.70 M, 1.84 M and 3.82 M salt concentrations (Table 2.3).

Table 2.3 Diffusion ($cm^2\ s^{-1}$) coefficients of the electrolyte components: TMP, FSI and Li, at 0.70 M, 1.43 M and 3.82 M salt concentrations.

	0.7 M	1.43 M	3.82 M
Solvent	1.43E-05	6.93E-06	1.35E-07
Li	2.32E-06	2.14E-06	2.75E-08
FSI^-	3.66E-06	2.15E-06	8.08E-08

Figure 2.3 shows the ratios of diffusion coefficients (D_{Li}/D_{TMP}, D_{Li}/D_{FSI-} and D_{FSI-}/D_{TMP}) and are compared with other similar electrolytes. $D_{Li}/_{DFSI-}$ is greater than the unity for the 0.70 and 1.43 M, but less than one for the 3.82 M (Fig. 2.3a). This indicates that the Li-ions diffuse more than the counter ion for the 0.70 and 1.43 M electrolytes, but the counter-ion diffuses more than the Li for the 3.82 M electrolyte. From the ion-pairing analysis, at 0.70 and 1.43 M, most of the ionic pairs founded are SSIP and CIP, however at 3.82 M, most of the ionic pairs are AGG, indicating that the Li are in contact with more than one counter ion in their inner shell, causing a change on the Li diffusion mechanism. Given the formation of AGGs, both ions diffuse together at higher concentrations.

D_{FSI-}/D_{TMP} are always less than one no matter the salt concentration (Fig. 2.3b). However, a trend is observed, as the salt concentration increases the D_{FSI-}/D_{TMP} also increases, indicating that at high salt concentration the diffusion of the counter-ions with respect to the solvent is increasing. We can explain the change on the diffusion rate due to the formation of AGG, in which several counter ions are in a close proximity and without enough TMP to solvate them. Strong coulombic interactions between the ions could affect the diffusivity of the FSI−, causing the increase in the D_{FSI-}/D_{TMP} ratio. Similarly, to the counter-ion, the D_{Li}/D_{TMP} are always less than one independently of the salt concentration (Fig. 2.3c). Due to the presence of CIP for the 0.70 M and 1.43 M electrolytes, and AGG for the 3.42 M electrolyte, the Li-ions diffusivity is limited by the counter-ion diffusivity.

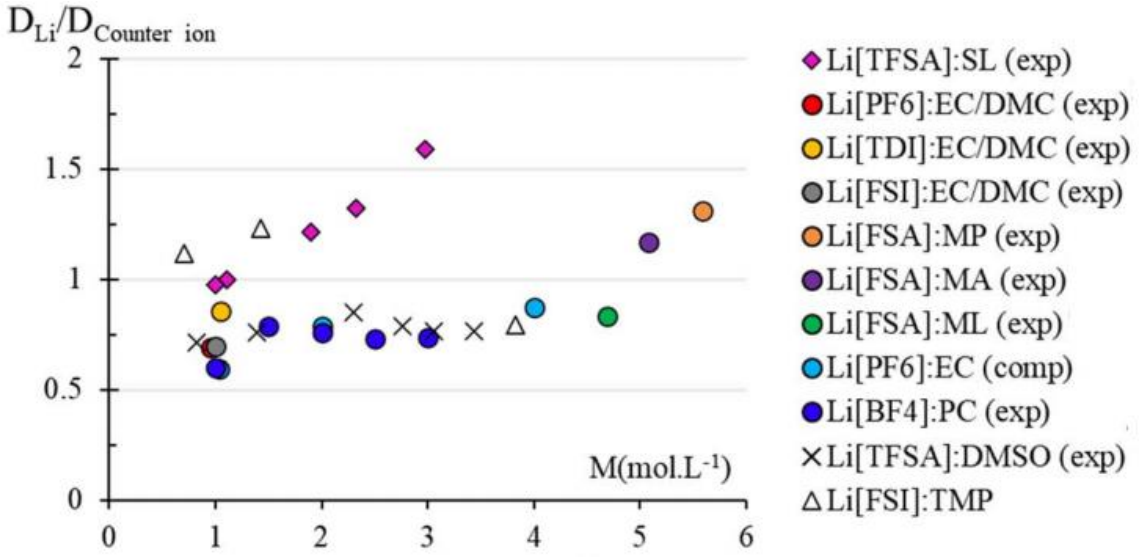
$D_{Li}/D_{Counter\ ion}$
2
1.5
1
0.5
0
0
1
2
3
4
5
6
M(mol.L^{-1})
Li[TFSA]:SL (exp)
Li[PF6]:EC/DMC (exp)
Li[TDI]:EC/DMC (exp)
Li[FSI]:EC/DMC (exp)
Li[FSA]:MP (exp)
Li[FSA]:MA (exp)
Li[FSA]:ML (exp)
Li[PF6]:EC (comp)
Li[BF4]:PC (exp)
Li[TFSA]:DMSO (exp)
Li[FSI]:TMP

(a)

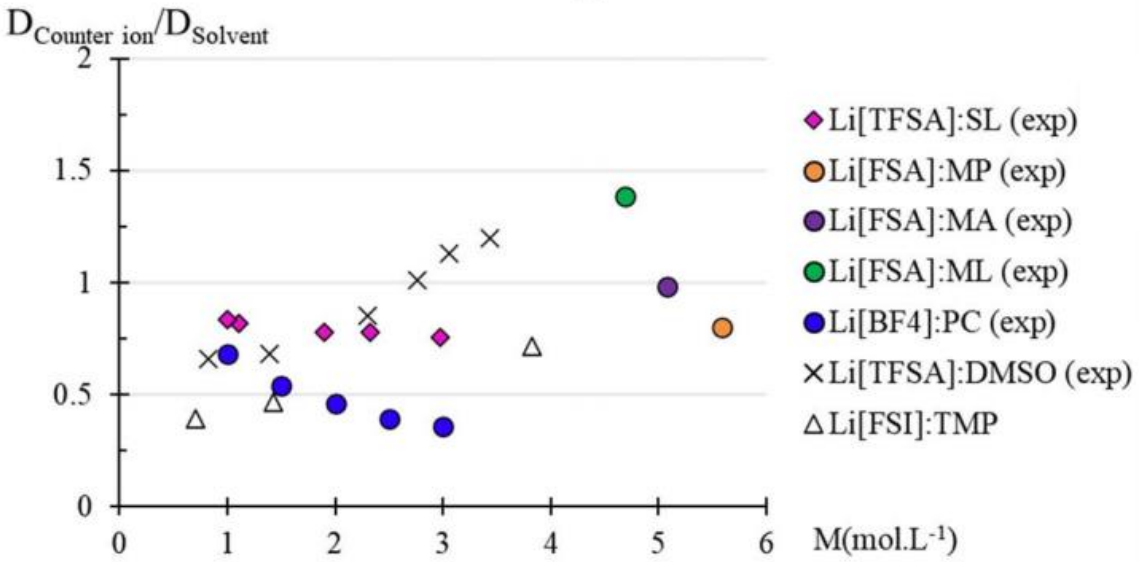
$D_{Counter\ ion}/D_{Solvent}$
2
1.5
1
0.5
0
0
1
2
3
4
5
6
M(mol.L^{-1})
Li[TFSA]:SL (exp)
Li[FSA]:MP (exp)
Li[FSA]:MA (exp)
Li[FSA]:ML (exp)
Li[BF4]:PC (exp)
Li[TFSA]:DMSO (exp)
Li[FSI]:TMP

(b)

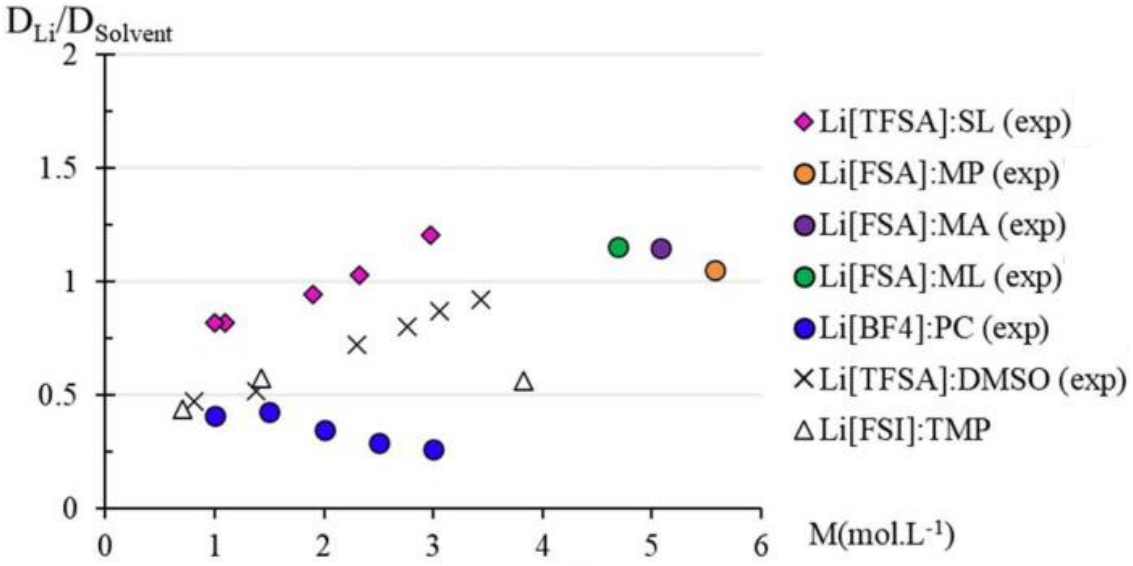

(c)

Figure 2.3 Diffusion coefficients ratios within the electrolyte components: (a) $D_{Li}/D_{Counter\text{-}ion}$, (b) $D_{Counter\text{-}ion}/D_{Solvent}$ and (c) $D_{Li}/D_{Solvent}$ from several similar electrolytes and the 0.70 M, 1.43 M and 3.82 M LiFSI-TMP electrolytes calculated in the present work.

In general, a change on the diffusion mechanism of the Li-ions occurs as the salt concentration on the electrolyte increases. For low salt concentrated electrolytes, the diffusion of Li-ions mostly follows a hopping/exchange mechanism, wherein Li ions diffuse from one coordinating site (on either solvent or the anions) to another vacant site through ligand exchange in the labile Li-ion coordination chains. As the salt concentration increases a vehicular mechanism premising translational motion of the AGG formed by Li-ions and FSI^- counterion is observed.

Conductivity analysis.— In the previous section a diffusion analysis of the ions was developed to understand their mobility through the solvent. However, effects involving charge transfer cannot be explained only from a diffusion analysis. The rate at

which the electrolyte conducts the charges is an important quantity to consider in the development and test of new electrolyte materials because it influences in the charge-discharge rates performance of the full battery. Ionic conductivity (σ_i) quantifies how good is the charge transfer rate: ions conduction. The ionic conductivity is not suitable to compare electrolytes containing different salt concentration, since the ionic conductivity depends on all the effective ion species in the electrolyte. Instead, we first calculate the molar conductivity (Λ) which is the property of an electrolyte solution that quantifies the efficiency of a given electrolyte in conducting electricity in a solution. Then, we can calculate the ionic conductivity (σ_i) from the molar conductivity (L) given:

$$\sigma_i = c\Lambda \tag{2.5}$$

where c is the salt concentration in moles per liter. In Fig. 11, we are showing the molar (Fig. 11a) and ionic (Fig. 11b) conductivity vs salt concentration, calculated for the LiFSI-TMP in the present work, and compared with several other similar electrolytes. We are using the 2.5 formula to convert from ionic to molar conductivity for the cases in which only one of the conductivities is reported. The molar conductivity (Λ) can be obtained from the collective mean square displacement of the ions in the solution using Einstein's relation: ∞·

$$\Lambda = \frac{N_A e^2}{6nk_BT} \lim_{t\to\infty} \frac{d}{dt} \sum_i \sum_j z_i z_j \langle \Delta r_i \cdot \Delta r_j \rangle \tag{2.5}$$

where N_A is Avogadro's number, e is an electron charge, n is the total number of ions (cations and anions), k_B is Boltzmann constant, and z_i is the charge on ion i. Δr_i is the displacement of ion i. The Einstein relation contains cross terms that account for the correlation of the anions and cations in the electrolyte.

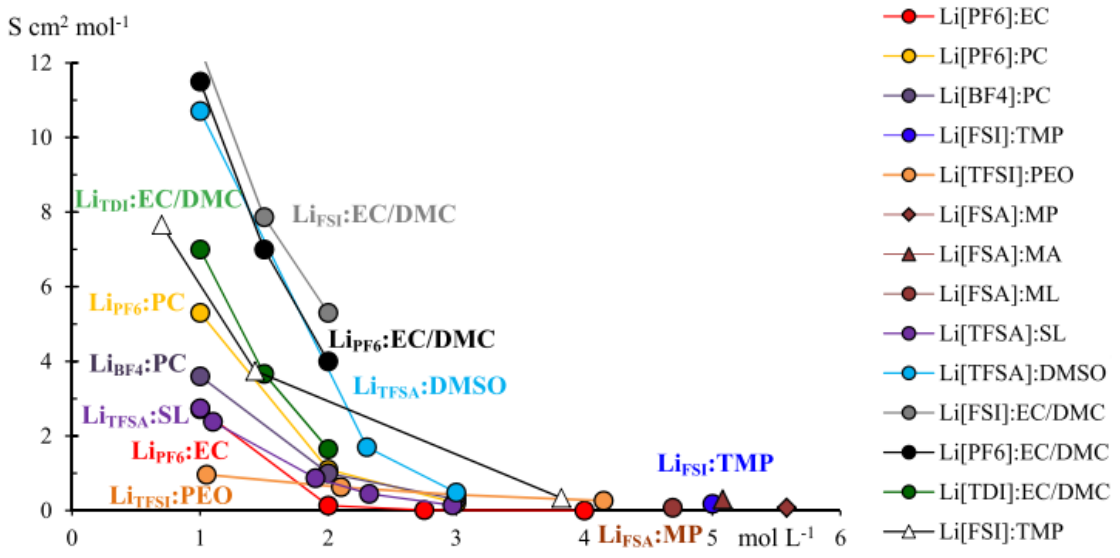

(a)

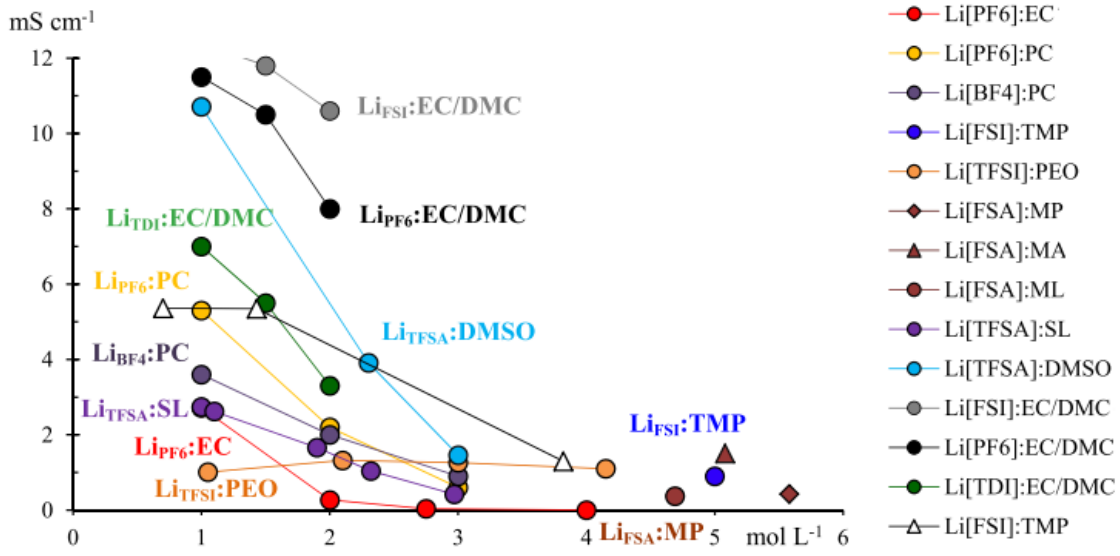

(b)

Figure 2.4 (a) Molar conductivity and (b) Ionic conductivity from several electrolytes and the 1 M, 2 M and 4 M LiFSI/TMP electrolytes calculated in the present work.

The computed molar conductivities are 7.66, 3.74 and 0.22 S cm^2 mol^{-1} for the 0.70 M, 1.43 M and 3.82 M salt concentration, respectively. The molar conductivity,

similar to diffusivity of ions, also decreases as the salt concentration increases. In Fig. 2.4a we are also plotting several other molar conductivities for similar electrolyte systems. Our molar conductivity calculation follows the general trend observed in Fig. 2.4a, the molar conductivity decreases as the concentration increases. The interplay between the number of available charge carriers and their ability to carry the charge defines the concentration for optimal performance.

The computed ionic conductivities are 5.36, 5.34 and 1.29 mS cm^{-1} for the 0.70 M, 1.43 M and 3.82 M salt concentration, respectively (Fig. 2.4b). The 5.36 and 5.34 mS cm^{-1} conductivities, corresponding to the 0.7 M and 1.43 M, could indicate that the maximum conductivity value of a LiFSI-TMP electrolyte is achieved in a concentration between 0.7 M and 1.43 M. An experimental value of 0.9 mS cm^{-1} have been reported for a 5 M LiFSI in pure TMP electrolyte,[43] which is consistent with the simulation results presented. However, we have to clarify that making a comparison between experimental results and simulations is difficult since the ion diffusion coefficients are hard to measure experimentally. However, we can establish two reason that could explain a discrepancy between experimental and computational results: ionic conductivity from simulation could overpredict the correlated ion movement, and the use of a polarizable force field might improve the calculation of the ionicity behavior.[63-65]

Clustering of Li-ions and FSI^- anions.— Analysis of the ion pairing and its classification as SSIP, CIP or AGG are limited by the radial space. The analysis of ionic clusters is necessary to have a bigger analysis to understand the diffusivity of Li-ions. In the ion pairing analysis, all the data is based on the neighbors around Li-ions, however,

we do not have much information of how these Li-ions interact between them or with the FSI counter-ions. For the purpose of this study, we define an ionic cluster as a group of ions in a distance less than 2.5 Å between cation- cation, cation-anion and anion-anion. The threshold distance of 2.5 Å is established from the RDF analysis showed in previous section of this work. For every time step there are a set of clusters connected through different topologies. A cluster topology indicates how the ions are connected. For example, a cluster containing 3 FSI– and 3 Li can show an open chain structure or a closed ring structure: Li-FSI-LiFSI-Li-FSI, or a branched structure such as Li-2FSI-Li-FSI-Li. The formation of neutral charged clusters, when the number of Li ions and counter ions are the same in the cluster, may offset gains in conductivity expected with increased salt concentration. The extent of this effect will be influenced by the characteristic lifetime of individual clusters.

2.5. Conclusions

We study the LiFSI-TMP electrolyte for 0.70 M, 1.43 M, and 3.82 M salt concentrations performing CMD simulations, which can capture the static and dynamic properties of the electrolyte solution. As the salt concentration increases, diffusivity of both ions, Li^+ and FSI^-, decreases. CNs were estimated by analyzing the cumulative distributions obtained from the integration of the RDFs, indicating that Li^+ is most likely coordinated to four molecules regardless of salt concentration; however, the salt concentration determines the ratio between solvent and counter-ions in the first shell of Li^+. In the 0.70 M dilute electrolyte, we find a mixture of SSIP and CIP; at 1.43 M, some AGGs appear and there are not more SSIP leaving the CIP as the most dominant ion pair;

at 3.82 M, AGGs becomes the most dominant ion pair by less than 5% with respect to the CIP.

An analysis of most radial distribution functions involving the ion and counterion suggests that the number of free TMP molecules in the solution is depleted as the salt concentration increases, allowing the formation of salt-solvent complexes affecting the electrolyte overall conductivity. Ideally speaking, the solvent should be able to minimize the ion pairing. However, as the salt concentration increases, the formation or ion-pairs such as CIP or AGGs, and even large clusters, is inevitable, directly affecting the ion diffusion mechanism and the ionic conductivity of the electrolyte. Results indicate that as the salt concentration increases a drop in the transport properties such as diffusivity and conductivity is observed.

From the ion-pair analysis we identified AGGs and CIP as the most recurrent ion-pairing. However, these ion pairs are part of one single ionic cluster. The ionic clusters present different topologies, we identified three: chainlike, ringlike, and branchlike. In all of them the Li-ions are bridged by the FSI counter-ions. At 0.70 M, no ionic clusters are observed, only CIP or SSIP. As the salt increases up to 1.43 M, some small chainlike and ringlike ionic clusters are formed, usually composed by 2 or 3 ionic pairs. The formation of ionic clustering is more critical as the salt concentration increases forming one single ionic cluster at 3.82 M.

Since at low concentration such as 0.7 M, the Li-ions are SSIP or CIP, the Li-ion hopping diffusion mechanism, travelling from shells composed of solvent molecules or anions, is the dominant diffusion mechanism. As the concentration increases and due to

the formation of chainlike, ringlike, and branchlike ionic clusters and AGGs, a diffusion mechanism ruled by anion-solvent exchange or diffusion of a whole positively charge cluster is observed instead of the hopping diffusion mechanism, decreasing the ionic diffusion and molar conductivities.

3. CHAPTER III LI-METAL ANODE IN DILUTE ELECTROLYTE LIFSI/TMP: ELECTROCHEMICAL STABILITY

3.1. Synopsis

Identifying the mechanism of SEI formation at electronic and atomic levels is especially important to understand how the SEI formation affects the overall battery performance such as the decrease of active material, decrease of cell potential, and interfacial stability. Ab initio molecular dynamics simulations were performed for Li+-conducting electrolytes based on trimethyl phosphates (TMP) and lithium bis(fluorosulfonyl)imide (Li^+FSI^-) salt in contact with a Li-metal electrode. We focused on the transient-state behavior at the electrolyte, interfacial electrolyte−Li-metal electrode, and lithium reference electrode−electrolyte−Li-metal electrode to study dynamics and activation energy barriers of the Li^+ ion, electrochemical and thermal stability of the interface electrode−electrolyte, and potential behavior of the Li-metal electrode, respectively.

3.2. Introduction

Current commercial rechargeable Li^+-ion batteries (LIBs) are mainly made of hexafluorophosphate ($LiPF_6$) salt dissolved in carbonate liquids (CLs).

---

*Reprinted with permission from:

Li-Metal Anode in Dilute Electrolyte LiFSI/TMP: Electrochemical Stability Using Ab Initio Molecular Dynamics by D. E. Galvez-Aranda, J. M. Seminario, 2020. The Journal of Physical Chemistry C, 2020, vol. 124, no 40, p. 21919-21934.

Linear carbonates such as ethyl methyl carbonate (EMC) or diethyl carbonate (DEC) are used as solvents keeping the electrolyte viscosity low and the electrolyte conductivity high.

Unfortunately, these $LiPF_6$/CL electrolytes are highly volatile and flammable,[66] especially in abused conditions such as overcharging and overheating. Therefore, it is necessary to develop novel electrolytes accomplishing all of the safety issues as well as electrochemical stability with electrodes. Organic phosphorus-based compounds are being tested, looking for new dilute electrolytes (DEs) due to their good flame-retarding ability and low cost.[34] Trimethyl phosphate (TMP) is being investigated as a sole solvent to replace carbonate solvents in LIBs.[34-35, 67] The main safety issue regarding the electrolytes used in commercial batteries is that they may catch fire when the battery is operated under abused conditions such as overcharging, overheating, and short-circuiting.[2, 68]

Unfortunately, commercial electrolytes present flashpoints around room temperature. Therefore, this commercial electrolyte can ignite given a thermal runaway that may occur by an external and/or internal stimulus such as overcharging the battery beyond the maximum allowed voltage, excessive currents during rapid charging, and deformation of the battery cell causing short circuits.[68]

One of the potential solutions to mitigate the fire hazard in electrolytes is adding nonflammable compounds or flame-retardant additives such as TMP. However, the addition of new compounds in the electrolyte affects the electrochemical performance of the battery. For example, TMP electrolytes cannot passivate carbonaceous electrodes, which are the most common electrodes used in commercial batteries.[44] The use of more

TMP additives can decrease the flammability of the cell but simultaneously degrades the charge−discharge cycle ability, especially when carbon electrodes are used.[44] The concentration salt/solvent can modify the overall performance of the electrolyte, decreasing TMP decomposition at the interface of the electrolyte/electrode. In a DE solution, a Li^+ ion is coordinated, on average, with three or four solvent molecules.[43] A DE is dominated by solvent-separated ion pairs and free solvent molecules. As the concentration of salt increased, we have a concentrated electrolyte, typically when the molarity exceeds 3 M. In a concentrated electrolyte, the Li^+ ion is coordinated, in average, with one or two solvent molecules.[43]

Another key aspect in the potential use of TMP-based electrolytes is the electrochemical stability in contact with the electrodes. Battery performance strongly depends on the solid electrolyte interface (SEI) film, which can profoundly modify several observables such as Coulombic efficiency, rate capability, cycling life, and safety;[18-19] therefore, it is extremely important to study the composition of the SEI film. Experimental work such as in situ and in operando experiments requires modifications of the operating conditions of the battery to perform multiple measurements in the same device at the same time; therefore, experimental conditions are different from operating conditions of the battery, for this reason, the use of computational tools is necessary to elucidate the structural, dynamical, and reactive behavior of LiFSI/TMP electrolytes in contact with a Li-metal electrode. Therefore, identifying the mechanism of SEI formation at electronic and atomic levels is very important to understand how the SEI formation affects the overall

battery performance such as the decrease of active material, decrease of cell potential, and interfacial stability.

In this work, we perform first-principles calculations to provide insights on the thermodynamics, kinetics, and electrochemical stability when a dilute 1 M LiFSI/TMP electrolyte is in contact with a Li-metal electrode. Degradation in Li-ion batteries due to loss of an active electrode material has measurable effects on the open-circuit potential,[69] which requires an additional electrode or reference electrode. Ideally, a reference electrode should be (1) electrochemically reversible, i.e., its potential is governed by the Nernst equation and does not change in time, and (2) nonpolarizable, i.e., its potential must remain constant when a current passes through the electrode and keeps its initial value after such current stops.[70] Experimentally, the use of reference electrodes in Li-ion batteries has been challenging due to safety considerations associated with the risk of short circuits, no matter if a two-electrode or a three-electrode cell configuration is used for the electrochemical testing.[71] Short circuits can occur from a variety of sources, including manufacture impurities, dissolution, and deposition of electrode materials, causing separator damage or solder splatter at electrode connection.[72] Also, no electrode can be completely stable since once they are part of the battery circuit, they are in contact with the other components, i.e., electrolyte or current collectors, and some degradation is expected. In lithium-ion batteries, lithium metal is usually the reference electrode of choice due to its stability.[73] In the present work, a lithium reference electrode (LRE) is used to calculate the open-circuit potential energy (OCPE) characteristics of the Li-metal electrodes throughout the SEI formation. The actual calculation by atomistic quantum mechanical first principles

methods of the potential difference between the cathode and anode plays a significant role in the design and selection of battery materials to improve their performance. In these calculations, we focus on the creation and effects on the SEI due to such potentials.

3.3. Methodology

In the present work, we perform ab initio molecular dynamics (AIMD) simulations of a phosphate-based electrolyte composed of 1 M LiFSI in TMP. We study the 1 M LiFSI/TMP electrolyte in three systems: (1) electrolyte system: to study transport mechanism, diffusion, and activation energy barriers of the Li^+ ions, (2) interfacial electrolyte−Li-metal electrode system: to study electrochemical and thermal stability and composition of the formed SEI, and (3) lithium reference electrode−electrolyte−Li-metal electrode system: to study the potential behavior of the Li-metal electrode.

In the electrolyte system, one dilute electrolyte box ($10.53 \times 10.53 \times 17.374$ $Å^3$) was used containing one LiFSI and nine TMP, corresponding to a 1 M salt solution in TMP (Figure 3.1a).

In the interfacial electrolyte−Li-metal electrode, three Li-metal/dilute electrolyte boxes of $10.53 \times 10.53 \times 28.01$ $Å^3$ contain a slab of dilute electrolyte made of one LiFSI and nine TMP, corresponding to 1 M electrolyte in contact with a Li-metal surface. To represent the randomness of the system, three initial configurations are tested positioning the ion pair at distinct distances from the lithium anode: contact ion pair (Model I), separated ion pair (Model II), and solvated ion pair (Model III). In the contact ion pair, the LiFSI is initially in contact with the Li-metal electrode. In the separated ion pair, the FSI^- and the Li^+ are in contact with the Li-metal but in different faces. In the solvated ion pair,

the Li^+ and FSI^- are separated and solvated at the center of the electrolyte, avoiding direct contact with the Li-metal electrode (Figure 3.1b). In all cases, the plane of the Li-metal facing the solvent is (100).

For the lithium reference electrode−electrolyte−Li-metal electrode system, three LRE/DE/Li-metal boxes of 10.53 × 10.53 × 40.0 $Å^3$ are built adding a lithium reference electrode (LRE). The box periodicity is broken along the longitudinal axis by adding a vacuum region next to the LRE, avoiding in this way, contact between the Li-metal and the LRE. We use a two-electrode cell configuration, where the counter electrode also acts as the reference electrode and the working electrode is the Li-metal electrode. The reference electrode is always a pristine crystal preserving its original potential since it does not participate in the dynamics of the cell, only single-points calculations, avoiding a possible decrease in the potential due to interfacial reactions between the LRE and the electrolyte (Figure 3.1c).

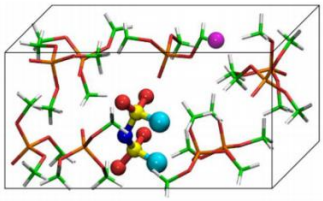

(a)

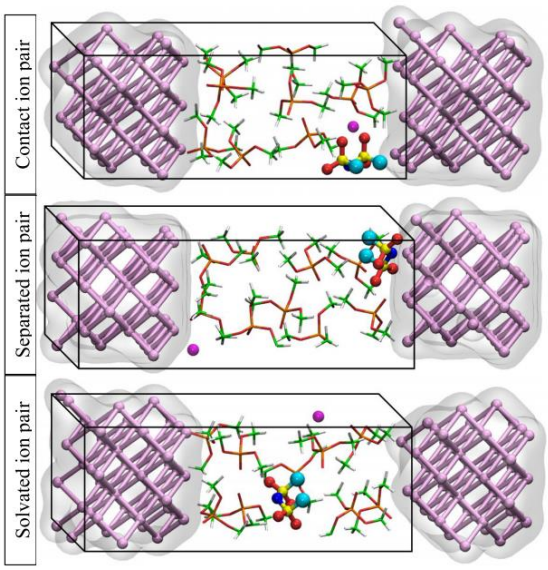

(b)

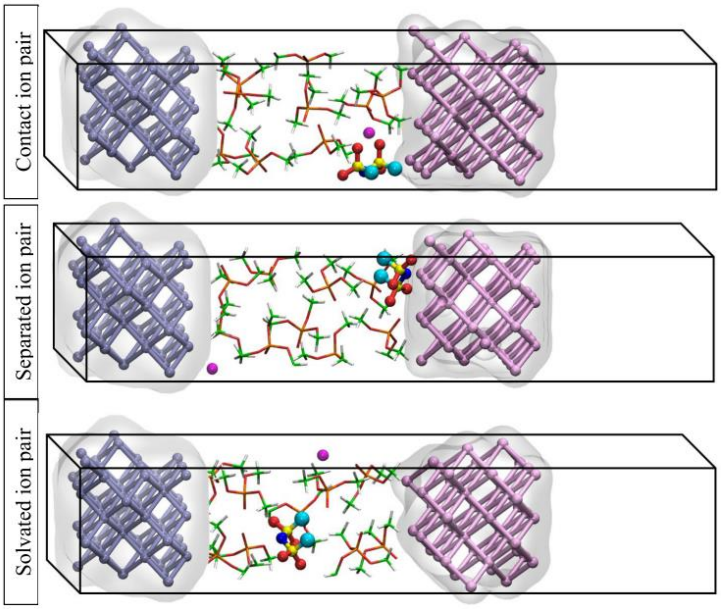

(c)

Figure 3.1 Initial simulation cells of (a) electrolyte; (b) interfacial electrolyte−Li-metal electrode, Model I: contact ion-pair salt in contact with Li-metal, Model II: separated ion-pair salt in contact with Li-metal, Model III: solvated ion-pair salt at the center of the electrolyte avoiding contact with the Li-metal; and (c) LRE−electrolyte−Li-metal electrode system. LRE (gray), Li-metal (violet), N (blue), C (green), P (orange), H (white), F (cyan), S (yellow), and O (red).

Li-metal and LiFSI/TMP electrolyte are optimized separately using Born−Oppenheimer approximation with density functional theory (DFT) within the projector-augmented wave approach (PAW) to solve the electronic Schrödinger equation with the Perdew−Burke−Ernzerhof (PBE) functional. After the geometry optimization, an equilibration using AIMD of each cell is performed under the NPT ensemble, allowing volume relaxation of the structures at 1 atm and 297 K with a tolerance of ±20 K for 10 ps, setting a plane-wave energy cutoff of 50 Ry (wavelength, $\lambda = 0.4$ Å). After equilibrated separately, each cell component, the Li-metal/LiFSI−TMP interfacial system, is assembled. Due to periodic boundary conditions (PBCs), the simulation cell features a sandwich-like structure along the longitudinal direction. Then, a geometry optimization is performed. After the optimization, an equilibration of the interfacial system is performed for 20 ps under the NVT ensemble at 297 K with a tolerance of ±20 K to rescale velocities with a time step of $\tau = 1$ fs.

We perform single-point calculations for the LRE−electrolyte−Li-metal electrode system, with threshold values for energy and force of 10^{-6} eV and 10^{-11} N, respectively. The structures are taken every 0.5 ps from the AIMD interfacial electrolyte−Li metal electrode system simulations, adding an LRE next to the electrolyte and a vacuum region next to the Li-metal anode. All of the AIMD and SCF calculations described before are performed using the Quantum Espresso program.[54]

Using the atomic scale modeling techniques previously described, we can provide detailed information of the Li^+ migration pathways and their activation barriers. We also

systematically investigate the interface LiFSI−TMP/Li-metal to carry out a detailed survey of the reaction pathways, the extent of decomposition, charge distribution, structure, and composition of the decomposed fragments that form the SEI. We are also performing a study of the open-circuit potential energy (OCPE) of the Li-metal electrode to distinguish its contribution to the overall battery performance using a lithium reference electrode (LRE).

3.4. Results and Discussion

Electrolyte System. We observe one Li^+ coordinating with four molecules in the dilute electrolyte 1 M LiFSI/TMP at 300 K. The four molecules surrounding the Li^+ are four TMP molecules or three TMP molecules and one FSI^-. The remaining TMP exist in a free state, i.e., they do not react or form a new compound. Bader charge analysis yields a charge of 0.89 for Li^+ ion; thus, −0.89 for FSI^- (counterion) and ∼0 for each of the nine TMP. FSI^- and Li^+ can form ion-pair contacts; however, this does not occur frequently due to the large number of TMP surrounding the ions at 1 M concentration. Without the formation of contact ion pairs, Li^+ can freely move over the TMP because the Coulombic interactions between ions are screened by the presence of TMP, avoiding direct interaction between the ion and the counterion. The most stable state occurs when the Li^+ ion is surrounded by three TMP and the FSI^-. The most unstable state is when the Li^+ ion is surrounded by less than four molecules (3 TMP, 2 TMP + FSI^- or 1 TMP + FSI^-) coordinating with the oxygen atoms from those surrounding molecules. During the transition from the most stable to the most unstable state, the most frequently observed geometry is the Li^+ ion surrounded by four or less molecules (4TMP, 3 TMP + FSI^-, 2

TMP + FSI^- or 1 TMP + FSI^-) but coordinated with methyl groups instead of oxygens from those molecules. The amount of energy that Li+ ion needs to get out from the 3 TMP + FSI^- cage and get into the four TMP cages or the three TMP cages oscillates from 3 to 4 eV (Figure 3.2).

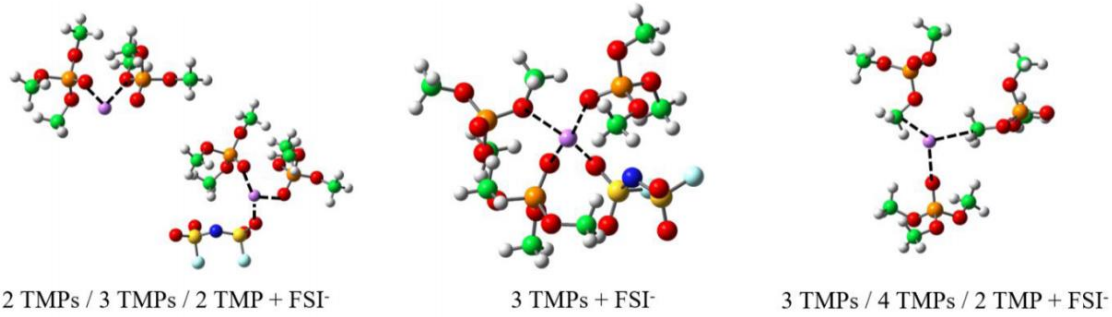

Figure 3.2 Solvation structures are identified, left: $TMP_2/TMP_3/TMP_2$ + FSI^-, center: TMP_3 + FSI^- and right: $TMP_3/TMP_4/TMP_2$ + FSI^-. Li (violet), N (blue), C (green), P (orange), H (white), F (cyan), S (yellow), and O (red).

Interfacial Electrolyte–Li-Metal Electrode System. LiFSI reduction mechanism and formation of an SEI layer are depicted in Figure 3.3. When the FSI^- counterion is in direct contact with the Li-metal, the salt reacts instantly, regardless of whether the ion pair is separated, Li^+ and FSI^- (Model II), or in contact, LiFSI (Model I). In both cases, the salt does not last the 15 ps of simulation time and has been completely dissociated in contact with Li-metal forming several Li binary compounds, such as Li_2O, Li_2S, Li_3N, and LiF. The reaction sequence begins with the defluorination of the salt at 0.1 ps, where the dissociated F^- reacts immediately with the Li-metal forming lithium fluoride. The defluorination also occurs when the salt is solvated with TMP molecules avoiding direct contact with the Li-metal (Model III). When the salt is solvated with TMP molecules, F^- remains as an anion in the electrolyte liquid phase, not forming new compounds during

the 15 ps of the simulation. After defluorination of the counterion in Models I and II, an SO_2 group breaks and lays on the surface of the Li-metal electrode. The S from the SO_2 group goes into deeper layers of the Li-metal electrode, breaking the original S−O bonds and forming new bonds with the Li from the metal. The decomposition of the SO_2 group into Li_2S and Li_2O occurs in a time lapse of 1−2 ps. The $FNSO_2^{2-}$ fragment, formed when SO_2 breaks, defluorinates after 0.2 ps of being formed. The remaining NSO^{2-} anion moves then to the surface where it gains two additional electrons and is reduced into its elemental constituents by the metal electrode forming Li binary compounds such as Li_3N, Li_2S, and Li_2O. Li_2S and Li_2O formation occur in the next 5−7 ps. Li_3N is the last composed formed, occurring at 9.50 and 12.70 ps for Models I and II, respectively. The reaction pathway in Models I and II is very similar, except for slight differences in time frames. The time frame reaction differences cannot be attributed exclusively to the initial separated or in contact state of the ion pair but also to the initial orientation of the LiFSI. A detailed list of the reaction sequence time frame is given in Table 3.1.

Table 3.1 Reaction Time Sequence of the FSI^- Decomposition in Contact with Li-Metal Electrode When Starting as a Contact Ion Pair (t_c) and as a Separated Ion Pair (t_s)

original bond	formed bond	t_c (ps)	t_s (ps)
S1−F	Li_s−F	0.05	0.07
S1−O1	Li_s−O	1.08	0.40
S1−O2	Li_s−O	1.09	0.80
S1−N	Li_s−S	0.87	0.30
S2−F	Li_s−F	1.06	0.50
S2−O3	Li_s−O	4.50	8.50
S2−O4	Li_s−O	8.20	8.90
S2−N	Li_s−S	9.50	12.70

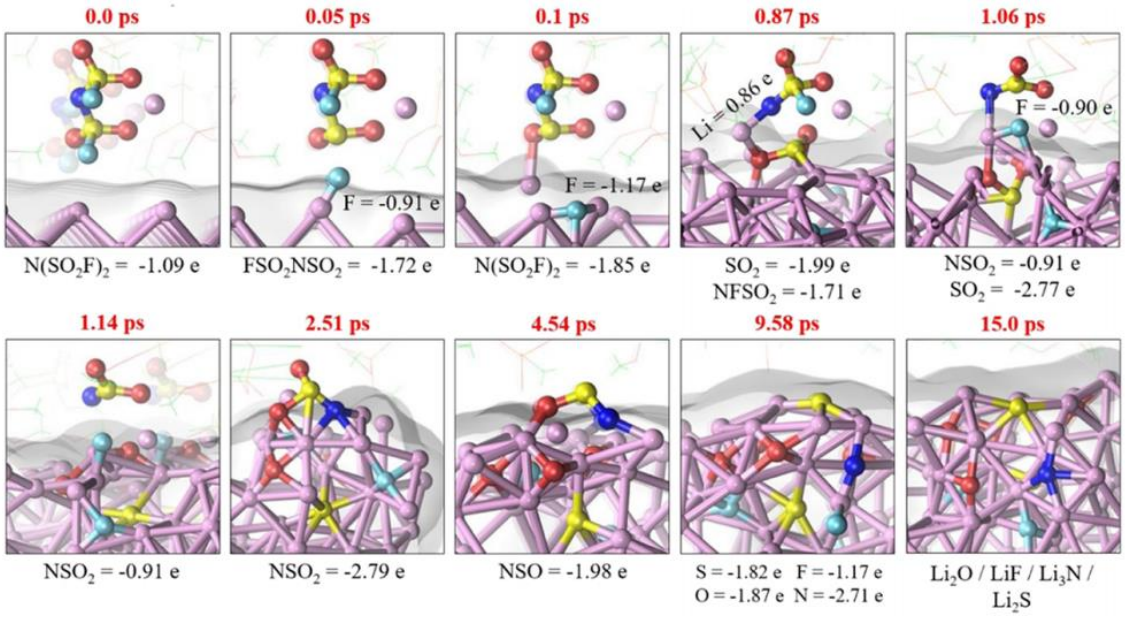
0.0 ps
0.05 ps
0.1 ps
0.87 ps
1.06 ps
F = -0.91 e
F = -1.17 e
Li = 0.86 e
F = -0.90 e
N(SO2F)2 = -1.09 e
FSO2NSO2 = -1.72 e
N(SO2F)2 = -1.85 e
SO2 = -1.99 e
NFSO2 = -1.71 e
NSO2 = -0.91 e
SO2 = -2.77 e
1.14 ps
2.51 ps
4.54 ps
9.58 ps
15.0 ps
NSO2 = -0.91 e
NSO2 = -2.79 e
NSO = -1.98 e
S = -1.82 e F = -1.17 e
O = -1.87 e N = -2.71 e
Li2O / LiF / Li3N /
Li2S

(a)

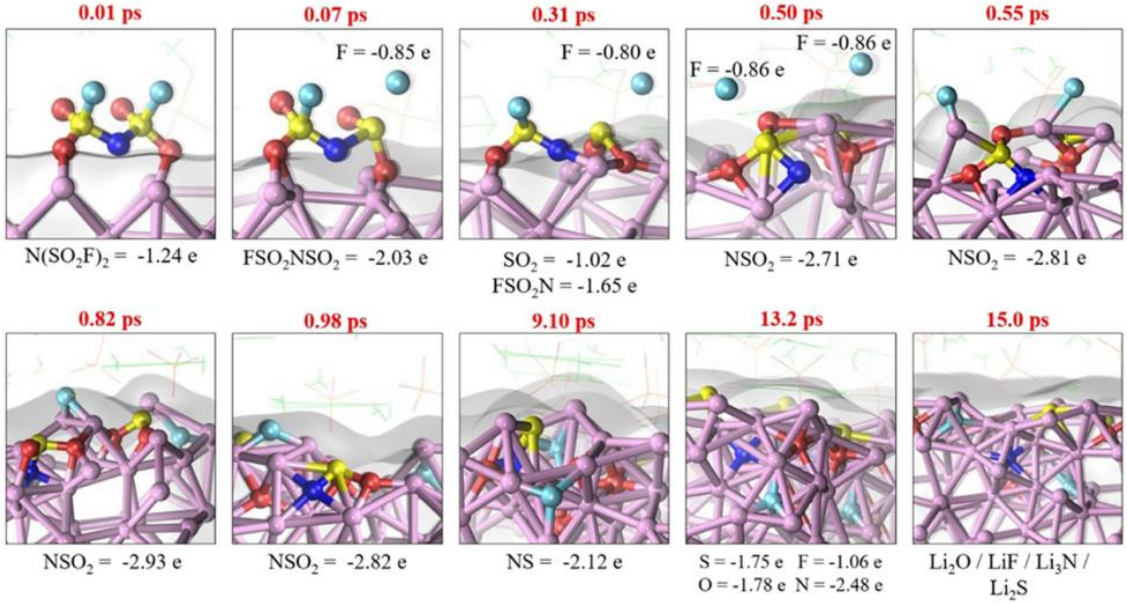
0.01 ps
0.07 ps
0.31 ps
0.50 ps
0.55 ps
F = -0.85 e
F = -0.80 e
F = -0.86 e
F = -0.86 e
N(SO2F)2 = -1.24 e
FSO2NSO2 = -2.03 e
SO2 = -1.02 e
FSO2N = -1.65 e
NSO2 = -2.71 e
NSO2 = -2.81 e
0.82 ps
0.98 ps
9.10 ps
13.2 ps
15.0 ps
NSO2 = -2.93 e
NSO2 = -2.82 e
NS = -2.12 e
S = -1.75 e F = -1.06 e
O = -1.78 e N = -2.48 e
Li2O / LiF / Li3N /
Li2S

(b)

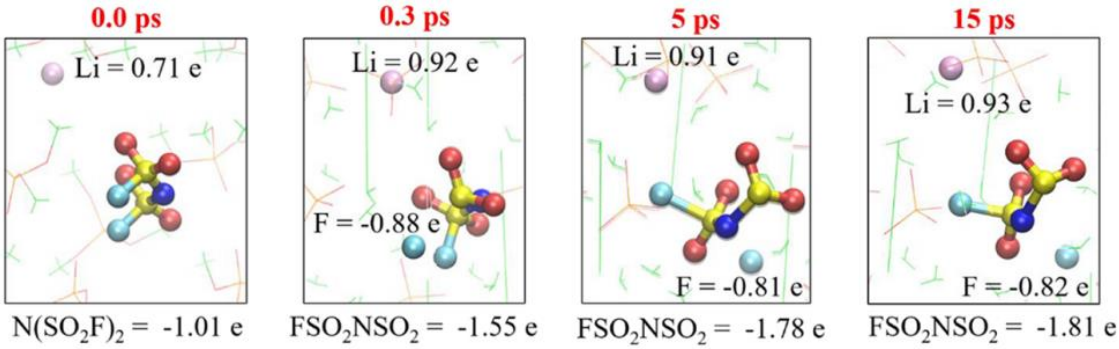

(c)

Figure 3.3 LiFSI reduction mechanism in a 1 M LiFSI/TMP solution: (a) Model I, (b) Model II, and (c) Model III. Li (violet), N (blue), C (green), P (orange), H (white), F (cyan), S (yellow), and O (red).

Bader charges are calculated on the FSI− counterion on every time step of the AIMD to gain additional insights into the reaction sequence. The Bader charge analysis is conducted in the four systems: electrolyte system in which there is no presence of Li-metal electrode, and Models I, II, and III, from the interfacial electrolyte−Li-metal electrode system in which there is a Li metal electrode next to the electrolyte. Figure 3.4 shows the net charge of the FSI^- counterion over the simulation time. Every time the charge of the FSI^- counterion abruptly changes is because a chemical reaction has taken place.

Lithium Reference Electrode−Electrolyte−Li Metal Electrode System. We study how the OCPE of the Li-metal electrode changes in the three interfacial models. The OCPE calculation is performed from the local potential profile. Figure 3.5a shows the local potential profile average along the z axis, which results from integrating the local potential throughout the xy planes at 0 and 15 ps. The xy planes are the planes parallel to the interface. Atomic positions are taken every 0.5 ps from the three models of the

interfacial systems. A pure pristine Li-metal, LRE, is added next to the electrolyte completing the cell structure: LRE/electrolyte/Li-metal. Then, the local potential profile is calculated from this full cell. The OCPE is calculated as the difference between the average local potential profile along the Li-metal region and the LRE region.

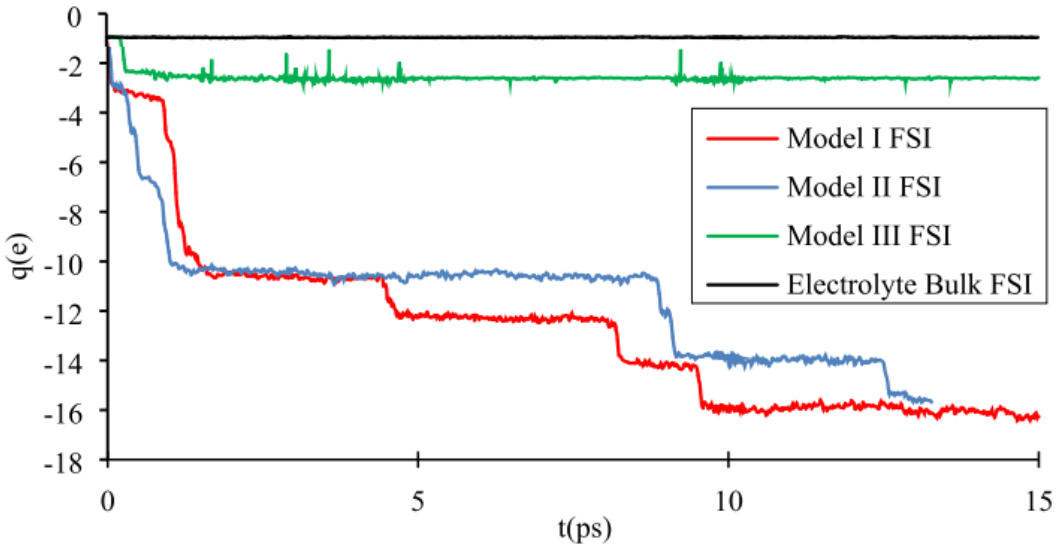

Figure 3.4 Bader charges of ion-pair LiFSI in Model I: undissociated ion pair in contact with the Li-metal electrode, Model II: dissociated ion pair in contact with the Li-metal electrode, Model III: dissociated ion pair avoiding contact with the Li-metal electrode, and electrolyte bulk: there is no Li-metal electrode, only the electrolyte.

For Model I, at 0 ps, the LRE region goes from 0 to 10 Å along the longitudinal axis, corresponding to the location of the LRE. Similarly, the Li-metal region goes from 26 to 37 Å along the longitudinal axis. As the simulation progresses, the LRE and Limetal regions are constantly changing. For Model I, at 15 ps, when the SEI is completely formed, the Li-metal region goes from 24 to 37 Å. The increase in the Li-metal region is due to the SEI formation. We repeat the OCPE calculation every 0.5 ps from 0 to 15 ps for the three models studied in the interfacial systems. When there is no SEI formed, the Li-metal

region goes from the minimum z-coordinate of a Li-metal atom to the maximum z-coordinate of a Li-metal atom. During the decomposition of the FSI−, the Li-metal region goes from the minimum z-coordinate of any Li-atom bonded to FSI− that is attached to the Li-metal to the maximum z-coordinate of a Limetal atom. We consider an atom bonded to Li based on a threshold distance for the atom pair: 2.3 Å for Li−O, 2.0 Å for Li−F, 2.0 Å for Li−N, and 2.5 Å for Li−S. Figure 3.5b shows the OCPE behavior over time for the three models. When no SEI is formed, as observed in Model III, the average OCPE of the Li-metal electrode over time is +0.36 eV vs LRE. The average OCPE of the Li-metal electrode changes when an SEI is formed. Due to the formation of an SEI, the average OCPE of the Li-metal electrode over time is −0.07 and −0.21 eV vs LRE for Models I and II, respectively. The formation of the SEI decreases the average OCPE of the initial Li-metal electrode by ∼0.42 eV vs LRE. The difference between Models I and II is perhaps due to the different SEI formation.

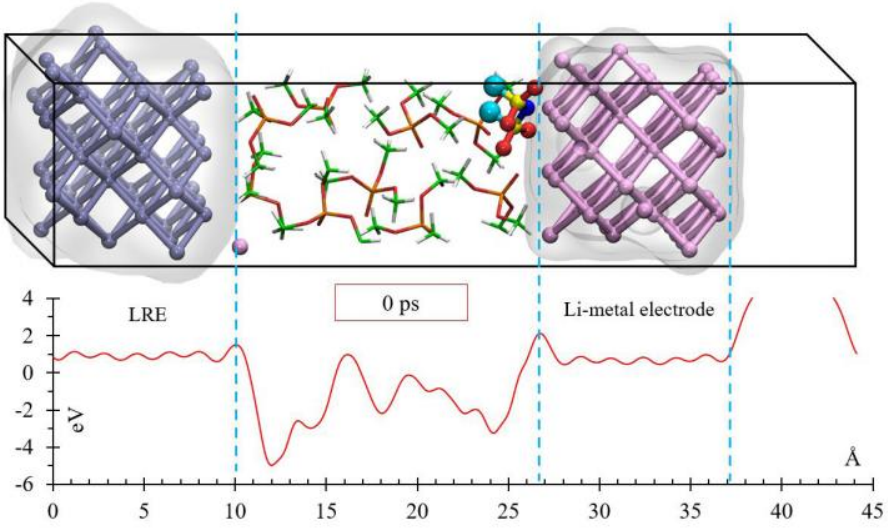

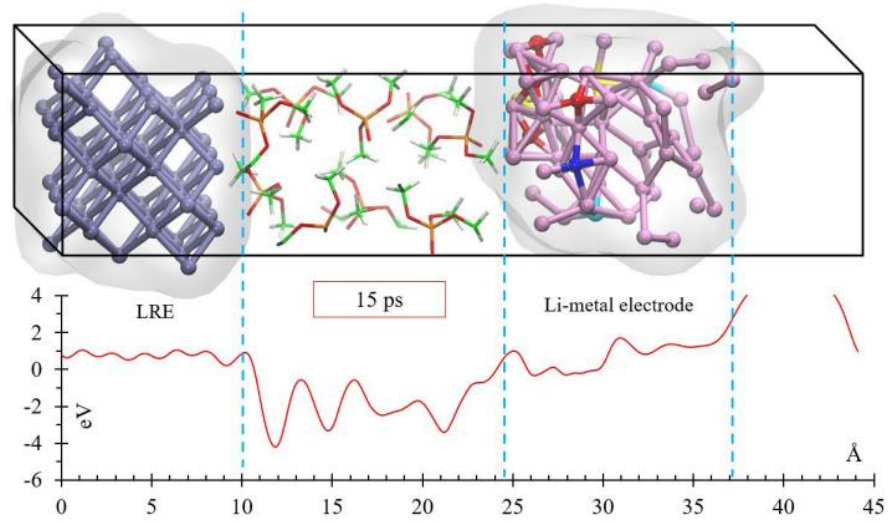

(a)

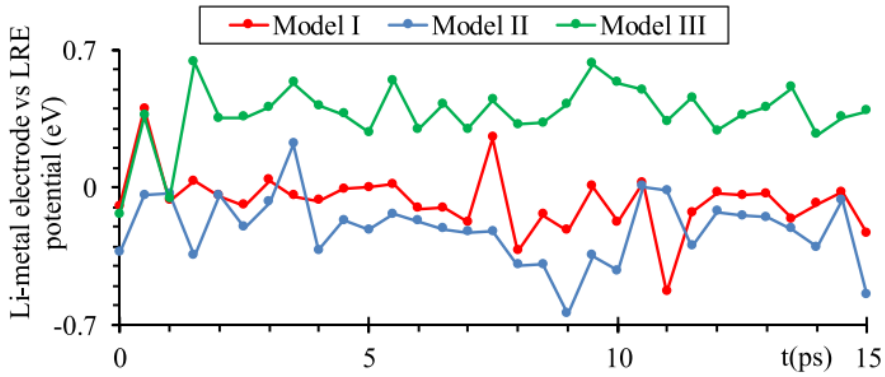

(b)

Figure 3.5 (a) Potential energy profile along the longitudinal axis at 0 and 15 ps when an SEI is formed. (b) Li-metal electrode vs LRE potential during the SEI formation for the three interfacial models.

3.5. Conclusions

We performed AIMD simulations and DFT calculations on three scenarios. Electrolyte: both, AIMD and DFT, predict that Li^+ ions are tetrahedrally coordinated to the solvent and salt molecules. However, Li^+ ions can also be found coordinated with three

or less molecules, but this is a transition state and only occurs while the Li^+ ion is traveling from one cage to another in the electrolyte. The inner shell of a solvated Li^+ ion is composed of four TMP molecules. O atoms that are not bonded to a methyl group from the TMP are the corners of a tetrahedron with the Li^+ ion located at the center. The counterion, FSI^-, can enter the inner shell of Li^+ ions solvated by TMP molecules changing the configuration of the inner shell to three TMP and one FSI^-. O atoms that are not bonded to a methyl group from the TMP and one O bonded to S from the FSI^- are the corners of a tetrahedron with the Li^+ ion located at the center. The characteristic features of the pair distribution function calculated in the AIMD simulations were also observed in the electronic structure calculations. The activation barrier that Li+ ions need to overcome to move freely along the electrolyte is 4 eV, in which the most stable structure is the Li^+ tetrahedrally coordinated with three TMP and one FSI^-, and the least stable structure is the Li^+ coordinated with four or less TMP.

We identified the decomposition pathway of LiFSI salt and the species present in the formed SEI between the electrolyte and the Li-metal electrode in the interfacial electrolyte−Li-metal electrode. Our data suggests that the following steps occur in the breakdown of the salt LiFSI: The counterion FSI^- rapidly loses one F ion to the lithium surface, resulting in the formation of LiF^- species. The remaining $FSO_2NSO_2^{-2}$ decomposed into SO_2^{-2} and $NFSO_2^{-2}$. The SO_2^{-2} deposited onto the Li surface. The SO_2^{-2} reacts with the Li-metal electrode forming Li_2O and Li_2S. The remaining $NFSO_2^{-2}$ defluorinate losing its F ion to the lithium surface, resulting in the formation of LiF. The NSO_2^{-1} deposited over the lithium surface decomposes in the following picoseconds

forming binary compounds Li_3N, Li_2S, and Li_2O. In contrast, when the salt is solvated by the TMP molecules avoiding a direct contact with the Li-metal electrode, only one defluorination occurs decomposing the FSI^- into $FSO_2NSO_2^{-2}$ and a F^-. The two ions remain stable as they are solvated by the TMP molecules. Therefore, salt fragmentation will necessarily take place when the counterion is in contact with the Li-metal electrode. We expect to get the same results independently of plane orientation. The reaction sequence could change, but the final composition of the SEI will be the same. This is supported in part by the fact that Models I and II reached the same SEI composition regardless of the initial position of the salt; however, the plane orientation could change the reaction pathway, making the reactions to occur in a different order, as observed in the cases of Models I and II.

Finally, in the lithium reference electrode−electrolyte− Li-metal electrode, the formation of the SEI as a result of side reactions occurring at the interface electrolyte/Li-metal electrode causes a drop in the OCPE of the Li-metal electrode by ∼0.42 eV. The drop in the OCPE can have a measurable effect on the open-circuit potential of a battery using Li-metal as anode and a 1 M TMP/LiFSI electrolyte. The nominal opencircuit potential in a Li-ion battery, 3.6 eV, would decrease up to 3.18 eV only due to the formation of the SEI, before any charge/ discharge cycles. However, to calculate the overall battery potential before the start of the charge/discharge cycles, it is necessary to calculate also the OCPE of the cathode and how it behaves in contact with the 1 M TMP/LiFSI electrolyte.

4. CHAPTER IV LI-METAL ANODE IN DILUTE ELECTROLYTE LIFSI/TMP: SEI EVOLUTION DURING CYCLING USING AB INITIO MOLECULAR DYNAMICS

4.1. Synopsis

An interfacial study is performed using ab initio molecular dynamics simulations to elucidate the solid electrolyte interphase (SEI) evolution formed between an electrolyte based on trimethyl phosphates (TMP) and lithium bis(fluorosulfonyl)imide(Li^+FSI^-) salt in contact with a Li-metal electrode. Going beyond the initial SEI composition generated due to the degradation of one counter-ion adding a second and third counter-ions ana analysis of how the initial SEI evolution is performed. The results indicate a different product formation due to the LiFSI salt dissociation as the SEI is formed. The products formed due to the dissociation of the 1st LiFSI salt when in direct contact with the Li-metal anode are Li_2O, Li_2S, Li_3N and LiF. These four Li-binary products compose the formed SEI. Then, a 2nd LiFSI is located at the electrolyte/SEI/Li-metal. The products formed due to the dissociation of the 2nd LiFSI when in contact with the SEI are Li_2S, Li_2O, LiF, Li_3NSO_2. Finally, a 3rd LiFSI is located at the electrolyte/SEI/Li-metal. The products formed due to the dissociation of the 3rd LiFSI when in contact with the SEI are $Li_2SO_2NSO_2$ and LiF. From the products composition due to the three LiFSI dissociations, we notice that the SEI prevents complete dissociation of the LiFSI as more counter-ions arrive to the interface.

---

*Reprinted with permission from:
Ab Initio Molecular Dynamics of Li-Metal Anode in a Phosphate-Based Electrolyte: Solid Electrolyte Interphase Evolution by D. E. Galvez-Aranda, J. M. Seminario, 2021. J. Electrochem. Soc. 168 090528

We also study the electrochemical window stability to identify the energy barriers the electron must overcome to be transferred from the anode to the counter-ion to initiate the LiFSI dissociation. We calculate the effect of the SEI formation in the anode potential, showing that the anode potential decreases from -0.39 V vs Li/Li^+ when there is not SEI, to 0.9 V vs Li/Li^+ when there is a SEI formed due to the dissociation of the three counter-ions. Finally, a simple scaling method is presented to scale our nano-scale results into a macro real battery. By performing this scaling method, we identify the number of counter-ions that need to be consumed to obtain a stable SEI in a CR2032 coin battery and also a linear extrapolation is performed to scale the SEI thickness as the counterions dissociates.

4.2. Introduction

Li metal batteries (LMBs) are being extensively study as an appealing new generation of energy storage devices because its high theoretical capacity, 3860 mAh g-1, and low redox potential, -3.04 V vs standard hydrogen electrode.[74-76] However, there are still several issues in the overall performance of Li-metal as anode material, such as poor electrochemical stability,[77] low cycling Coulombic efficiency[78] and Li dendrites growth.[4, 79]

The Li-metal interfacial stability with electrolytes affects the overall battery cycling performance.[80-82] Degradation of Li ion batteries occur due to the loss of active material, from the electrode or the electrolyte, consumed partly forming the solid electrolyte interface (SEI).[83-85] A SEI formation is desirable but only if it reaches an electrochemical stability after few cycles, without consuming to much active material and protecting both the electrolyte and the electrode. Similarly, in LMB, a poor cycle

performance is observed due to the irreversible formation of products consuming the active electrode material.[15, 86] The SEI formed due to the reaction occurring at the interface has measurable effects in the open-circuit potential.[69] Appropriate electrolyte solutions with high safety and interfacial compatibility with both electrodes, cathode and anode, are required to achieve batteries with higher electrochemical stability over cycling. Two strategies have been proposed to improve the electrochemical performance in LMB focused in the development of an stable Li metal/electrolyte interface over cycling:[87] 1) The addition of an artificial SEI at the Li-metal/electrolyte interface[87] and 2) The addition of liquid electrolyte additives that contain fluorine such as lithium bis(fluorosulfonyl)imide (LiFSI) to create a robust and stable SEI.[88-89] Phosphates, such as the trimethyl phosphate (TMP) have been used as additives for Li-ion batteries because its flame retarding feature and relatively high ionic conductivity.[35, 90-91] TMP has a wide liquid temperature window, -46 °C to 197 °C and it is able to dissolve lithium salts, even at high salt concentrations.[92-93] Besides the use of TMP as an additive in an electrolyte solution at small concentrations, less than 10 wt. %,[94] TMP can also be employed as pure electrolyte solvent.[95]

Recently, concentrated electrolyte such as 5 M LiFSI solvated in TMP effectively suppress the growth of Li dendrites because the formation of a LiF-rich SEI layer due to the decomposition of the LiFSI at the Li-metal interface.[43] Ab initio molecular dynamics simulations for Li^+ conducting electrolytes, based on TMP solvent and LiFSI salt, in contact with a Li-metal electrode, elucidating the initial SEI formation and composition due to the dissociation of a first FSI^- counterion found that the FSI fully dissociated in Li-

binary compounds in contact with Li-metal such as Li_2O, Li_2S, LiF and Li_3N;[50] however, this first counterion did not represent the final composition of the SEI during charge/discharge cycles, since additional counter ions arrive to the Li-metal/electrolyte interface during cycling, modifying the composition further the initial SEI.

An electrochemical stability window (ESW) analysis elucidates if a dissociation of the solvent and salts is possible in contact of an electrode. ESW is defined as the gap between the oxidation and reduction potentials.[96] If the anode has an electrochemical potential above the solvent and ion reduction potential, a reduction of the solvent of ion is possible.[97] For example, TMP decomposes at a potential of 1.2 V vs. Li/Li^+,[35, 98] meaning that the electrochemical potential of the Li anode is 1.2 V below the reduction potential of the TMP, therefore a reduction of the TMP is not possible, at least during open-circuit conditions. The potential is modified during charge conditions, overcoming the 1.2 V, making possible the decomposition of TMP in contact with Li metal anode. The formation or addition of a passivation layer such as SEI could prevent further electron transfer between electrode and electrolyte.[33, 99]

In the present work, we study the morphology SEI evolution during its growth beyond its initial structure. We follow a novel procedure that allows us to create an atomistic environment that can simulate a cycling behavior, focusing at the moments counterions dissociate at the interface without considering the long travel times it would require to the Li-ions and counterions to arrive to the interface. We also study the electrochemical window stability of all the electrolyte components, solvent, and ions, and the Li-metal anode. Finally, we present an intuitive scaling method to calculate

equivalences from atomistic nanoscale simulations to macroscopic batteries. A linear extrapolation is performed to estimate SEI thickness as the number of counterions dissociates.

4.3. Methodology

We perform ab initio molecular dynamics (AIMD) simulations of a phosphate-based electrolyte composed of 1 M LiFSI in TMP. We study an interfacial electrolyte−Li-metal electrode system, using a slab structure. The electrolyte box is 10.53 × 10.53 × 17.48 $Å^3$ containing one LiFSI and nine TMP, corresponding to a 1 M electrolyte. The Li-metal anode box is 10.53 × 10.53 × 10.53 $Å^3$. To study the morphology evolution of the SEI beyond its initial formation, we follow a novel procedure which consists in replacing the electrolyte box once the counterion is dissociated forming the SEI.

Three counter-ion dissociations are performed to study the SEI morphology evolution due to the decomposition of the ions. 1st Dissociation: the electrolyte box is assembled next to the Li-metal box, creating the interfacial electrolyte-electrode system. An AIMD is performed to the interfacial system for 15 ps. Reactions are expected during this time forming a SEI (Figure 4.1a). 2nd Dissociation: a new electrolyte box is assembled next to the SEI/Li-metal box formed in the 1st dissociation, creating the interfacial electrolyte-SEI-electrode system. An AIMD simulation is carry out to the interfacial system for 15 ps. Reactions are expected during this time, modifying the composition of the SEI (Figure 4.1b). 3rd Dissociation: A new electrolyte box is assembled next to the SEI/Li-metal box formed in the 2nd dissociation, creating a new interfacial electrolyte-

SEI-electrode system. An AIMD is performed to the interfacial system for 15 ps (Figure 4.1c). All the initial geometry boxes from each dissociation are showed in Figure 4.2.

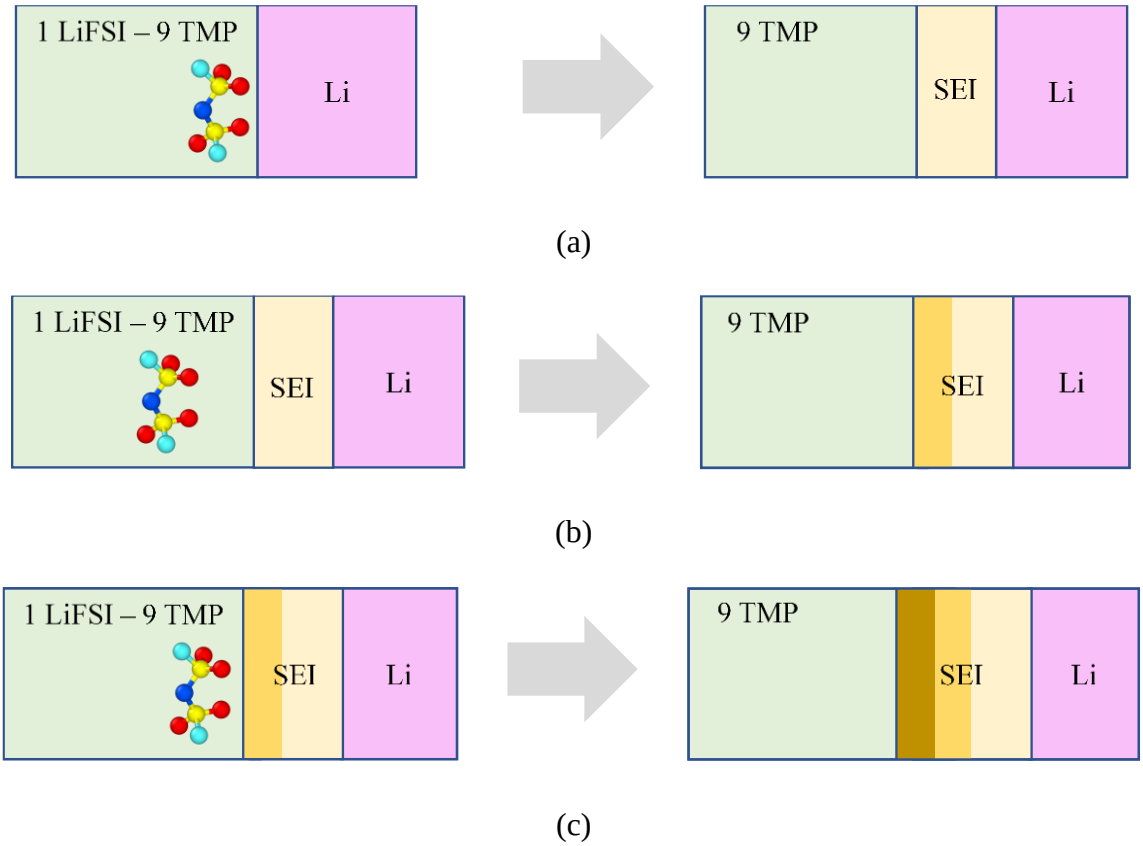

Figure 4.1 Procedure of SEI morphology evolution in a channel. (a) An electrolyte box with one LiFSI and nine TMP is assembled next to the Li-metal box. Then, an AIMD simulation is performed until a SEI is created between the anode and electrolyte. (b) The SEI and Li-metal anode from the previous run are assembled next to a new electrolyte box composed of one LiFSI and nine TMP. Then, an AIMD simulation is performed until the SEI changes its composition due to the 2nd FSI dissociation. (c) The new SEI and Li-metal anode from the previous run are assembled next to a new electrolyte box of one LiFSI and nine TMP. Then, an AIMD simulation is performed until the SEI changes its composition due to the 3rd FSI dissociation. Then, the final composition of the SEI is studied due to the dissociation of the three counter-ions.

The Li-metal and the electrolyte boxes are optimized separately using Born−Oppenheimer approximation[100] to solve the electronic Schrödinger equation using

density functional theory (DFT)[101] with the Perdew−Burke−Ernzerhof (PBE) functional.[55, 102] These calculations are performed using periodic boundary conditions (PBC) using a plane-wave energy cut-off of 40 Ry (λ = 0.5 Å) and 27 k-points were used for the k-mesh within the projector-augmented wave approach (PAW).[57] Due to the PBC, the interfacial system features a sandwich-like structure along the longitudinal direction. All the AIMD simulations of reactions at the interfacial site are performed for a maximum of 15 ps under the NVT ensemble at 297 K with a tolerance of ±20 K to rescale velocities and with a time step of τ = 1 fs. A Bader charge allocation method is used to study charge transfers.[58, 60, 103]

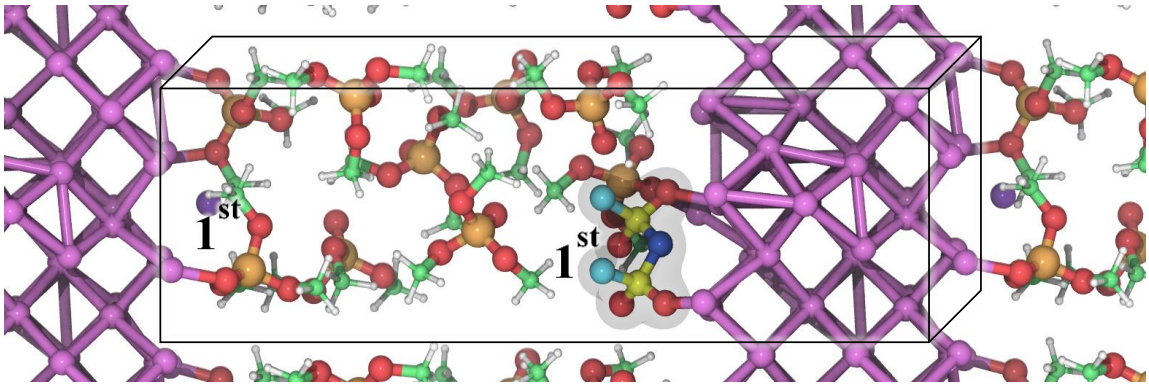

(a)

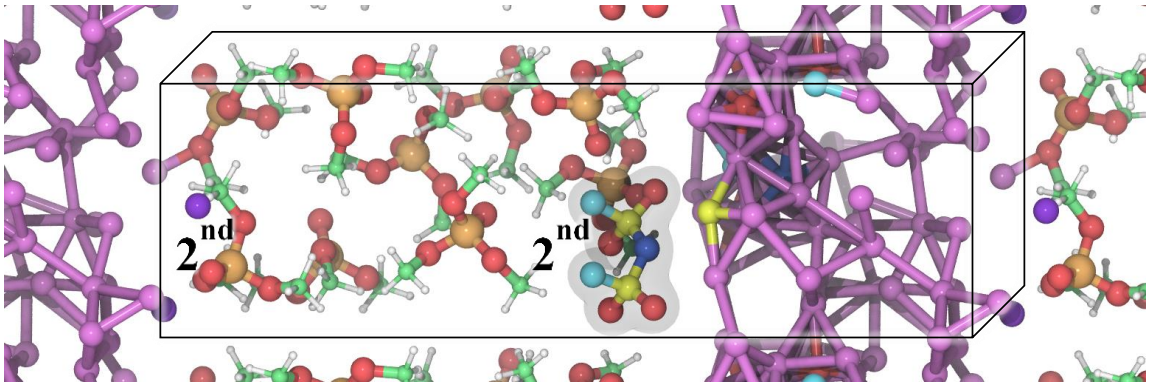

(b)

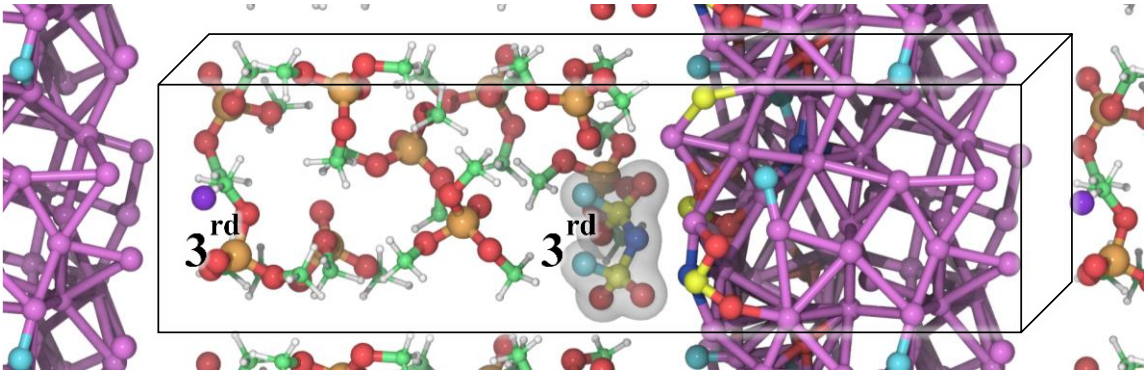

(c)

Figure 4.2 Initial boxes of $Li^{+}(F_2NO_4S_2)^{-}$ (LiFSI) salt, $(CH_3O)_3PO$ (TMP) electrolyte and Li metal electrode, corresponding to the dissociation of (a) first, (b) second, and (c) third counter ions. Counter ion (gray shadow). Li (violet), N (blue), C (green), P (orange), H (white), F (cyan), S (yellow) and O (red).

We calculate the battery potential with respect to a lithium reference electrode (LRE). The actual calculation by atomistic quantum mechanical first principles methods of the potential difference between cathode and anode plays a significant role in the design and selection of battery materials to improve performance. We focus on the creation and effects on the SEI due to such potentials. We also calculate the potential of an NMC cathode with respect to the LRE in order to get the full battery potential. Figure 4.3 shows an equivalence of the use of reference electrode in an experimental CR2032 coin cell battery[104] and our computational samples. We add an LRE every time we want to calculate the potential of the anode, that way the LRE does not participate in the reactions occurring in the electrolyte/Li-metal anode interface resembling an ideal LRE.[50]

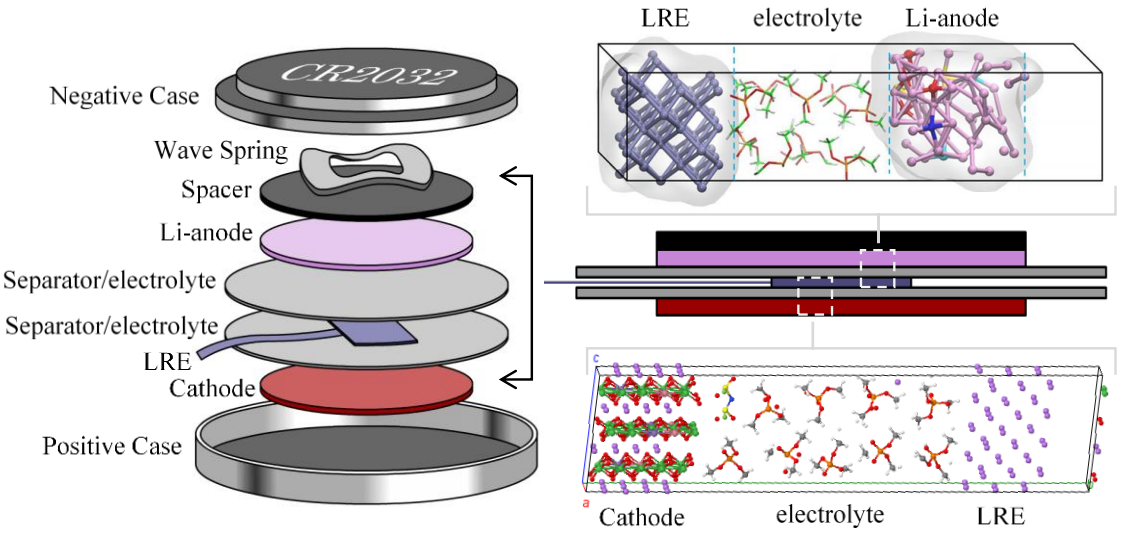

Figure 4.3 Schematic of the use of a LRE in a CR2032 experimental coin cell battery and their corresponding AIMD model to obtain the battery potential as the SEI is formed.

4.4. Results and Discussion

When a 1st FSI^- counterion is in direct contact with the Li-metal, the counterion reacts instantly creating an initial SEI. As a 2nd counterion is located at the electrode/electrolyte interface, the decomposition sequence of this 2nd counterion is not the same as the one observed for the 1st counterion due to the presence of the SEI, forming new products modifying the composition and morphology of the initial SEI. Similarly, as a 3rd counterion is located at the electrode/electrolyte interface, the degradation of the counterion is way less impacting than the one observed on the degradation of the 1st counterion.

1st Dissociation: Initial SEI composition due to degradation of the 1st FSI^- counter ion: The FSI^- counterion located at the interface electrolyte-electrode reacts instantly with the Li-metal anode. At the end of the 15 ps of simulation time the FSI^- has been completely

dissociated in contact with Li-metal forming several Li binary compounds, such as Li_2O, Li_2S, Li_3N, and LiF. The reaction pathway is elucidated through a Bader charge analysis, which are calculated at every time-step during the 15 ps of the AIMD simulations.

Initially the counterion has a total charge of -1.09e. The reaction sequence begins with the defluorination of the salt at 0.05 ps, leaving a FSO_2NSO_2 fragment with a total charge of -2.03e (Figure 4.4). The dissociated F^- reacts immediately with the Li-metal forming lithium fluoride. After the initial defluorination of the counterion at 0.34 ps, an SO_2 group comes off and lays on the Li-metal surface. The SO_2 fragment has a charge of -1.96e, and the remaining $NFSO_2$, a charge of -1.87e. Then, at 0.48 ps, a second defluorination occurs, leaving a NSO_2 fragment with a total charge of -2.71e. The dissociated F^- reacts immediately with the Li-metal forming lithium fluoride. At 0.96 ps, the SO_2 reacts with the Li-metal forming two Li binary compounds: Li_2O and Li_2S. After 1 ps, the SEI is formed by Li_2O, Li_2S, LiF and NSO_2 fragments, and does not change its composition until almost 8 ps later. At 8.89, the O from the NSO_2 goes into deeper layers of the Li-metal anode, breaking the S−O bond and forming Li_2O. The remaining NSO fragment has a charge of -1.92e. At 9.09 ps, the other O from the NSO reacts with the Li-metal, breaking the S−O bond and forming Li_2O. The remaining NS fragment has a charge of -2.86e. Finally, the NS bond breaks at 12.55 ps, forming the Li binary products: Li_2S and Li_3N. Thus, after 12.55 ps, the FSI has been completely dissociated and the SEI is composed of Li binary products: Li_3N, Li_2S, Li_2O and LiF. A detailed list of the reactions in sequence, time frame and electron transfer are given in Table 4.1.

Table 4.1 Reaction time and electron transfer reactions during FSI^- decomposition during the 1st dissociation

Reaction	Time (ps)
$N(SO_2F)_2^{1-} + 2e \rightarrow FSO_2NSO_2^{2-} + F^{1-}$	0.05
$FSO_2NSO_2^{2-} + 2e \rightarrow NFSO_2^{2-} + SO_2^{2-}$	0.34
$NFSO_2^{2-} + 2e \rightarrow NSO_2^{3-} + F^{1-}$	0.48
$SO_2^{2-} + 4e \rightarrow 2O^{2-} + S^{2-}$	0.96
$NSO_2^{3-} + 2e \rightarrow NSO^{3-} + O^{2-}$	8.89
$NSO^{3-} + 2e \rightarrow NS^{3-} + O^{2-}$	9.09
$NS^{3-} + 2e \rightarrow S^{2-} + N^{3-}$	12.55

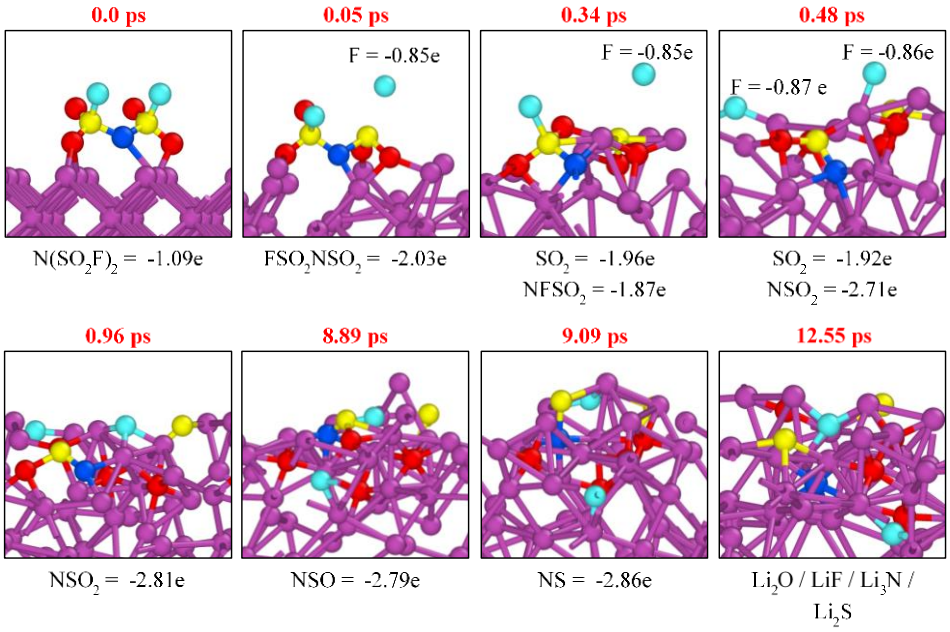

Figure 4.4 1st FSI reduction mechanism in a 1 M LiFSI/TMP solution. The TMP molecules have been removed to show a clear picture of the FSI reaction sequence. Li (violet), N (blue), F (cyan), S (yellow), and O (red).

2nd Dissociation: SEI composition due to degradation of the 2nd FSI^- counter ion:

The 2nd FSI^- counterion located at the interface electrolyte-SEI-electrode reacts with the SEI formed during the 1st FSI^- counterion. At the end of the 15 ps of simulation time the FSI^- has been dissociated forming several Li binary compounds, such as Li_2O and LiF, and a SO and NSO_2 fragments. The reaction pathway is elucidated through a Bader charge analysis. The Bader charges are calculated on every time-step of all the 15 ps of the AIMD simulation.

Initially the counterion has a total charge of -1e. The reaction sequence begins with the defluorination of the salt at 0.42 ps, leaving a FSO_2NSO_2 fragment with a total charge of -1.75e (Figure 4.5). The dissociated F^- reacts immediately with the SEI/Li-metal forming lithium fluoride. After the initial defluorination of the counterion, at 0.83 ps, the FSO_2NSO_2 is fragmented in a SO_2 and a $NFSO_2$ laying over the SEI/Li-metal surface. The SO_2 fragment has a charge of -1.86e, and the $NFSO_2$, a charge of -1.74e. Then, at 0.93 ps, a second defluorination occurs, leaving a $NFSO_2$ fragment with a total charge of -2.71e. The dissociated F^- reacts immediately with the SEI/Li-metal forming lithium fluoride. The remaining NSO_2 fragment has a charge of -2.71e. At 13.63 ps, the SO_2 reacts with the SEI/Li-metal forming SO and Li_2O. The SO fragment has a charge of -1.81e. At 14.35 ps, the remaining SO reacts with the SEI/Li-metal forming Li_2O and Li_2S, after that and until 15 ps, no more reactions are observed and the 2nd FSI dissociation have been dissociated adding some new products to the formed SEI: Li_2S, LiF, Li_2O and $NFSO_2^{2-}$. A detailed list of the reaction sequence, time frame and electron transfer are given in Table 4.2.

Table 4.2 Reaction time sequence and electron transfer of the FSI^- Decomposition during the 2nd dissociation

Reaction	Time (ps)
$N(SO_2F)_2^{1-} + 2e \rightarrow FSO_2NSO_2^{2-} + F^{1-}$	0.42
$FSO_2NSO_2^{2-} + 2e \rightarrow NFSO_2^{2-} + SO_2^{-2}$	0.83
$NFSO_2^{2-} + 2e \rightarrow NSO_2^{3-} + F^{1-}$	0.93
$SO_2^{2-} + 2e \rightarrow SO^{2-} + O_2^{2-}$	13.63
$SO^{2-} + 2e \rightarrow S^{2-} + O^{2-}$	14.35

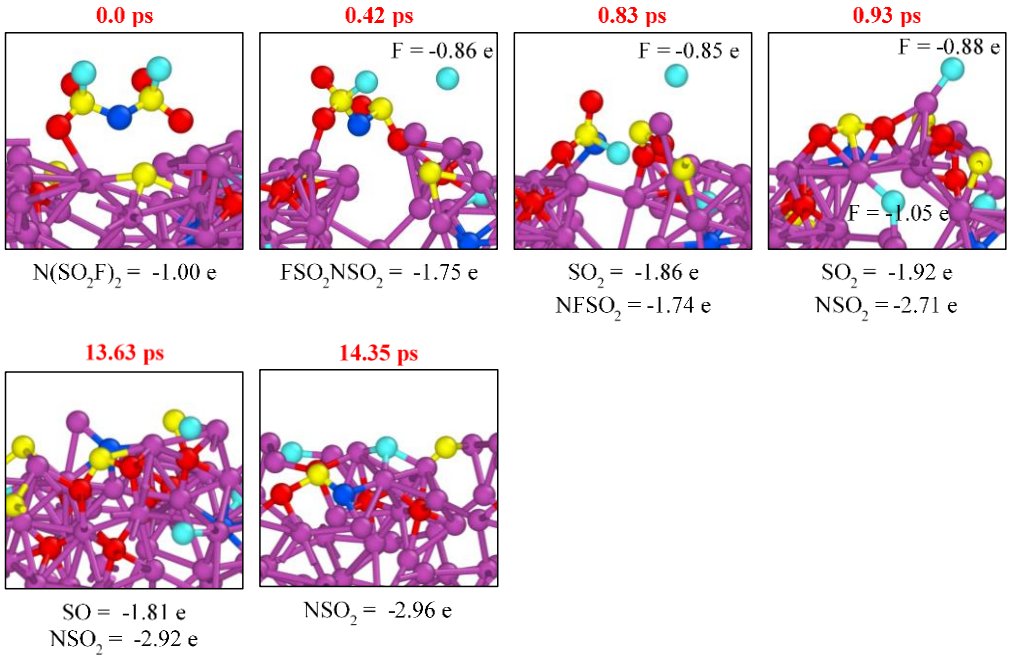

Figure 4.5 2nd FSI reduction mechanism in a 1 M LiFSI/TMP solution. The TMP molecules have been removed to show a clear picture of the FSI reaction sequence. Li (violet), N (blue), F (cyan), S (yellow), and O (red).

3rd Dissociation: SEI composition due to degradation of the 3rd FSI^- counter ion:

The FSI^- counterion located at the interface electrolyte-electrode reacts with the SEI formed due to the two previous dissociation. At the end of the 15 ps of simulation time the FSI^- has been dissociated in LiF and $SO_2NSO_2^{2-}$. The reaction pathway is elucidated through a Bader charge analysis, which are calculated at every time-step during the 15 ps of the AIMD simulations.

Initially the counterion has a total charge of -1.00e. Similarly, as in the previous two counter-ion dissociation, the reaction sequence begins with the defluorination of the salt at 0.20 ps. The remaining FSO_2NSO_2 fragment has a total charge of -1.82e (Figure 4.6). The dissociated F^- reacts with the Li-metal forming lithium fluoride. A second defluorination occurs at 0.87e, leaving a SO_2NSO_2 fragment with a charge of -1.82e. LiF is formed due to the reaction between the Li-metal and the dissociated F^-. No more reactions are observed until the end of the 15 ps of simulation time. Thus, after 0.87 ps, the FSI has been react with the SEI/Li-metal is forming: LiF and SO_2NSO_2. A detailed list of the reaction sequence, time frame and electron transfer are given in Table 4.3.

Table 4.3 Reaction Time Sequence and electron transfer of the FSI^- Decomposition during 3rd dissociation

Reaction	Time (ps)
$N(SO_2F)_2^{1-} + 2e \rightarrow FSO_2NSO_2^{2-} + F^{1-}$	0.20
$FSO_2NSO_2^{2-} + 1e \rightarrow SO_2NSO_2^{2-} + F^{1-}$	0.87

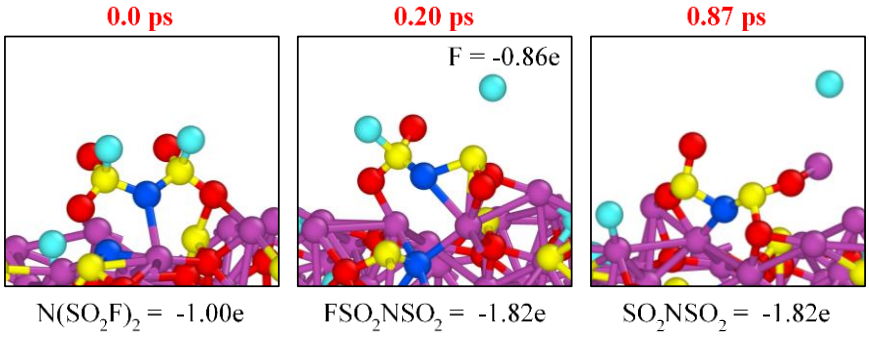

Figure 4.6 3rd FSI reduction mechanism in a 1 M LiFSI/TMP solution. The TMP molecules have been removed to show a clear picture of the FSI reaction sequence. Li (violet), N (blue), F (cyan), S (yellow), and O (red).

The composition of the SEI at the end of the 3rd dissociation is as follow: Li_3N, Li_2S, Li_2O and LiF due to the 1st FSI^- dissociation, Li_2S, LiF, Li_2O, $NFSO_2^{2-}$ due to the 2nd FSI^- dissociation, and LiF and SO_2NSO_2 due to the 3rd dissociation. Figure 4.7a shows the net charge of the each of the three FSI^- counter-ions over the 15 ps simulation time. Every time the charge of an FSI^- counter-ion changes is because a chemical reaction has occurred. All the reactions described in the previous section for the three counter-ions dissociation are charge-transfer reactions. We observe that 16e have been transferred to the counter-ion during the 1st dissociation, 10e during the 2nd dissociation, and 3e during the 3rd dissociation. It is clear then, that as the SEI is formed, it blocks further electrons transfer from the Li to the electrolyte (Figure 4.7b), preventing and reducing the electrolyte decomposition. In our model, the electron transfer is reduced from 16e, transferred when there was not SEI, to 3e, transferred when a SEI is formed.

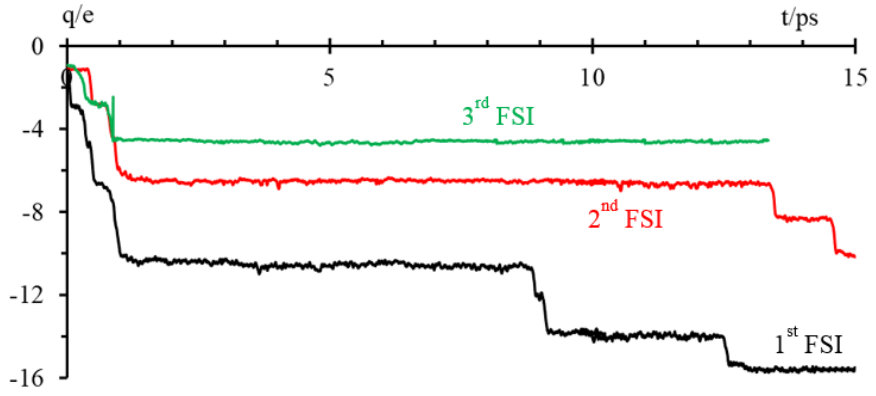

(a)

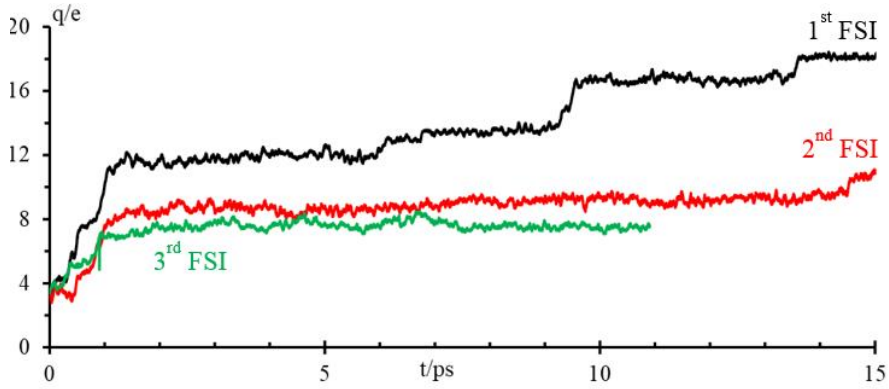

(b)

Figure 4.7 (a) Bader charges, q(t), of the three FSI- during its dissociation (b) Bader charges q(t) of the Li-metal electrode (Li_{54}) for each consecutive dissociation of counterions FSI^- at the Li-metal electrode.

We analyze the electrochemical stability windows of the electrolyte/Li-metal interface as the SEI is formed (Figure 4.8). In many battery reports,[25, 88, 105-106] the electrochemical stability was analyzed considered the highest occupied molecular orbital (HOMO) and lowest unoccupied molecular orbital (LUMO) of the electrolyte components to understand if their oxidation/reduction can occur. However, the HOMO-LUMO analysis is an approximation of the electronic structure, useful to investigate the electronic

properties of isolated molecules, but not in a solvent environment in which the energy levels of the isolated molecules do not indicate with precision which species are participating in redox reactions, expected in a anode/electrolyte interface.[97, 107] The true electrochemical stability window can be assessed from the ionization potential and electron affinity of the electrolyte components as showed by Peljo et al..[97]

The oxidation/reduction potential of the isolated molecules provide comparable data of energy barriers between each electrolyte component and Li-metal; however, these components are not isolated in the electrolyte, but surrounded by other solvents or ions. Therefore, we also calculated the oxidation/reduction potential of an electrolyte box containing 9 TMP, 1 Li^+ and 1 FSI^-. The reduction potential of this electrolyte bulk is located at -4.21 eV. Since the fermi energy of the Li-metal is located at -2.25 eV, electron transfer is highly possible from the Li-metal to the electrolyte. After the 3rd FSI^- dissociation, the SEI oxidation potential is -3.76 eV and the electrolyte bulk reduction potential is -4.21 eV, therefore, an electron transfer is still possible from the SEI to the electrolyte; however, the energy gap is reduced from 1.96 eV to 0.45 eV.

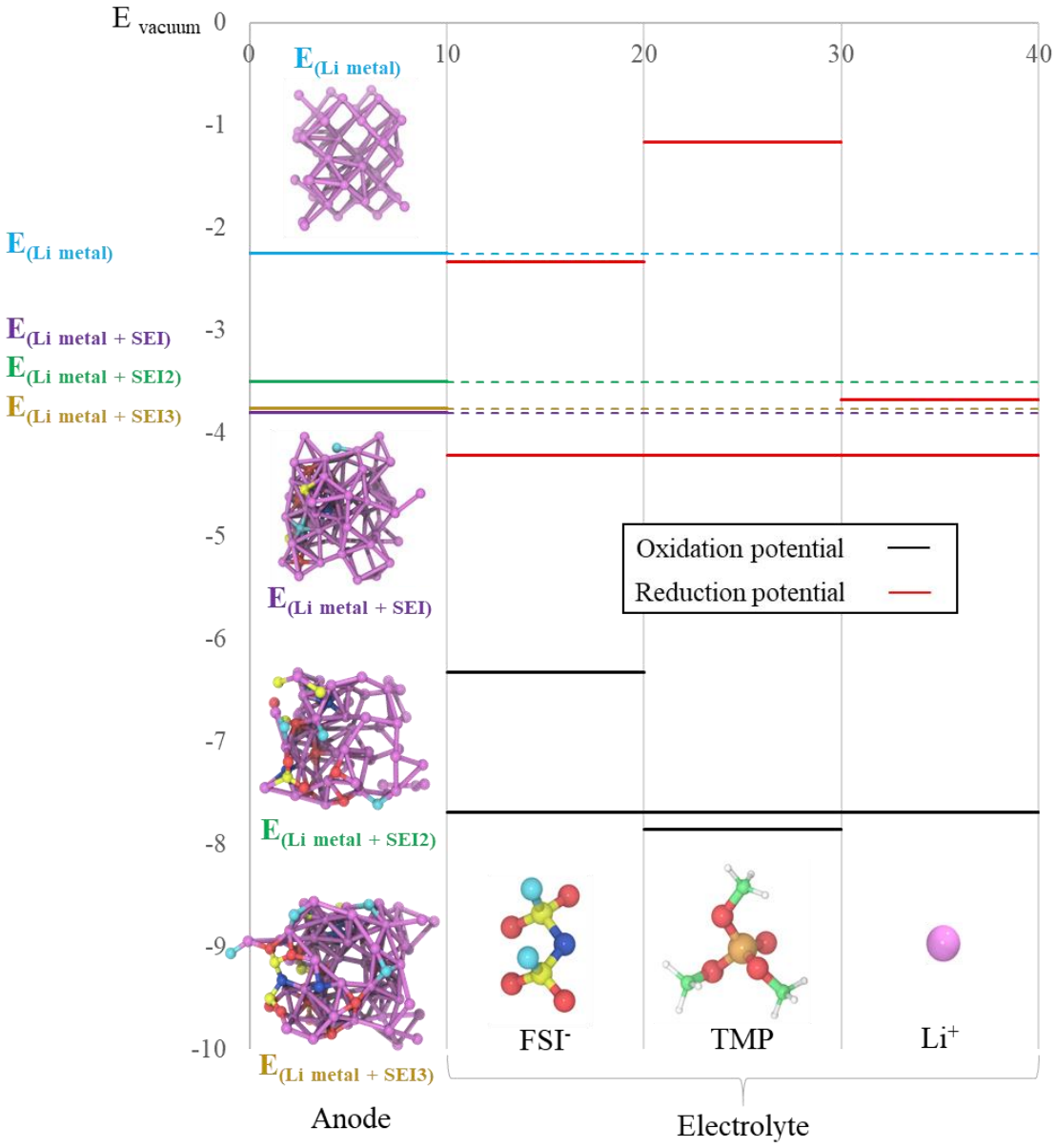

Figure 4.8 Electrochemical window of the LiFSI/TMP electrolyte and the Li-metal anode. Oxidation (black bars) and reduction (red bars) potential limits are showed for each electrolyte component individually (Li^+, FSI^- and TMP) and the electrolyte bulk. The fermi energy is calculated for the different stages of the Anode as the SEI is formed.

We propose a simple scaling rule to extrapolate AIMD predictions from a nanoBatt to a macroBatt. Data from the macroBatt is taken from Shi et al.[43] experiment, in which

they built a Li|$LiNi_{1/3}Co_{1/3}Mn_{1/3}O_2$ cell with a 5M LiFSI/TMP electrolyte by using a CR2032-type coin cell. The Li electrode was punched into discs (15.6 mm diameter and 450 µm thickness) to assembly the coin cell. The thickness of the separator is 30 µm, which is also a value typically reported in several commercial separators.[94, 108-110]

The scaling is used to extrapolate two parameters, the SEI time formation and the amount of LiFSI dissociated to form the SEI. One scaling factor is obtained as the ratio of the cross-section area of the nano-battery and the CR2032 coin battery (Figure 4.9). The second scaling factor is obtained as the ratio within the simulation time of the nano-battery and the real charging/discharging time of the CR2032 coin battery.

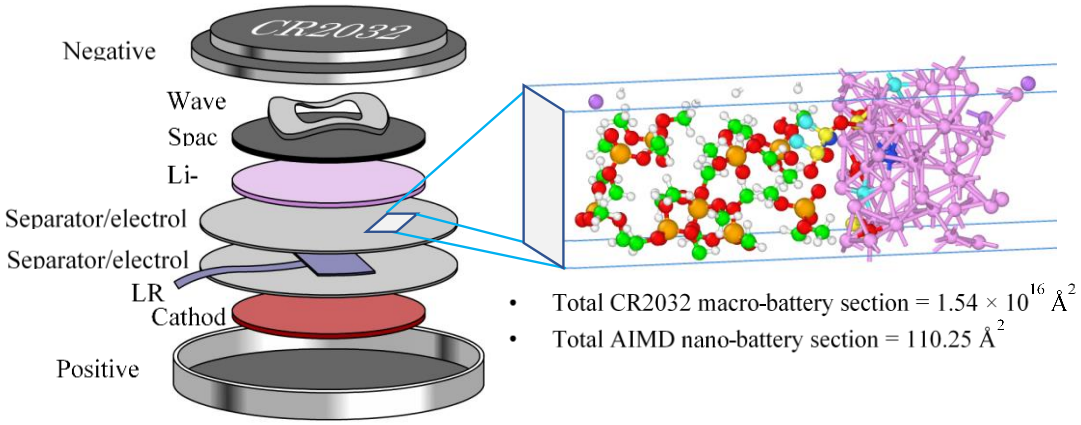

Figure 4.9 Scaling method based on the cross-section area between the AIMD nanoBatt and the CR2032 macroBatt.

In Table 4.4, we compare the dimension of the cross-section area, electrolyte volume and number of counter-ions between the CR2032 battery and our AIMD simulated battery (nanoBatt). An estimate of the total amount of FSI^- available in the CR2032 electrolyte is obtained from the volume of the separator: $\pi \times (8\ mm)^2 \times 30\ \mu m = 6.031\ mm^3$, with a 45% porosity,[111] the net electrolyte volume is 2.71 mm^3. From a previous study,[91]

the density of counter-ions is $3.30\times10^{18}/mm^3$ for a 5M LiFSI/TMP electrolyte, which is the one used in Shi et al. experiment.

Table 4.4 CR2032 macroBatt and nanoBatt main characteristics.

	CR2032 macroBatt	nanoBatt
Cross-section area	2.01×10^{16} Å^2	110.25 Å^2
Separator volume (45% porosity)	6.031 mm^3	
Electrolyte volume	2.71 mm^3	1653 Å^3
Counter ion density	$3.30\times10^{18}/mm^3$	6.04×10^{-4}/Å^3
Number of counter ions	8.95×10^{18}	1

A scaling factor based on the ratio of the cross-section area of the CR2032 battery and the cross-section area of the nanoBatt yields 1.82×10^{14} or the equivalent amount of dissociated FSI^- in the CR2032 per dissociated FSI^- in the nanobattery, i.e., 5.46×10^{14}, representing 0.0061% of the total FSI^- available in the macro electrolyte. The small factor indicates that the degradation occurring it is not yet significant in terms of number of ions reduction to form a SEI. Most of the ion's dissociation occur in the first charge/discharge cycles, as reported by Shi et al.[43] experiment, in which a drop of the capacity from ~140 $mAhg^{-1}$ to ~120 $mAhg^{-1}$ was observed during the first 3 cycles, a 14% drop. In the following cycles the capacity decreased at much lower rates reaching ~110 $mAhg^{-1}$ by the end of the 100th cycle. The observed capacity fade can be associated to the reduction of charge carriers to form the SEI, among other reactions occurring at the cathode/electrolyte or cluster formation in the electrolyte. For the scaling method used in the present work,

we consider that all the 14% of reduced charge carriers occurs at the electrolyte/Li-metal interface forming the SEI. Considering that the drop of 14% is associated completely to the dissociation of charge carriers to form the SEI, we obtain that 1.25×10^{18} counter ions are dissociated, which is 2295 times greater than the amount of dissociated counterions scaled from the nanoBatt, 5.46×10^{14}. Therefore, to scale the counterion degradation from the dissociation of the three FSI^- at the electrolyte/Li-metal interface, it is required to have 6885 FSI^- dissociated in a cross-section equivalent to the one from the nanoBatt. However, the 14% drop considers the loss of charge carriers, ions or counter ions. For a fully dissociation of an FSI forming Li-binary compounds such as Li_2S, Li_2O, LiF and Li_3N, 17 Li are consumed. Therefore, to calculate the number of ions and counter-ions consumed from scaling the data of our AIMD simulation we multiply the amount of FSI dissociated, 5.46×10^{14}, by 18 obtaining 9.84×10^{14} which represent 0.11% of the total amount of ions available.

We can also extrapolate the thickness of the SEI, based on the dissociation of the three FSI^- from the nanoBatt. The thickness of the SEI during the dissociation of the 1st, 2nd, and 3rd FSI^- is 3.3 Å, 3.8 Å and 4.4 Å, respectively. Performing a linear extrapolation, for the SEI thickness (d_{SEI}) yields, $d_{SEI}[Å] = 0.55\times n_{FSI} + 2.73$. Therefore, for a $n_{FSI} = 6885$, we get a thickness of 378 nm. From the literature, the average SEI thickness is in the order of 20 nm.[112-113] Thus, the extrapolated SEI thickness is one order of magnitude greater than the average SEI thickness. This is because we considered that all the reduced charge carriers are the dissociated counterions at the electrolyte/Li-metal interface; however, charge carrier reductions can also occur at the cathode/electrolyte interface,[114-115] forming

ionic clusters in the electrolyte.[116] Using the linear extrapolation, $d_{SEI}[Å] = 0.55 \times n_{FSI} + 2.73$, for a 20 nm SEI thickness, 359 FSI^- must dissociate in the nanoBatt cross-section. Thus, the equivalent amount of dissociated FSI^- in the CR2032 per dissociated FSI^- in the nanoBatt, yields 6.53×10^{16}, which is calculated multiplying the cross-section batteries ratio, 1.82×10^{14}, by the number of dissociated FSI^-, 359. 6.53×10^{16} is 0.72% of the total FSI^- available in the macro-electrolyte. Compared with the 14% drop from the reduced charge carriers, less than 1% correspond to the dissociation of the counter-ions.

4.5. Conclusions

We performed AIMD simulations to study the SEI initial formation and evolution as more counter-ions approaches the interface electrolyte/Li-metal. As the SEI is formed, the decomposition pathway followed by the FSI^- counterions changes producing a variety of products.

A 1st FSI^- fully dissociates in contact with the Li-metal anode, forming Li binary components such as Li_2O, LiF, Li_2S and Li_3N. Thus, the initial SEI interface composition includes the four Li binary components formed due to the degradation of this 1st FSI^-. Then, when a 2nd FSI^- approaches the interface, facing now the previous formed SEI, the species formed are LiF, Li_2S, Li_2O and Li_3NSO_2. Thus, the full SEI composition includes LiF, Li_2S, Li_2O, Li_3N and Li_3NSO_2 species formed due to the degradation of the first two FSI^-. When a third FSI approaches the interface electrolyte/SEI, the products formed are LiF and Li_2SO_2NSO2. Thus, the SEI composition includes LiF, Li_2S, Li_2O, Li_3N, Li_3NSO_2 and $Li_2SO_2NSO_2$ species. As the SEI is being formed, it has an impact decreasing the degradation of the upcoming FSI^-, clearly indicating the protective behavior of the SEI to

decrease further reaction of the counter-ions. As the dissociation reactions of the FSI^- occur, the formation of Li-binary compounds indicates the loss of these Li as charge carriers and are now part of the stable SEI, having an impact in the overall battery capacity. For the dissociation of one FSI^-, 17 Li are being consumed to form the Li-binary compounds forming the SEI. Therefore, high LiFSI concentrated electrolytes will perform better in terms of cyclability than low concentrated, since the loss of charge carriers will be less.

Performing a Bader charge analysis, all the reactions are occurring due to electron transfers from the Li-metal to the counter-ions. For the dissociation of the 1^{st} FSI^-, 2^{nd} FSI^- and 3^{rd} FSI^-, 16e, 10e and 3e, respectively, transferred from the Li-metal, indicating that as the SEI is formed, less electrons are able to be transferred from the electrode to the electrolyte. We calculated the energy barriers between the electrolyte components and the electrode as the SEI is formed. Initially the Fermi energy of the pure Li-metal is located at -2.25 eV. As observed in the AIMD simulation, the TMP does not dissociate because it has a reduction potential located at -1.16 eV, resulting in a barrier of 1.09 eV. FSI^- and Li^+ have reduction potentials equals to -2.33 eV and -3.67 eV respectively, both located below the Fermi energy of the Li-metal electrode, allowing the transference of electrons from the Li-metal. As the SEI is formed, its oxidation potential is located at -3.76 eV, below the reduction potential of the FSI^-, presenting an energy barrier of 1.43 eV. However, from the AIMD, we also observed electron transfer even when the SEI is formed. The difference with the electrochemical window analysis is that we are considering the oxidation/reduction potential of isolated electrolyte molecules. However,

these molecules are not isolated in the electrolyte, but surrounded by other solvent molecules or ions. The calculated reduction potential of a bulk electrolyte is located at -4.21 eV, which is below the oxidation potential of the formed SEI located at -3.76 eV, indicating that electron transfer from the SEI to the electrolyte is possible going accordingly with the results of the AIMD simulations.

Even though we have not observed any reaction of the TMP solvent molecule in contact with Li-metal because its energy barrier of 1.09 eV with respect to the Li-metal, we have to consider that this analysis is performed under open circuit condition. However, during charging conditions, in which a greater potential usually in the range of 5 eV is provide to the battery, which is 1.5 eV greater than the open circuit potential, the electrons from the Li-metal could receive the required energy to overcome the 1.09 eV barrier dissociating the TMP molecules. Also, because the formation of the SEI, the anode local potential increases from -0.39 V up to 0.91 V, indicating an increase in the anode local potential of about 1.3 V. Assuming that the potential at the cathode remains constant, an increase in the anode potential cause a decrease in the overall battery potential, decreasing the power that the battery can provide. An interfacial study between the cathode and the electrolyte it is necessary to calculate the actual behavior of the potential in a full battery.Lastly a simple scaling method is presented to establish a correlation between the results of our AIMD simulation and an experimental CR2032 battery, to provide an approximate number of FSI^- dissociated to form a stable SEI in the experimental CR2032 battery from the data obtained in the AIMD simulation. The 3 dissociated FSI^- from our AIMD simulation are equivalent to 6.53×10^{16} dissociated FSI^- in the experimental

CR2032 battery, which represent only the 0.72% of the FSI- existing in the 5 M TMP/LiFSI electrolyte of the CR2032 battery. Since a 14% drop from the reduced charge carriers is observed in the CR2032 battery, most of the reduced charge carriers are Li-ions forming the SEI and also as dead Li in the electrolyte and only less than 1% correspond to the dissociation of the counter-ions. The fast dissociation of FSI in contact with Li-metal, forming a stable SEI as proven from our AIMD, avoids further dissociation of upcoming FSI but still Li-ions can be reduced and captured in the SEI, being lost as charge carriers decreasing the overall capacity of the battery.

5. CHAPTER IV: LI-METAL ANODE IN DILUTE ELECTROLYTE LIFSI/TMP: A MACHINE LEARNING REACTIVE FORCE FIELD.

5.1. Synopsis

Molecular dynamics (MD) simulations employing classical force fields approximate the potential energy surface due to electronic structure and internuclear interactions as a function of the position of the nuclei. A typical classical force field approach works very well under the following conditions: there is no bond breaking or forming and electrons are highly localized in the nuclei. However, the predictive power of these simulations is only as good as the underlying interatomic potential.

Force fields often fail to faithfully capture key quantum effects in molecules and materials. Here we enable the direct construction of reactive molecular force fields from high-level ab initio calculations by incorporating atomic descriptors such as Bader charges, spatial configurations, bonds and angles formation, in order to replicate reactions in a MD simulation developing an alternative approach using machine learning techniques such as clustering, classifiers, and neural networks to construct dynamic force fields keeping the accuracy of high-level ab initio calculations. A dynamic force field is able to change its parameters depending on the atomic environment in which the atoms are located.

5.2. Introduction

Remarkable advances have been made by MD simulations offering unprecedented insights into complex electrochemical systems such as Li-ion batteries.[4, 117-118] However, one of the widely recognized issues in MD simulations is the lack of accuracy of underlying classical interatomic potentials, which hinders truly predictive modeling of dynamics and function of electrochemical systems.

A force field treats the atoms of a material as mathematical points each with lump parameters such as charge and mass in most cases as well as interatomic interactions, mainly two body but also with three, four, and many-body interactions, described by very simple to very sophisticated mathematical functions. For example, in the simplest cases, harmonic potentials can describe bonded interactions given a force constant between atom-pair and non-bonded interactions, such as van der Walls, can be treated by Lennard-Jones potentials. One possible solution to the accuracy problem is provided by direct ab initio molecular dynamics (AIMD) simulations, where the quantum-mechanical forces are computed on the fly for atomic configurations (environments) at every time step from which interpolations and extrapolations can be more precise than using a force field of constant parameters as AIMD simulations can only reach the order of 10-100 picoseconds for a system containing ~200 atoms with the modern computational resources that we have nowadays. To counteract the dimension and time-scale issues involved in the AIMD simulation several possible solutions have been proposed such as fitting analytical expressions to the potential energy surface (PES) learned from quantum mechanical

calculations.[119-121] Machine learning techniques have been proposed as a solution to solve the force field problem of classical molecular dynamics (CMD).

To solve the accuracy and molecular size dilemma, we develop an alternative approach using machine learning techniques such as clustering, classifiers, and neural networks to construct dynamic force fields keeping the accuracy of high-level ab initio calculations. A dynamic force field is able to change its parameters depending on the atomic environment in which the atoms are located. Atomic local environment (ALE) have been used before in the development of potentials to use in molecular dynamic simulations because atomic energy contribution depends strongly on the local chemical environment,[122] for example, bond-order potentials such as ReaxFF, reaches size-extensibility by using the local chemical environment concept.[123]

5.3. Methodology

ALE for each atom in the cell is collected at a fixed number of time-steps (n). All the collected data is stored in an ALE data matrix. When n = 1, we collect data every time-step of the ab initio simulation; however, even though collecting data at every AIMD time-step increases accuracy of the developed force field, the computational cost increases. ALE data matrix is analyzed using a K-mean clustering ML algorithm defining a fixed number (N_o) of atomic types.

For each atomic type, a set of force field parameters are defined from DFT calculations of the local environments. To describe the molecules more accurately, we have established that all atom pairs have nonbonded interactions, adding local perturbations such as bond, angle, and torsion. Force field parameters describe both,

bonded and non-bonded interactions, and are not constant, instead force field parameters are changing as the CMD simulation progresses, being able to replicate phenomena, such as chemical reactions and electron transfers, resembling the way as an ab-initio calculation does.

Force field parameters, involving bonded interactions, such as force, angle and torsion constants, as well as non-bonded interactions, such as well-depth, distance of zero interaction, and atomic charges change dynamically as the MD simulation progresses based on the information collected from the local environments in the AIMD simulations in a time-lapse of 15 ps. Each atom involved in the ab initio simulation has a set of features given its ALE, such as type of atomic nearest neighbors, atomic charges, bond distances and masses (Figure 5.1).

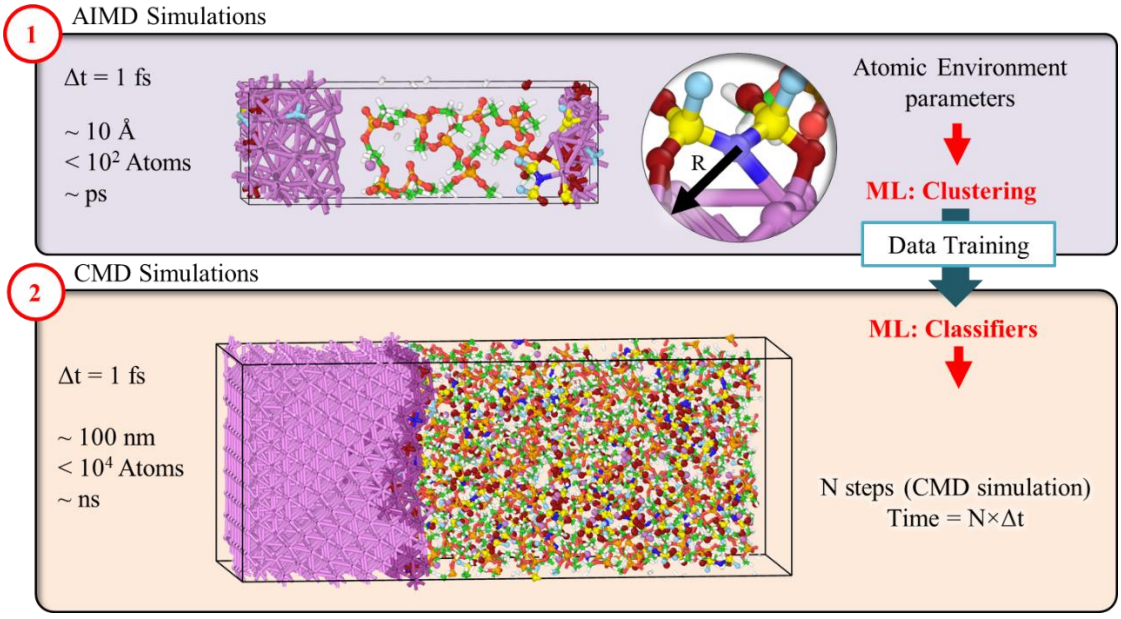

Figure 5.1 Schematics of the procedure followed in the development of a force field using a machine learning approach from ab initio calculations for a Li-metal/LiFSI-TMP interface.

To test the accuracy of the machine-learning time-dependent force fields, we develop a Li-metal/LiFSI-TMP nanobattery model to simulate SEI growth at two different salt concentrations, 1 M and 4M. The electrochemical system under test consists of two interfaced materials a Li-metal as anode and LiFSI/TMP as electrolyte. The two reactant materials and the product compound are modeled individually. We use all the data coming from four AIMD simulations studied in Chapter III and Chapter IV. The interfacial cell contains a slab geometry of the LiFSI/TMP electrolyte and Li metal and provide the ALE information of the respectives molecules at different environments and times during its dissociation at the metal-anode/electrolyte interface. (Figure 5.2).

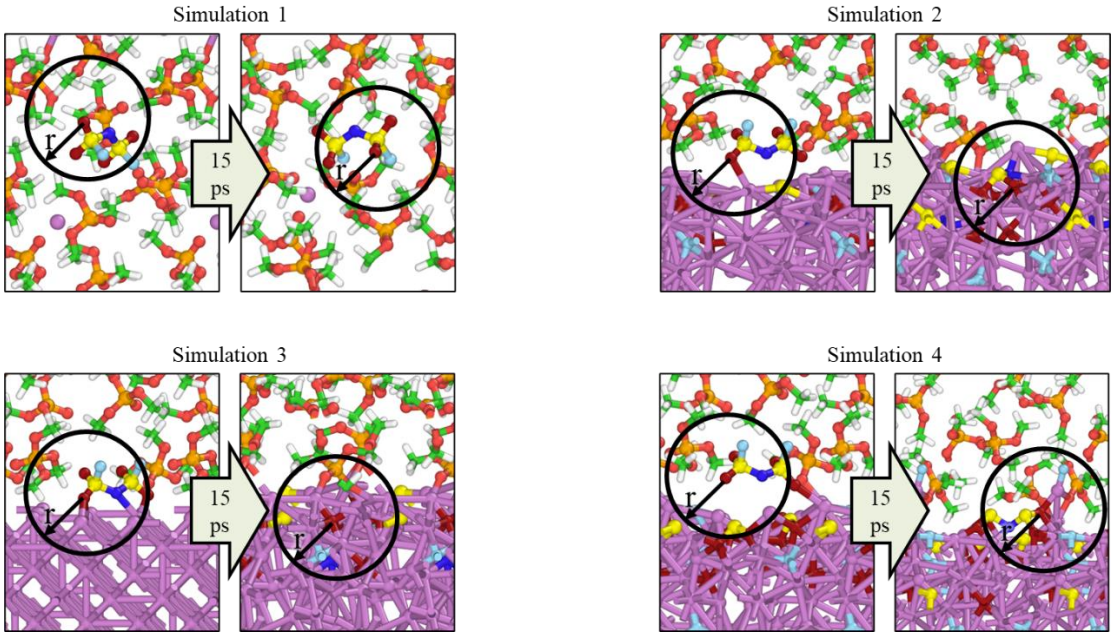

Figure 5.2 Four AIMD simulations are considered to get the ALE data to develop the MD simulation. Each simulation is used to study a particular environment, Simulation 1: pure electrolyte, Simulation 2: FSI dissociation over pure Li-metal, Simulation 3: FSI

dissociation after the dissociation of the 1st FSI and Simulation 4: FSI dissociation after the dissociation of the 2nd FSI.

Atomistic local environments the atomistic local environment is defined as a sphere of radius r_c, the cutoff radius, surrounding the position of an atom; therefore, we have an ALE for each atom from the AIMD simulation.

A set of features are defined for each ALE: atomic nearest neighbors, atomic charges, bond distances and mass of the central atom. Using ALE, we can group the atoms with similar features identifying different atom types. As a simplified illustrative example Figure 5.2 shows 8 different ALE for one of the O atoms from the FSI. We use a cutoff distance r_c of 6 Å to define the region of the ALE. From the 4 simulations showed in Figure 5.2, we collect the ALE data every 0.25 ps which is every 250 time-steps (n = 250). Therefore, since each AIMD simulation has taken 15 ps, for each simulation a total of 60 ALE are identified, having a total of 240 ALE per atom in total. Each ALE contains 12 features: charge of central atom, NN_O, NN_F, NN_S, NN_H, NN_C, NN_P, NN_{OFSI}, NN_N, $NN_{Li\text{-}ion}$, $NN_{Li\text{-}metal}$, mass of central atom. Being NN_x the number of x atoms in that particular ALE.

Data clustering The ALE data collected from the AIMD simulation is then clustered, based on the number of defined atomic types, N_o. The importance of the number of atomic types reflects the versatility of the force field being able to replicate all the reactions occurring in the AIMD. As we increase N_o, the accuracy of the calculation increases, but the computational cost of the simulation also increases. For that reason, it is important to define an N_o value that keeps a good accuracy comparable with the AIMD

results but keeping a reasonable computational cost. From the AIMD we observed that there are no reactions involving the TMP solvent molecule, therefore we focused our development on the FSI counter-ion which is the one that reacts in contact with Li-metal. Since the ALE data is a 12 dimensions matrix, we use a projection technique to decrease its dimensionality to 2 just for visualization purposes. All the calculations are performed over the original 12-D ALE data matrix. Plotting the 2D projected ALE raw data from the counter-ions atoms, F-S-O-N, (Figure 5.3a) we cannot distinguish how this bunch of data should be divided to define a fixed number of atom types (N_o). Coloring the 2D projected ALE raw data considering their original atomic type, we observe how the data is distributed. To perform in a more accurate way, we divided the ALE data matrix into 4 groups, each group corresponding to an atomic type: F-S-N-O.

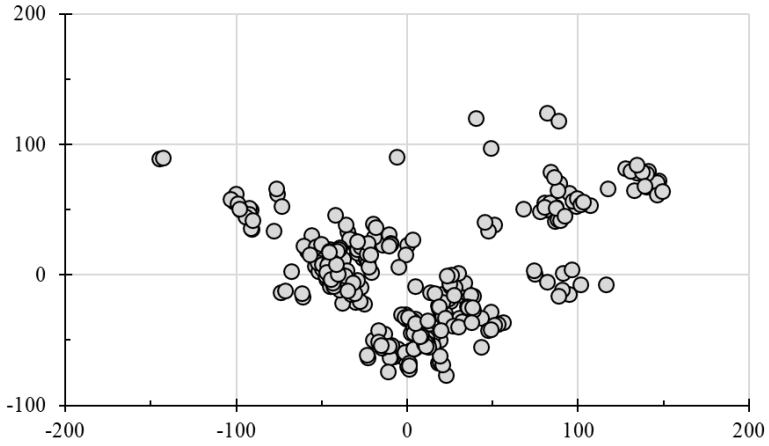

(a)

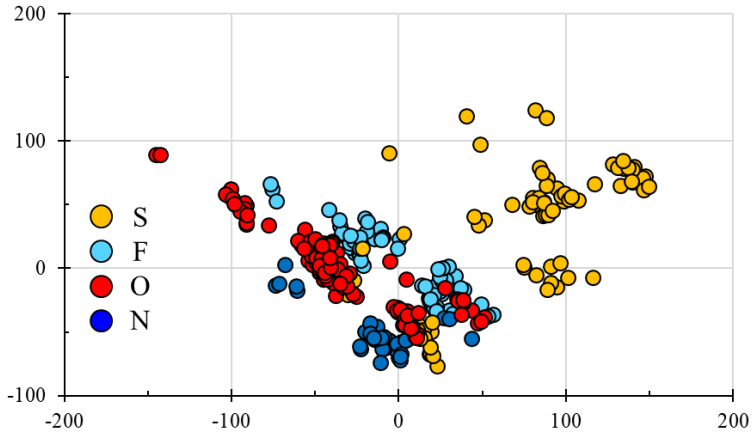

(b)

Figure 5.3 (a) Projected raw data points from the ALE collection from AIMD. Each point corresponds to a particular ALE of an atom. For purposes of the plot the dimensionality of the ALE matrix has been reduced from its original 12 dimensions to 2 dimensions. (b) Grouping the ALE data based on its atomic type.

Given a value for N_o, a clustering ML algorithm is used to cluster the ALE data in N_o groups. Each group corresponds to an atomic type; therefore, all atoms in a same group show similar parameters considered in the ALE data. For example, for the S atoms (Figure 5.4a), not all the S atoms have behaved similarly along all the 4 AIMD simulations. Using again the 2D projection technique to plot the results, we can divide the S atom ALE data in many groups as desired N_o = 4, 5 or 6 (Figure 5.4b), however, the suitable number will come from our observation of the AIMD simulations.

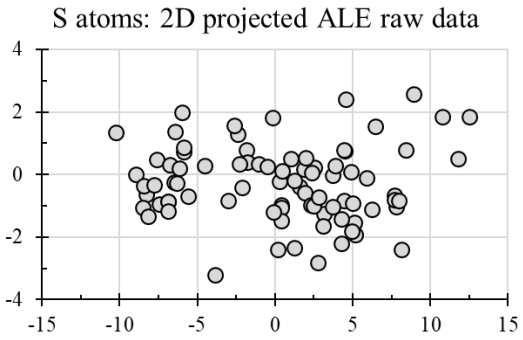

(a)

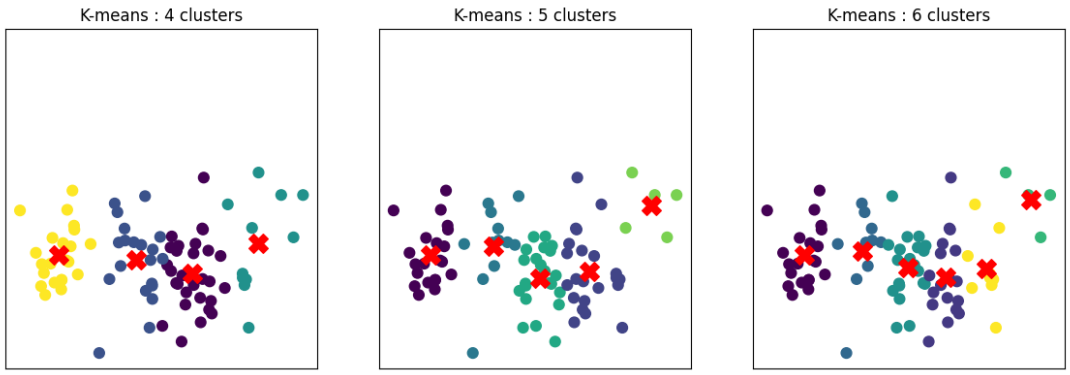

(b)

Figure 5.4 (a) 2D projected ALE data of S atoms. (b) Clustered data using No = 4, 5 and 6.

The clustering algorithm chosen to group the raw ALE data matrix is the *k*-mean. Given the dataset of *i* data points $x_1, x_2, \ldots, x_i$ such that each data point is in $\mathbf{R^d}$, the problem of finding the minimum variance clustering of the dataset into *k* clusters is that of finding *k* points $\{m_j\}$ (j = 1, 2, …, k) in $\mathbf{R^d}$ such that

$$\frac{1}{i}\sum_{t=1}^{i}\left[min_j d^2(x_i, m_j)\right] \quad (5.1)$$

Is minimized, where $d(x_i, m_j)$ refers to the Euclidean distance between x_i and m_j. The points $\{m_j\}$ (j = 1, 2, …, k) are known as cluster centroids. The clustering problem is solved

finding k cluster centroids, such that the average squared Euclidean distance, mean squared error (MSE), between a data point and its nearest cluster centroid is minimized. The number of cluster centroids is the number of groups we are going to divide the data, in this case we have N_o centroids which represents the N_o types of atoms.

The k-means[124-125] algorithm provides a method to get an approximate solution to equation 5.1. We are using the k-means algorithm due to its speed of convergence and adaptability to sparse data. The k-means algorithm can be thought of as a gradient descent procedure, which starts at initial cluster centroids calculated randomly, and iteratively updates these centroids to decrease the value of the function described in equation 5.1. The *k*-mean will update cluster centroid until converge to a local minimum. In general, we can divide the *k*-mean clustering algorithm as follow

Step 1: The number of cluster (No) to group the data and the ALE data matrix are the input values

Step 2: Initialize randomly the first *k* clusters centroids.

Step 3: Calculate arithmetic means of each cluster centroid formed in the dataset.

Step 4: *k*-means assigns each data point in the ALE data matrix to the nearest cluster centroid using Euclidian distance.

Step 5: *k*-means re-assigns each data point in the ALE data matrix to the most similar cluster and re-calculates the arithmetic mean of all the clusters in the dataset.

Force field parameters Given that ALE data is clustered in N_o groups, each atomic type has one single ALE that represents the whole group. Self-Consistent Field (SCF) calculations are performed using Gaussian-16 to each ALE to obtain the force field

parameters corresponding to each atomic type. Therefore, for each atomic type, we have a set of force field parameters. The bonded interactions will be treated by harmonic potential having the force and angles constant from the corresponding ALE. The non-bonded interactions will be treated by a Lennard-Jones potential having their parameters ε and σ constants for all the atom pairs in the corresponding ALE. Continuing with the S atom ALE data, based on electron transfer analysis and the number of bonds observed in the AIMD we can distinguish 6 types of S atoms as showed in Figure 5.5. Similarly, 3 types are used for F, 5 types for N, and 6 types for O_{FSI}.

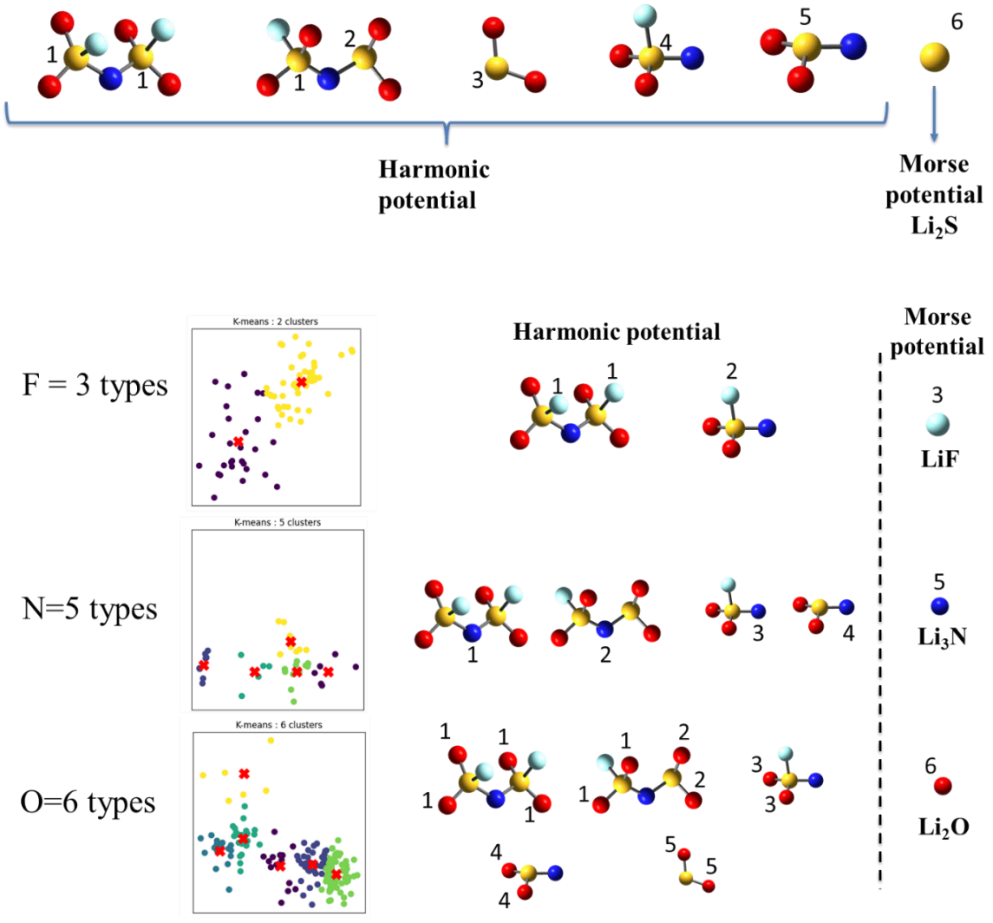

Figure 5.5 Number of types per atom (S, F, N and O) based on the AIMD simulations.

Having all the information from the AIMD distributed and clustered we can proceed to start working on building the CMD model. Therefore, we need to define an algorithm that will discriminate and identify to which atomic type from our database a particular atom corresponds as the CMD is executing.

Data classification A machine learning classifier algorithm is used to discriminate and identify the atomic type of a particular atom as the CMD simulation progress. The classifier will assign one of all the 20 atom types defined in the clustering step (6 types for S, 3 types for F, 5 types for N and 6 types for O).

Before picking a classification algorithm, some steps are done to improve the overall performance of our algorithm and to reduce computational cost. Feature selection is the process of reducing the number of input variables when developing a predictive model. It is desirable to reduce the number of input features to both reduce the computational cost of modeling and, in some cases, to improve the performance of the model.

Statistical-based feature selection methods[126] involve evaluating the relationship between each input variable and the target variable using statistics and selecting those input variables that have the strongest relationship with the target variable. For this case we use a filter-based[127] feature selection (Figure 5.6a) Additionally we also perform a K-fold cross validation analysis to determine the best number of features that need to be used in the classification algorithm keeping a good accuracy (Figure 5.6a). From both analysis, the feature score and the K-fold cross validation we use 7 features: q, C, F, H, O, O-FSI and Li-metal. Then we tested 4 different classification algorithms: K-Nearest

Neighbors,[128] Support vector machine (SVM),[129] Random Forest[130] and Decision tree,[131] obtaining the best results with the Random forest algorithm (Figure 5.6b)

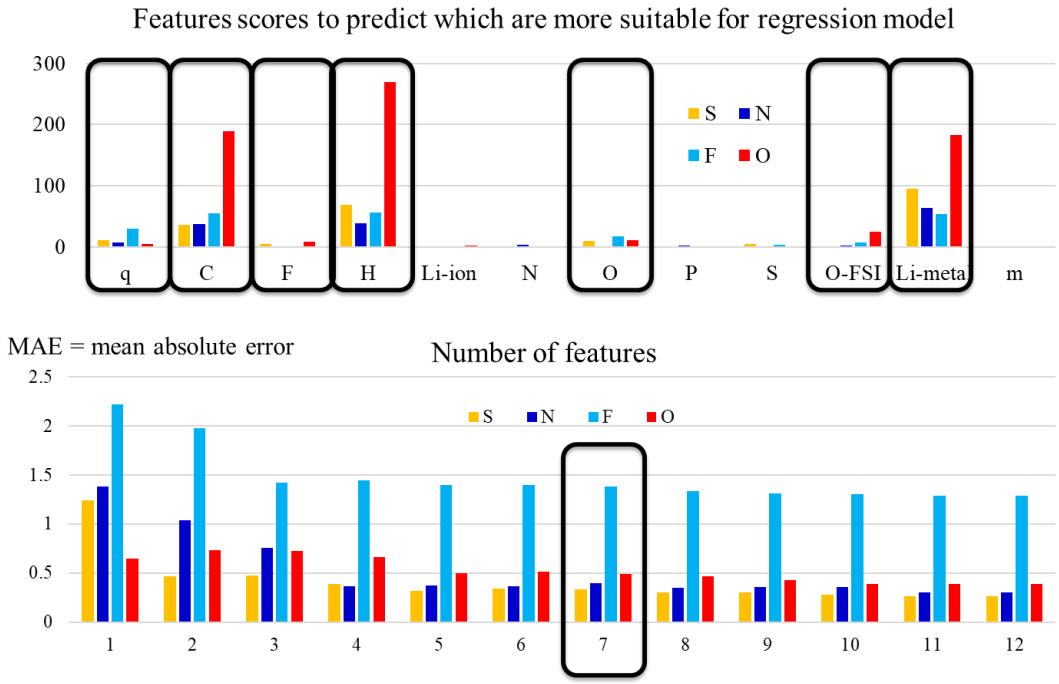

(a)

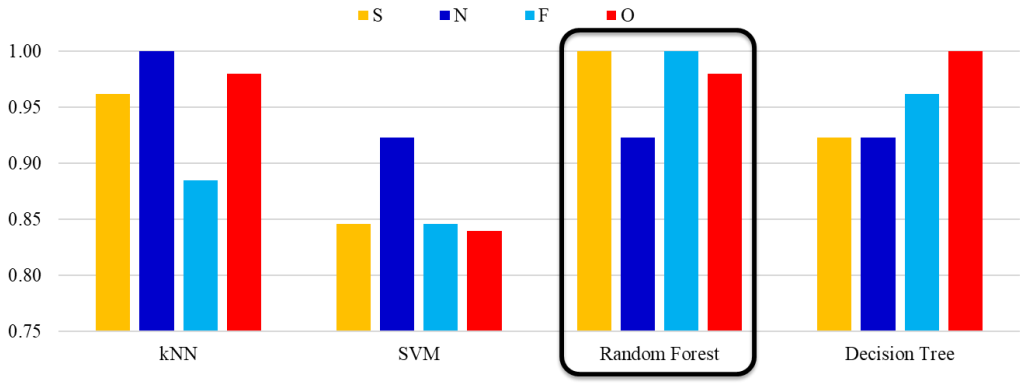

(b)

Figure 5.6 (a) Feature score and K-fold cross validation analysis prior the election of a classification algorithm. (b) Performance comparison of 4 different classification methods.

The random forest algorithm is performed in the CMD simulation every 500 steps, which corresponds to 50 fs. The two initial boxes of 1 M LiFSI/TMP AND 4 M LiFSI/TMP interfaced with a Li-metal electrolyte contains 27 LiFSI – 243 TMP – 1134 Li-metal and 108 LiFSI – 216 TMP – 1134 Li-metal, respectively. Both boxes are simulated for 0.5 ns with a thermostat set at 300 K.

5.4. Results and Discussion

Initially, there is no SEI in both boxes, 1 M LiFSI/TMP and 4 M LiFSI/TMP. As time goes on, the FSI located at the interface start reacting with the Li-metal surface showing the initial forming stage of a SEI. The total energy and temperature of the battery are showed in Figure 5.7a. The total energy decreases rapidly at the beginning of the simulation indicating initial reactions occurring at the interface to form more stable components (SEI). In the temperature plot the observed peaks can be used as indicators of reactions. For the 1 M case we observe less peaks than in the 4 M case. Since the 1 M case has less FSI counter-ions, is clear that the number of reactions occurring in the 4 M is greater than in the 1 M. Additionally for the 4 M case, we observed that the frequency of peak is greater during the first 0.1 ns of simulation time in comparison with the following 0.4 ns indicating that more reactions take place during the 0.1 ns of the simulation time.

The observed dissociation pathway of a FSI counter ion in contact with the Li-metal surface is disclosed in Figure 5.7b, showing a good agreement with the AIMD calculations showed in Figures 3.3.

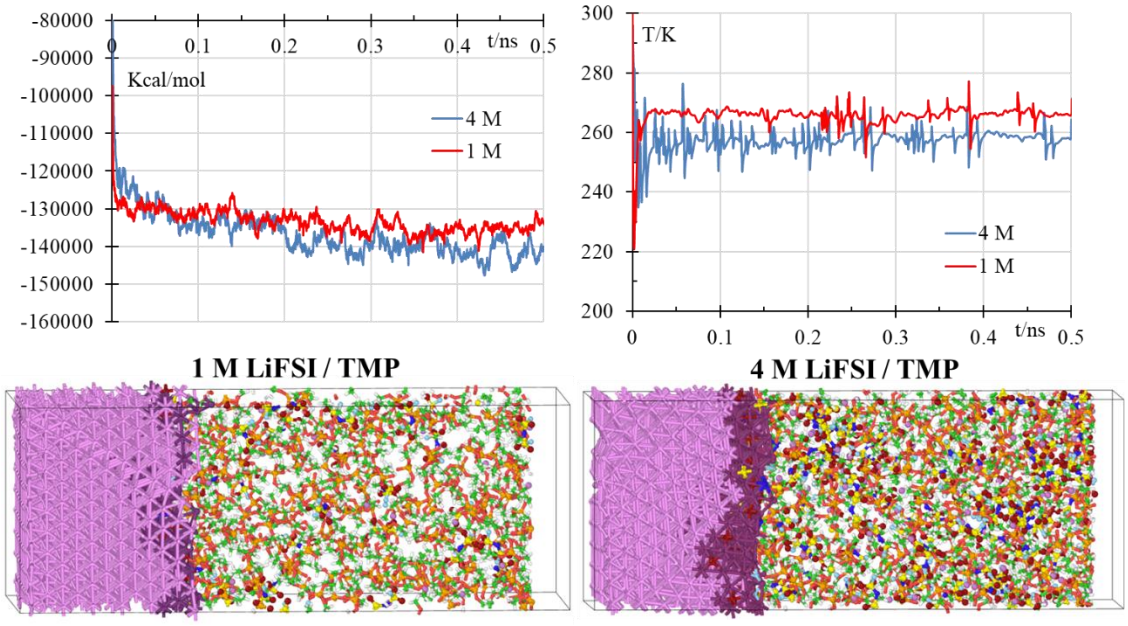

(a)

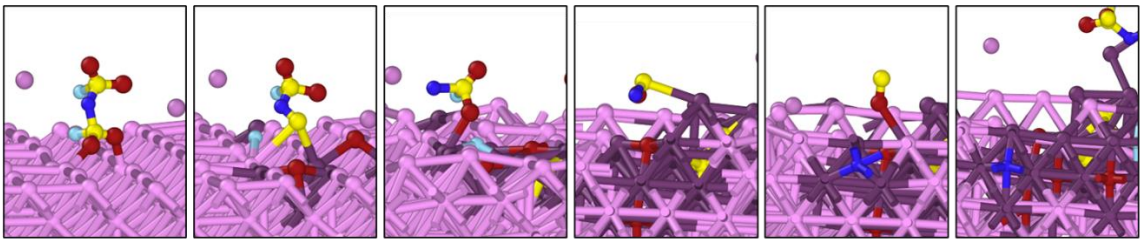

(b)

Figure 5.7 (a) Total energy (Kcal/mol) and Temperature (K) during the 0.5 ns of simulation of both boxes: 1 M LiFSI/TMP and 4 M LiFSI/TMP. (b) Observed FSI dissociation mechanism in the CMD model. O (red), S (yellow), C (green), H (white), N (blue), F (cyan), Li (pink), Li-SEI (dark pink)

The CMD model also replicates the electron transfer observed in the AIMD simulations, in which the Li-metal gains positive charge, donating their electrons to the counter-ions to start the dissociation process. For the 4 M case we observe a rapid increase in the positive charge of the Li-metal in the first 0.1 ns of the simulation, indicating that several reactions are occurring simultaneously, as the simulation progress the amount of transferred charge decreases indicating that the formed SEI is reaching a stable state acting as a protective layer between the anode and the electrolyte avoiding further electron transfers (Figure 5.8).

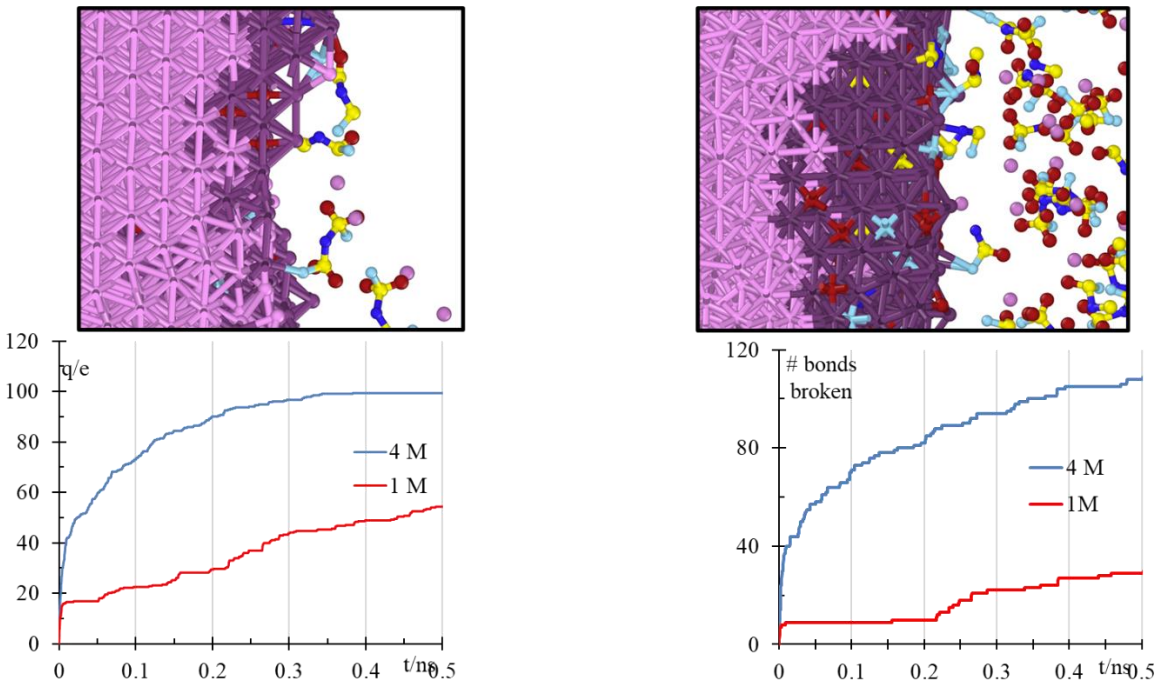

Figure 5.8 Total charge and number of bonds broken during the 0.5 ns of simulation time of both boxes: 1 M LiFSI/TMP and 4 M LiFSI/TMP.

5.5. Conclusions

We developed a CMD model to extend the study of the SEI initial formation beyond the AIMD models limitation which can only reaching ~10 ps. We compare the SEI composition when a high concentrated, 4 M, electrolyte is used in comparison with a low concentrated, 1 M.

The CMD model can replicate AIMD results indicating the formation of Li binary components such as Li_2O, LiF, Li_2S and Li_3N when the counter-ion is fully dissociated. The Li-binary components is observed in the low concentrated case. However, for the high concentrated cases other components are found. When a counter-ion approaches a region in which a previous counter-ion has been already dissociated the formed species can be Li_3NSO_2, $Li_2SO_2NSO_2$ and Li_2SO_2 which remains in the anode surface.

6. SUMMARY

This study investigates the ion-pairing, clustering, diffusivity, conductivity, and coordination of Li-ions in a LiFSI/TMP electrolyte and the solid electrolyte formation at a Li-metal/LiFSI-TMP electrolyte. Key findings are summarized below.

In Chapter II, we study the LiFSI-TMP electrolyte for 0.70 M, 1.43 M, and 3.82 M salt concentrations performing CMD simulations, which can capture the static and dynamic properties of the electrolyte solution. As the salt concentration increases, diffusivity of both ions, Li^+ and FSI^-, decreases. Results indicate that as the salt concentration increases a drop in the transport properties such as diffusivity and conductivity is observed. Moreover, it is observed that the ionicity, Λ/Λ_{NE}, decreases as the salt concentration increases, indicating a more correlated ionic motion for the 3.82 M high salt concentrated case, which is strongly linked to the formation of AGGs and ion clustering, demonstrating their significant influence in the ionic conductivity.

In Chapter III, we identified the decomposition pathway of LiFSI salt and the species present in the formed SEI between the electrolyte and the Li-metal electrode in the interfacial electrolyte−Li-metal electrode. Our data suggests that the following steps occur in the breakdown of the salt LiFSI: The counterion FSI^- rapidly loses one F ion to the lithium surface, resulting in the formation of LiF^- species. The remaining $FSO_2NSO_2^{-2}$ decomposed into SO_2^{-2} and $NFSO_2^{-2}$. The SO_2^{-2} deposited onto the Li surface. The SO_2^{-2} reacts with the Li-metal electrode forming Li_2O and Li_2S. The remaining $NFSO_2^{-2}$ defluorinate losing its F ion to the lithium surface, resulting in the formation of LiF. The NSO_2^{-1} deposited over the lithium surface decomposes in the following picoseconds

forming binary compounds Li_3N, Li_2S, and Li_2O. In contrast, when the salt is solvated by the TMP molecules avoiding a direct contact with the Li-metal electrode, only one defluorination occurs decomposing the FSI^- into $FSO_2NSO_2^{-2}$ and a F^-. The two ions remain stable as they are solvated by the TMP molecules. Therefore, salt fragmentation will necessarily take place when the counterion is in contact with the Li-metal electrode.

In Chapter IV, the SEI evolution as more counter ions approaches the Li-metal interface is study. When a 2nd FSI^- approaches the interface, facing now the previous formed SEI, the species formed are LiF, Li_2S, Li_2O and Li_3NSO_2. Thus, the full SEI composition includes LiF, Li_2S, Li_2O, Li_3N and Li_3NSO_2 species formed due to the degradation of the first two FSI^-. When a third FSI approaches the interface electrolyte/SEI, the products formed are LiF and Li_2SO_2NSO2. Thus, the SEI composition includes LiF, Li_2S, Li_2O, Li_3N, Li_3NSO_2 and $Li_2SO_2NSO_2$ species. As the SEI is being formed, it has an impact decreasing the degradation of the upcoming FSI^-, clearly indicating the protective behavior of the SEI to decrease further reaction of the counter-ions. As the dissociation reactions of the FSI^- occur, the formation of Li-binary compounds indicates the loss of these Li as charge carriers and are now part of the stable SEI, having an impact in the overall battery capacity. For the dissociation of one FSI^-, 17 Li are being consumed to form the Li-binary compounds forming the SEI. Therefore, high LiFSI concentrated electrolytes will perform better in terms of cyclability than low concentrated, since the loss of charge carriers will be less

In Chapter V, we develop an alternative classical molecular dynamics approach using machine learning techniques such as clustering and classifiers to construct dynamic

force fields keeping the accuracy of high-level ab initio calculations. A dynamic force field can change its parameters depending on the atomic environment in which the atoms are located. Atomic local environment (ALE) has been used before in the development of potentials to use in molecular dynamic simulations because atomic energy contribution depends strongly on the local chemical environment, for example, bond-order potentials such as ReaxFF, reaches size-extensibility by using the local chemical environment concept. We test the CMD results and compare them with the AIMD results obtained in Chapters III and IV.

REFERENCES

1. Kurzweil, P., Gaston Planté and his invention of the lead–acid battery—The genesis of the first practical rechargeable battery. *Journal of Power Sources* **2010,** *195* (14), 4424-4434.

2. Hess, S.; Wohlfahrt-Mehrens, M.; Wachtler, M., Flammability of Li-Ion Battery Electrolytes: Flash Point and Self-Extinguishing Time Measurements. *Journal of The Electrochemical Society* **2015,** *162* (2), A3084-A3097.

3. Galvez-Aranda, D. E.; Seminario, J. M., Ab Initio Study of the Interface of the Solid-State Electrolyte Li9N2Cl3 with a Li-Metal Electrode. *Journal of The Electrochemical Society* **2019,** *166* (10), A2048-A2057.

4. Selis, L. A.; Seminario, J. M., Dendrite formation in Li-metal anodes: an atomistic molecular dynamics study. *RSC advances* **2019,** *9* (48), 27835-27848.

5. Zhu, R.; Feng, J.; Guo, Z., In Situ Observation of Dendrite Behavior of Electrode in Half and Full Cells. *Journal of The Electrochemical Society* **2019,** *166* (6), A1107-A1113.

6. Rosso, M.; Brissot, C.; Teyssot, A.; Dollé, M.; Sannier, L.; Tarascon, J.-M.; Bouchet, R.; Lascaud, S., Dendrite short-circuit and fuse effect on Li/polymer/Li cells. *Electrochimica Acta* **2006,** *51* (25), 5334-5340.

7. Zhang, X.; Wang, S.; Xue, C.; Xin, C.; Lin, Y.; Shen, Y.; Li, L.; Nan, C.-W., Self-Suppression of Lithium Dendrite in All-Solid-State Lithium Metal Batteries with Poly(vinylidene difluoride)-Based Solid Electrolytes. *Advanced Materials* **2019,** *31* (11), 1806082.

8. Camacho-Forero, L. E.; Balbuena, P. B., Exploring interfacial stability of solid-state electrolytes at the lithium-metal anode surface. *Journal of Power Sources* **2018,** *396*, 782-790.

9. Webber, A.; Blomgren, G. E., Ionic liquids for lithium ion and related batteries. In *Advances in lithium-ion batteries*, Springer: 2002; pp 185-232.

10. Sakaebe, H.; Matsumoto, H., N-Methyl-N-propylpiperidinium bis(trifluoromethanesulfonyl)imide (PP13–TFSI) – novel electrolyte base for Li battery. *Electrochemistry Communications* **2003,** *5* (7), 594-598.

11. Heist, A.; Lee, S.-H., Improved Stability and Rate Capability of Ionic Liquid Electrolyte with High Concentration of LiFSI. *Journal of The Electrochemical Society* **2019,** *166* (10), A1860-A1866.

12. Matsumoto, H.; Sakaebe, H.; Tatsumi, K.; Kikuta, M.; Ishiko, E.; Kono, M., Fast cycling of Li/LiCoO2 cell with low-viscosity ionic liquids based on bis(fluorosulfonyl)imide [FSI]−. *Journal of Power Sources* **2006,** *160* (2), 1308-1313.

13. Yoon, H.; Howlett, P. C.; Best, A. S.; Forsyth, M.; MacFarlane, D. R., Fast Charge/Discharge of Li Metal Batteries Using an Ionic Liquid Electrolyte. *Journal of The Electrochemical Society* **2013,** *160* (10), A1629-A1637.

14. Chaban, V. V.; Voroshylova, I. V.; Kalugin, O. N.; Prezhdo, O. V., Acetonitrile Boosts Conductivity of Imidazolium Ionic Liquids. *The Journal of Physical Chemistry B* **2012,** *116* (26), 7719-7727.

15. Jitvisate, M.; Seddon, J. R. T., Near-Wall Molecular Ordering of Dilute Ionic Liquids. *The Journal of Physical Chemistry C* **2017,** *121* (34), 18593-18597.

16. Sha, M.; Dong, H.; Luo, F.; Tang, Z.; Zhu, G.; Wu, G., Dilute or Concentrated Electrolyte Solutions? Insight from Ionic Liquid/Water Electrolytes. *The Journal of Physical Chemistry Letters* **2015,** *6* (18), 3713-3720.

17. Gebbie, M. A.; Valtiner, M.; Banquy, X.; Fox, E. T.; Henderson, W. A.; Israelachvili, J. N., Ionic liquids behave as dilute electrolyte solutions. *Proceedings of the National Academy of Sciences* **2013,** *110* (24), 9674-9679.

18. Huang, C.; Huang, K.; Wang, H.; Liu, S.; Zeng, Y., The effect of solid electrolyte interface formation conditions on the aging performance of Li-ion cells. *Journal of Solid State Electrochemistry* **2011,** *15* (9), 1987-1995.

19. Liu, Y.; Xie, K.; Pan, Y.; Wang, H.; Chen, Y.; Li, Y.; Zheng, C., Impacts of the Properties of Anode Solid Electrolyte Interface on the Storage Life of Li-Ion Batteries. *The Journal of Physical Chemistry C* **2018,** *122* (17), 9411-9416.

20. Plimpton, S., Fast parallel algorithms for short-range molecular dynamics. *Journal of computational physics* **1995,** *117* (1), 1-19.

21. Tarascon, J.-M.; Armand, M., Issues and challenges facing rechargeable lithium batteries. *Materials for sustainable energy: a collection of peer-reviewed research and review articles from Nature Publishing Group* **2011**, 171-179.

22. Scrosati, B.; Garche, J., Lithium batteries: Status, prospects and future. *Journal of power sources* **2010,** *195* (9), 2419-2430.

23. Li, M.; Lu, J.; Chen, Z.; Amine, K., 30 years of lithium-ion batteries. *Advanced Materials* **2018,** *30* (33), 1800561.

24. Qiao, Y.; Jiang, K.; Deng, H.; Zhou, H., A high-energy-density and long-life lithium-ion battery via reversible oxide–peroxide conversion. *Nature Catalysis* **2019,** *2* (11), 1035-1044.

25. Goodenough, J. B.; Park, K.-S., The Li-ion rechargeable battery: a perspective. *Journal of the American Chemical Society* **2013,** *135* (4), 1167-1176.

26. Goodenough, J. B., How we made the Li-ion rechargeable battery. *Nature Electronics* **2018,** *1* (3), 204-204.

27. Yoshino, A., The birth of the lithium-ion battery. *Angewandte Chemie International Edition* **2012,** *51* (24), 5798-5800.

28. Selis, L. A.; Seminario, J. M., Dendrite formation in silicon anodes of lithium-ion batteries. *RSC advances* **2018,** *8* (10), 5255-5267.

29. Kong, L.; Li, C.; Jiang, J.; Pecht, M. G., Li-ion battery fire hazards and safety strategies. *Energies* **2018,** *11* (9), 2191.

30. Wu, X.; Song, K.; Zhang, X.; Hu, N.; Li, L.; Li, W.; Zhang, L.; Zhang, H., Safety issues in lithium ion batteries: Materials and cell design. *Frontiers in Energy Research* **2019,** *7*, 65.

31. Liu, K.; Liu, Y.; Lin, D.; Pei, A.; Cui, Y., Materials for lithium-ion battery safety. *Science advances* **2018,** *4* (6), eaas9820.

32. Kalhoff, J.; Eshetu, G. G.; Bresser, D.; Passerini, S., Safer electrolytes for lithium-ion batteries: state of the art and perspectives. *ChemSusChem* **2015,** *8* (13), 2154-2175.

33. Wang, Q.; Mao, B.; Stoliarov, S. I.; Sun, J., A review of lithium ion battery failure mechanisms and fire prevention strategies. *Progress in Energy and Combustion Science* **2019,** *73*, 95-131.

34. Yu, Y.; Che, H.; Yang, X.; Deng, Y.; Li, L.; Ma, Z.-F., Non-flammable organic electrolyte for sodium-ion batteries. *Electrochemistry Communications* **2020,** *110*, 106635.

35. Wang, X.; Yasukawa, E.; Kasuya, S., Nonflammable trimethyl phosphate solvent-containing electrolytes for lithium-ion batteries: I. Fundamental properties. *Journal of The Electrochemical Society* **2001,** *148* (10), A1058.

36. Pan, H.; Ellis, J. F.; Li, X.; Nie, Z.; Chang, H. J.; Reed, D., Electrolyte Effect on the Electrochemical Performance of Mild Aqueous Zinc-Electrolytic Manganese Dioxide Batteries. *ACS applied materials & interfaces* **2019,** *11* (41), 37524-37530.

37. Bitenc, J.; Pirnat, K.; Žagar, E.; Randon-Vitanova, A.; Dominko, R., Effect of salts on the electrochemical performance of Mg metal–organic battery. *Journal of Power Sources* **2019,** *430*, 90-94.

38. Feng, J.; Ma, P.; Yang, H.; Lu, L., Understanding the interactions of phosphonate-based flame-retarding additives with graphitic anode for lithium ion batteries. *Electrochimica Acta* **2013,** *114*, 688-692.

39. Borodin, O.; Self, J.; Persson, K. A.; Wang, C.; Xu, K., Uncharted waters: super-concentrated electrolytes. *Joule* **2020,** *4* (1), 69-100.

40. Berhaut, C. L.; Lemordant, D.; Porion, P.; Timperman, L.; Schmidt, G.; Anouti, M., Ionic association analysis of LiTDI, LiFSI and LiPF 6 in EC/DMC for better Li-ion battery performances. *RSC advances* **2019,** *9* (8), 4599-4608.

41. Chen, L.; Li, Y.; Li, S.-P.; Fan, L.-Z.; Nan, C.-W.; Goodenough, J. B., PEO/garnet composite electrolytes for solid-state lithium batteries: From "ceramic-in-polymer" to "polymer-in-ceramic". *Nano Energy* **2018,** *46*, 176-184.

42. Gupta, A.; Sakamoto, J., Controlling ionic transport through the PEO-LiTFSI/LLZTO interface. *The Electrochemical Society Interface* **2019,** *28* (2), 63.

43. Shi, P.; Zheng, H.; Liang, X.; Sun, Y.; Cheng, S.; Chen, C.; Xiang, H., A highly concentrated phosphate-based electrolyte for high-safety rechargeable lithium batteries. *Chemical communications* **2018,** *54* (35), 4453-4456.

44. Xu, K.; Ding, M. S.; Zhang, S.; Allen, J. L.; Jow, T. R., An attempt to formulate nonflammable lithium ion electrolytes with alkyl phosphates and phosphazenes. *Journal of the Electrochemical Society* **2002,** *149* (5), A622.

45. Khetan, A.; Arjmandi, H. R.; Pande, V.; Pitsch, H.; Viswanathan, V., Understanding ion pairing in high-salt concentration electrolytes using classical molecular dynamics simulations and its implications for nonaqueous Li–O2 batteries. *The Journal of Physical Chemistry C* **2018,** *122* (15), 8094-8101.

46. Qian, J.; Henderson, W. A.; Xu, W.; Bhattacharya, P.; Engelhard, M.; Borodin, O.; Zhang, J.-G., High rate and stable cycling of lithium metal anode. *Nature communications* **2015,** *6* (1), 1-9.

47. Wang, M.; Huai, L.; Hu, G.; Yang, S.; Ren, F.; Wang, S.; Zhang, Z.; Chen, Z.; Peng, Z.; Shen, C., Effect of LiFSI concentrations to form thickness-and modulus-controlled SEI layers on lithium metal anodes. *The Journal of Physical Chemistry C* **2018,** *122* (18), 9825-9834.

48. Camacho-Forero, L. E.; Smith, T. W.; Balbuena, P. B., Effects of high and low salt concentration in electrolytes at lithium–metal anode surfaces. *The Journal of Physical Chemistry C* **2017,** *121* (1), 182-194.

49. Zheng, Y.; Soto, F. A.; Ponce, V.; Seminario, J. M.; Cao, X.; Zhang, J.-G.; Balbuena, P. B., Localized high concentration electrolyte behavior near a lithium–metal anode surface. *Journal of Materials Chemistry A* **2019,** *7* (43), 25047-25055.

50. Galvez-Aranda, D. E.; Seminario, J. M., Li-Metal Anode in Dilute Electrolyte LiFSI/TMP: Electrochemical Stability Using Ab Initio Molecular Dynamics. *The Journal of Physical Chemistry C* **2020,** *124* (40), 21919-21934.

51. Yamada, Y.; Yamada, A., Superconcentrated electrolytes for lithium batteries. *Journal of The Electrochemical Society* **2015,** *162* (14), A2406.

52. Perez Beltran, S.; Cao, X.; Zhang, J.-G.; Balbuena, P. B., Localized High Concentration Electrolytes for High Voltage Lithium–Metal Batteries: Correlation between the Electrolyte Composition and Its Reductive/Oxidative Stability. *Chemistry of Materials* **2020,** *32* (14), 5973-5984.

53. Wang, J.; Yamada, Y.; Sodeyama, K.; Chiang, C. H.; Tateyama, Y.; Yamada, A., Superconcentrated electrolytes for a high-voltage lithium-ion battery. *Nature communications* **2016,** *7* (1), 1-9.

54. Giannozzi, P.; Baroni, S.; Bonini, N.; Calandra, M.; Car, R.; Cavazzoni, C.; Ceresoli, D.; Chiarotti, G. L.; Cococcioni, M.; Dabo, I., QUANTUM ESPRESSO: a modular and open-source software project for quantum simulations of materials. *Journal of physics: Condensed matter* **2009,** *21* (39), 395502.

55. Ropo, M.; Kokko, K.; Vitos, L., Assessing the Perdew-Burke-Ernzerhof exchange-correlation density functional revised for metallic bulk and surface systems. *Physical Review B* **2008,** *77* (19), 195445.

56. Perdew, J. P.; Burke, K.; Ernzerhof, M., Generalized gradient approximation made simple. *Physical review letters* **1996,** *77* (18), 3865.

57. Blöchl, P. E., Projector augmented-wave method. *Physical review B* **1994,** *50* (24), 17953.

58. Tang, W.; Sanville, E.; Henkelman, G., A grid-based Bader analysis algorithm without lattice bias. *Journal of Physics: Condensed Matter* **2009,** *21* (8), 084204.

59. Sanville, E.; Kenny, S. D.; Smith, R.; Henkelman, G., Improved grid-based algorithm for Bader charge allocation. *Journal of computational chemistry* **2007,** *28* (5), 899-908.

60. Henkelman, G.; Arnaldsson, A.; Jónsson, H., A fast and robust algorithm for Bader decomposition of charge density. *Computational Materials Science* **2006,** *36* (3), 354-360.

61. Marcus, Y., Ionic radii in aqueous solutions. *Chemical Reviews* **1988,** *88* (8), 1475-1498.

62. Baur, W. H., Effective ionic radii in nitrides. *Crystallography Reviews* **1987,** *1* (1), 59-83.

63. Youngs, T. G.; Hardacre, C., Application of static charge transfer within an ionic-liquid force field and its effect on structure and dynamics. *ChemPhysChem* **2008,** *9* (11), 1548-1558.

64. Borodin, O.; Smith, G. D., Quantum chemistry and molecular dynamics simulation study of dimethyl carbonate: ethylene carbonate electrolytes doped with LiPF6. *The Journal of Physical Chemistry B* **2009,** *113* (6), 1763-1776.

65. Wang, J.; Hou, T., Application of molecular dynamics simulations in molecular property prediction. 1. Density and heat of vaporization. *Journal of chemical theory and computation* **2011,** *7* (7), 2151-2165.

66. Hess, S.; Wohlfahrt-Mehrens, M.; Wachtler, M., Flammability of Li-ion battery electrolytes: flash point and self-extinguishing time measurements. *Journal of The Electrochemical Society* **2015,** *162* (2), A3084.

67. Wang, J.; Yamada, Y.; Sodeyama, K.; Watanabe, E.; Takada, K.; Tateyama, Y.; Yamada, A., Fire-extinguishing organic electrolytes for safe batteries. *Nature Energy* **2018,** *3* (1), 22-29.

68. Ruiz, V.; Pfrang, A.; Kriston, A.; Omar, N.; Van den Bossche, P.; Boon-Brett, L., A review of international abuse testing standards and regulations for lithium ion

batteries in electric and hybrid electric vehicles. *Renewable and Sustainable Energy Reviews* **2018,** *81*, 1427-1452.

69. Birkl, C. R.; Roberts, M. R.; McTurk, E.; Bruce, P. G.; Howey, D. A., Degradation diagnostics for lithium ion cells. *Journal of Power Sources* **2017,** *341*, 373-386.

70. Gómez-Cámer, J. L.; Novák, P., Electrochemical impedance spectroscopy: Understanding the role of the reference electrode. *Electrochemistry communications* **2013,** *34*, 208-210.

71. Raccichini, R.; Amores, M.; Hinds, G., Critical review of the use of reference electrodes in Li-ion batteries: a diagnostic perspective. *Batteries* **2019,** *5* (1), 12.

72. Orendorff, C. J.; Roth, E. P.; Nagasubramanian, G., Experimental triggers for internal short circuits in lithium-ion cells. *Journal of Power Sources* **2011,** *196* (15), 6554-6558.

73. Belt, J. R.; Bernardi, D. M.; Utgikar, V., Development and use of a lithium-metal reference electrode in aging studies of lithium-ion batteries. *Journal of The Electrochemical Society* **2014,** *161* (6), A1116.

74. Cho, S., Nonflammable Lithium Metal Full Cells with Ultra-high Energy Density Based on Coordinated Carbonate Electrolytes. iScience 23. **2020**.

75. Park, M. S.; Ma, S. B.; Lee, D. J.; Im, D.; Doo, S.-G.; Yamamoto, O., A highly reversible lithium metal anode. *Scientific reports* **2014,** *4* (1), 1-8.

76. Zhang, R.; Li, N. W.; Cheng, X. B.; Yin, Y. X.; Zhang, Q.; Guo, Y. G., Advanced micro/nanostructures for lithium metal anodes. *Advanced Science* **2017,** *4* (3), 1600445.

77. Lee, Y. M.; Seo, J. E.; Lee, Y.-G.; Lee, S. H.; Cho, K. Y.; Park, J.-K., Effects of triacetoxyvinylsilane as SEI layer additive on electrochemical performance of lithium metal secondary battery. *Electrochemical and Solid State Letters* **2007,** *10* (9), A216.

78. Zhang, H.; Eshetu, G. G.; Judez, X.; Li, C.; Rodriguez-Martínez, L. M.; Armand, M., Electrolyte additives for lithium metal anodes and rechargeable lithium metal batteries: progress and perspectives. *Angewandte Chemie International Edition* **2018,** *57* (46), 15002-15027.

79. Takeda, Y.; Yamamoto, O.; Imanishi, N., Lithium dendrite formation on a lithium metal anode from liquid, polymer and solid electrolytes. *Electrochemistry* **2016,** *84* (4), 210-218.

80. Tikekar, M. D.; Choudhury, S.; Tu, Z.; Archer, L. A., Design principles for electrolytes and interfaces for stable lithium-metal batteries. *Nature Energy* **2016,** *1* (9), 1-7.

81. Xu, R.; Cheng, X.-B.; Yan, C.; Zhang, X.-Q.; Xiao, Y.; Zhao, C.-Z.; Huang, J.-Q.; Zhang, Q., Artificial interphases for highly stable lithium metal anode. *Matter* **2019,** *1* (2), 317-344.

82. Xu, C.-X.; Jiang, J.-J., Designing electrolytes for lithium metal batteries with rational interface stability. *Rare Metals* **2021,** *40* (2), 243-245.

83. Pender, J. P.; Jha, G.; Youn, D. H.; Ziegler, J. M.; Andoni, I.; Choi, E. J.; Heller, A.; Dunn, B. S.; Weiss, P. S.; Penner, R. M.; Mullins, C. B., Electrode Degradation in Lithium-Ion Batteries. *ACS Nano* **2020,** *14* (2), 1243-1295.

84. Cabana, J.; Kwon, B. J.; Hu, L., Mechanisms of Degradation and Strategies for the Stabilization of Cathode–Electrolyte Interfaces in Li-Ion Batteries. *Accounts of Chemical Research* **2018,** *51* (2), 299-308.

85. Galvez-Aranda, D. E.; Seminario, J. M., Simulations of a LiF Solid Electrolyte Interphase Cracking on Silicon Anodes Using Molecular Dynamics. *Journal of The Electrochemical Society* **2018,** *165* (3), A717-A730.

86. Leung, K.; Pearse, A. J.; Talin, A. A.; Fuller, E. J.; Rubloff, G. W.; Modine, N. A., Kinetics-Controlled Degradation Reactions at Crystalline LiPON/LixCoO2 and Crystalline LiPON/Li-Metal Interfaces. *ChemSusChem* **2018,** *11* (12), 1956-1969.

87. Wang, J.; Yang, J.; Xiao, Q.; Zhang, J.; Li, T.; Jia, L.; Wang, Z.; Cheng, S.; Li, L.; Liu, M., In Situ Self-Assembly of Ordered Organic/Inorganic Dual-Layered Interphase for Achieving Long-Life Dendrite-Free Li Metal Anodes in LiFSI-Based Electrolyte. *Advanced Functional Materials* **2021,** *31* (7), 2007434.

88. Zhang, H.; Shen, C.; Huang, Y.; Liu, Z., Spontaneously formation of SEI layers on lithium metal from LiFSI/DME and LiTFSI/DME electrolytes. *Applied Surface Science* **2021,** *537*, 147983.

89. Lu, H.; Zhu, Y.; Yuan, Y.; He, L.; Zheng, B.; Zheng, X.; Liu, C.; Du, H., LiFSI as a functional additive of the fluorinated electrolyte for rechargeable Li-S batteries. *Journal of Materials Science: Materials in Electronics* **2021,** *32* (5), 5898-5906.

90. Zhang, K.; Tian, Y.; Wei, C.; An, Y.; Feng, J., Building stable solid electrolyte interphases (SEI) for microsized silicon anode and 5V-class cathode with salt engineered nonflammable phosphate-based lithium-ion battery electrolyte. *Applied Surface Science* **2021,** *553*, 149566.

91. Galvez-Aranda, D. E.; Seminario, J. M., Ion Pairing, Clustering and Transport in a LiFSI-TMP Electrolyte as Functions of Salt Concentration using Molecular Dynamics Simulations. *Journal of The Electrochemical Society* **2021,** *168* (4), 040511.

92. Zhou, G.; Lin, X.; Liu, J.; Yu, J.; Wu, J.; Law, H. M.; Wang, Z.; Ciucci, F., In situ formation of poly(butyl acrylate)-based non-flammable elastic quasi-solid electrolyte for dendrite-free flexible lithium metal batteries with long cycle life for wearable devices. *Energy Storage Materials* **2021,** *34*, 629-639.

93. Min, Z.; Gaojie, X.; Di, L.; Bin, X.; Lang, H.; Wei, W.; 光磊, 崔., Formulating a Non-Flammable Highly Concentrated Dual-Salt Electrolyte for Wide Temperature High-Nickel Lithium Ion Batteries. *Journal of The Electrochemical Society* **2021**.

94. Jia, H.; Xu, Y.; Zhang, X.; Burton, S. D.; Gao, P.; Matthews, B. E.; Engelhard, M. H.; Han, K. S.; Zhong, L.; Wang, C.; Xu, W., Advanced Low-Flammable Electrolytes for Stable Operation of High-Voltage Lithium-Ion Batteries. *Angewandte Chemie International Edition* **2021,** *n/a* (n/a).

95. Liu, S.; Mao, J.; Zhang, L.; Pang, W. K.; Du, A.; Guo, Z., Manipulating the Solvation Structure of Nonflammable Electrolyte and Interface to Enable Unprecedented Stability of Graphite Anodes beyond 2 Years for Safe Potassium-Ion Batteries. *Advanced Materials* **2021,** *33* (1), 2006313.

96. Marchiori, C. F. N.; Carvalho, R. P.; Ebadi, M.; Brandell, D.; Araujo, C. M., Understanding the Electrochemical Stability Window of Polymer Electrolytes in Solid-State Batteries from Atomic-Scale Modeling: The Role of Li-Ion Salts. *Chemistry of Materials* **2020,** *32* (17), 7237-7246.

97. Peljo, P.; Girault, H. H., Electrochemical potential window of battery electrolytes: the HOMO–LUMO misconception. *Energy & Environmental Science* **2018,** *11* (9), 2306-2309.

98. Wang, X.; Yasukawa, E.; Kasuya, S., Nonflammable Trimethyl Phosphate Solvent-Containing Electrolytes for Lithium-Ion Batteries: II. The Use of an Amorphous Carbon Anode. *Journal of The Electrochemical Society* **2001,** *148* (10), A1066.

99. Benitez, L.; Cristancho, D.; Seminario, J.; de la Hoz, J. M.; Balbuena, P., Electron transfer through solid-electrolyte-interphase layers formed on Si anodes of Li-ion batteries. *Electrochimica Acta* **2014,** *140*, 250-257.

100. Combes, J.-M.; Duclos, P.; Seiler, R., The born-oppenheimer approximation. In *Rigorous atomic and molecular physics*, Springer: 1981; pp 185-213.

101. Parr, R. G., Density functional theory. *Annual Review of Physical Chemistry* **1983,** *34* (1), 631-656.

102. Perdew, J. P.; Burke, K.; Ernzerhof, M., Generalized Gradient Approximation Made Simple. *Physical Review Letters* **1996,** *77* (18), 3865-3868.

103. Sanville, E.; Kenny, S. D.; Smith, R.; Henkelman, G., Improved grid-based algorithm for Bader charge allocation. *Journal of Computational Chemistry* **2007,** *28* (5), 899-908.

104. Kayyar, A.; Huang, J.; Samiee, M.; Luo, J., Construction and testing of coin cells of lithium ion batteries. *Journal of visualized experiments: JoVE* **2012,** (66).

105. Wang, A.; Kadam, S.; Li, H.; Shi, S.; Qi, Y., Review on modeling of the anode solid electrolyte interphase (SEI) for lithium-ion batteries. *npj Computational Materials* **2018,** *4* (1), 15.

106. Kumar, N.; Siegel, D. J., Interface-Induced Renormalization of Electrolyte Energy Levels in Magnesium Batteries. *The Journal of Physical Chemistry Letters* **2016,** *7* (5), 874-881.

107. Binninger, T.; Marcolongo, A.; Mottet, M.; Weber, V.; Laino, T., Comparison of computational methods for the electrochemical stability window of solid-state electrolyte materials. *Journal of Materials Chemistry A* **2020,** *8* (3), 1347-1359.

108. Costa, C. M.; Silva, M. M.; Lanceros-Méndez, S., Battery separators based on vinylidene fluoride (VDF) polymers and copolymers for lithium ion battery applications. *Rsc Advances* **2013,** *3* (29), 11404-11417.

109. Jang, J.; Oh, J.; Jeong, H.; Kang, W.; Jo, C., A Review of Functional Separators for Lithium Metal Battery Applications. *Materials* **2020,** *13* (20), 4625.

110. Mauger, A.; Julien, C. M.; Paolella, A.; Armand, M.; Zaghib, K., Building Better Batteries in the Solid State: A Review. *Materials (Basel)* **2019,** *12* (23), 3892.

111. An, S. J.; Li, J.; Mohanty, D.; Daniel, C.; Polzin, B. J.; Croy, J. R.; E. Trask, S.; Wood, D. L., Correlation of Electrolyte Volume and Electrochemical Performance in Lithium-Ion Pouch Cells with Graphite Anodes and NMC532 Cathodes. *Journal of The Electrochemical Society* **2017,** *164* (6), A1195-A1202.

112. Peled, E., The electrochemical behavior of alkali and alkaline earth metals in nonaqueous battery systems—the solid electrolyte interphase model. *Journal of The Electrochemical Society* **1979,** *126* (12), 2047.

113. Cheng, X. B.; Zhang, R.; Zhao, C. Z.; Wei, F.; Zhang, J. G.; Zhang, Q., A review of solid electrolyte interphases on lithium metal anode. *Advanced science* **2016,** *3* (3), 1500213.

114. Zhang, Z.; Yang, J.; Huang, W.; Wang, H.; Zhou, W.; Li, Y.; Li, Y.; Xu, J.; Huang, W.; Chiu, W.; Cui, Y., Cathode-Electrolyte Interphase in Lithium Batteries Revealed by Cryogenic Electron Microscopy. *Matter* **2021,** *4* (1), 302-312.

115. Cho, S.-J.; Yu, D.-E.; Pollard, T. P.; Moon, H.; Jang, M.; Borodin, O.; Lee, S.-Y., Nonflammable Lithium Metal Full Cells with Ultra-high Energy Density Based on Coordinated Carbonate Electrolytes. *iScience* **2020,** *23* (2), 100844.

116. Hsieh, Y.-C.; Leißing, M.; Nowak, S.; Hwang, B.-J.; Winter, M.; Brunklaus, G., Quantification of Dead Lithium via In Situ Nuclear Magnetic Resonance Spectroscopy. *Cell Reports Physical Science* **2020,** *1* (8), 100139.

117. Galvez-Aranda, D. E.; Seminario, J. M., Simulations of a LiF solid electrolyte interphase cracking on silicon anodes using molecular dynamics. *Journal of The Electrochemical Society* **2018,** *165* (3), A717.

118. Ponce, V.; Galvez-Aranda, D. E.; Seminario, J. M., Analysis of a Li-ion nanobattery with graphite anode using molecular dynamics simulations. *The Journal of Physical Chemistry C* **2017,** *121* (23), 12959-12971.

119. McLaughlin, D. R.; Thompson, D. L., Ab initio dynamics: HeH++ H 2→ He+ H 3+(C 2v) classical trajectories using a quantum mechanical potential-energy surface. *The Journal of Chemical Physics* **1973,** *59* (8), 4393-4405.

120. Truhlar, D. G.; Horowitz, C. J., Functional representation of liu and siegbahn's accurate abinitio potential energy calculations for h+ h2. *The Journal of Chemical Physics* **1978,** *68* (5), 2466-2476.

121. Maisuradze, G. G.; Thompson, D. L.; Wagner, A. F.; Minkoff, M., Interpolating moving least-squares methods for fitting potential energy surfaces: Detailed analysis of one-dimensional applications. *The Journal of chemical physics* **2003,** *119* (19), 10002-10014.

122. Khorshidi, A.; Peterson, A. A., Amp: A modular approach to machine learning in atomistic simulations. *Computer Physics Communications* **2016,** *207*, 310-324.

123. Van Duin, A. C.; Dasgupta, S.; Lorant, F.; Goddard, W. A., ReaxFF: a reactive force field for hydrocarbons. *The Journal of Physical Chemistry A* **2001,** *105* (41), 9396-9409.

124. Huang, Z., Extensions to the k-means algorithm for clustering large data sets with categorical values. *Data mining and knowledge discovery* **1998,** *2* (3), 283-304.

125. Likas, A.; Vlassis, N.; Verbeek, J. J., The global k-means clustering algorithm. *Pattern recognition* **2003,** *36* (2), 451-461.

126. Solorio-Fernández, S.; Carrasco-Ochoa, J. A.; Martínez-Trinidad, J. F., A review of unsupervised feature selection methods. *Artificial Intelligence Review* **2020,** *53* (2), 907-948.

127. Xue, B.; Cervante, L.; Shang, L.; Browne, W. N.; Zhang, M., Multi-objective evolutionary algorithms for filter based feature selection in classification. *International Journal on Artificial Intelligence Tools* **2013,** *22* (04), 1350024.

128. Peterson, L. E., K-nearest neighbor. *Scholarpedia* **2009,** *4* (2), 1883.

129. Yang, Y.; Li, J.; Yang, Y. In *The research of the fast SVM classifier method*, 2015 12th international computer conference on wavelet active media technology and information processing (ICCWAMTIP), IEEE: 2015; pp 121-124.

130. Pal, M., Random forest classifier for remote sensing classification. *International journal of remote sensing* **2005,** *26* (1), 217-222.

131. Quinlan, J. R., Learning decision tree classifiers. *ACM Computing Surveys (CSUR)* **1996,** *28* (1), 71-72.